Lawrence Berkeley National Laboratory

Recent Work

Title
THE HYPERFUSE-STRUCTURE ANOMALIES OF GOLD-198 AND GOLD-199

Permalink
https://escholarship.org/uc/item/5ds5j0k0

Author
Bout, Paul Adrian Vanden.

Publication Date
1966-03-31

University of California

Ernest O. Lawrence
Radiation Laboratory

THE HYPERFINE-STRUCTURE ANOMALIES OF GOLD-198 AND GOLD-199

DISCLAIMER

UCRL-16757

UNIVERSITY OF CALIFORNIA

Lawrence Radiation Laboratory
Berkeley, California

AEC Contract No. W-7405-eng-48

THE HYPERFINE-STRUCTURE ANOMALIES
OF GOLD-198 AND GOLD-199

Paul Adrian Vanden Bout

(Ph. D. Thesis)

March 31, 1966

THE HYPERFINE-STRUCTURE ANOMALIES
OF GOLD-198 AND GOLD-199

Contents

THE HYPERFINE-STRUCTURE ANOMALIES
OF GOLD-198 AND GOLD-199

Paul Adrian Vanden Bout

Lawrence Radiation Laboratory
University of California
Berkeley, California

March 31, 1966

ABSTRACT

I have measured the hyperfine-structure separations and nuclear magnetic moments of Au^{198}(2.70d) and Au^{199}(3.15d) using the atomic-beam magnetic-resonance method. I also measured the ratio of the electronic g factor of gold to those of potassium and cesium. The results are, for Au^{198} (I=2), $\Delta\nu$ = 21450.7167(5) MHz, $\mu_{I_{uncorr}}$ = + 0.5842(4)nm; and for Au^{199} (I=3/2), $\Delta\nu$ = 10962.7227(3) MHz, $\mu_{I_{uncorr}}$ = + 0.2673(7)nm. The results for the g-factor ratios are: $g_J(Au^{198, 199})/g_J(K^{39})$ = 1.000504(2) and $g_J(Au^{198, 199})/g_J(Cs^{133})$ = 1.000381(2). For all these results the error in the last place, enclosed in parentheses, represents twice the standard deviation of a least-squares fit, with χ^2 = 5.4 for Au^{198} with 47 observations, and with χ^2 = 4.9 for Au^{199} with 37 observations. Second-order corrections to the hyperfine structure are shown to be negligible. The nuclear results are interpreted in terms of the shell model of the nucleus with allowance for configuration mixing. The measurement of some ratios of alkali electronic g factors has also been made with the results: $g_J(Cs^{133})/g_J(K^{39})$ = 1.0001231(3), $g_J(Rb^{85, 87})/g_J(K^{39})$ = 1.0000182(2), and $g_J(Na^{23})/g_J(K^{39})$ = 1.0000007(2).

I. INTRODUCTION

The hyperfine structure (hfs) of the element gold was first observed in 1931, when Ritschl observed lines in the AuI spectrum that were split into four components.[1] He concluded that the nuclear angular momentum (for the 100%-abundant, stable isotope Au^{197}) is $(3/2)\hbar$. Since then further investigations have been made into the hyperfine structure of Au^{197} as well as into the hyperfine structure of nine radioactive isotopes of gold.[2-9] All of the work on the radioactive isotopes and in particular the work described in this thesis has been done with the magnetic-resonance atomic-beam method. For the history of this technique any one of a number of review articles may be consulted.[10-12]

The research reported in this thesis is part of a continuing program by the Atomic Beam Group of the Lawrence Radiation Laboratory to measure nuclear spins and static moments. Such information about nuclei provides a basis for the formation of nuclear theories and a means of checking the validity of any proposed nuclear theories.

Our experiment began as a summer project to measure the signs of the nuclear magnetic-dipole moments of Au^{198} and Au^{199}. Because we suspected that these isotopes might have large hyperfine-structure anomalies, I chose to measure the anomalies as a thesis project. This anomaly is an effect related to the finite size of the nucleus. It is of interest as a parameter describing the nucleus in atoms such as radioactive gold whose ground state of $^2S_{1/2}$ precludes the measurement of the nuclear electric quadrupole moment.

These two isotopes are particularly well suited to the long series of measurements required to determine the hyperfine-structure anomaly. The half lives are sufficiently long, being 2.70 days for Au^{198} and 3.15 days for Au^{199}. Sufficient quantities of both isotopes are easily produced in a reactor. When the experiment began, the following information was available:[13]

	Au^{198}	Au^{199}
Nuclear spin I	2	3/2
hfs separation $\Delta\nu$ (if $\mu_I > 0$)	21800(150)	11110(130)
hfs separation $\Delta\nu$ (if $\mu_I < 0$)	22500(150)	11180(130)

Another research group provided a preliminary value of the quantity $g_J(\mathrm{Au}^{197})/g_J(\mathrm{K}^{39}) = 1.00050756(55)$. (Ref. 14).

I will describe the theory relevant to our experiment (Sec. II), the apparatus and experimental techniques used (Sec. III), and the data and results obtained (Sec. IV), and I will interpret the results in terms of the theory (Sec. V).

II. THEORY

A. Fine Structure

A Hamiltonian yielding a good approximation to the fine-structure energy levels of an isolated atom is

$$\mathcal{H} = \sum_{i=1}^{Z} \left\{ \frac{p_i^2}{2m} - \frac{Ze^2}{r_i} \right\} + \sum_{i>j=1}^{Z} \frac{e^2}{r_{ij}} + \sum_{i=1}^{Z} \xi_i(r_i) \vec{\ell}_i \cdot \vec{s}_i , \qquad (1)$$

where r_i is the distance of the _i_th electron from the nucleus, and r_{ij} is the distance of the _i_th electron from the _r_th electron. The last term repre-sents the interaction between the spin magnetic-dipole moment of the _i_th electron and the magnetic field produced by its orbital motion. This Hamiltonian is nonrelativistic and ignores spin-spin, orbit-orbit, and spin-other-orbit interactions.

As this Hamiltonian is too difficult to solve analytically, virtually all calculations begin with the Central-Field Approximation in which the non-central Coulomb and spin-orbit portions of (1) are treated as a perturbation on the eigenstates of the following Hamiltonian:

$$\mathcal{H}_{central} = \sum_{i=1}^{Z} \left\{ \frac{p_i^2}{2m} + U_i(r_i) \right\} , \qquad (2)$$

where $U_i(r_i)$ is some spherically symmetric potential. The eigenstates of $\mathcal{H}_{central}$ are products of single-electron wave functions, each of which has the form $\psi_i = R_{n\ell}(r_i) Y_\ell^m(\theta_i, \phi_i)$. The spin of the electron is taken into account by including in each ψ_i a factor α or β corresponding to $m_s = +1/2$ or $m_s = -1/2$, respectively. The product wave function ψ satis-fying the Pauli exclusion principle is then of the form

$$\psi = (N!)^{-1/2} \begin{vmatrix} \psi_1(1) & \psi_1(2) \cdots \psi_1(N) \\ \psi_2(1) & \psi_2(2) \cdots \psi_2(N) \\ \cdots \cdots \cdots \cdots \cdots \cdots \\ \psi_N(1) & \psi_N(2) \cdots \psi_N(N) \end{vmatrix} , \qquad (3)$$

where the index in parentheses refers to a set of quantum numbers (n, ℓ, m_ℓ, m_s) and hence specifies a function, and the subscripts refer to the spin and spatial coordinates of a particular electron. The diagonal of this determinant contains all the information about ψ, and the energy eigenvalue of ψ is usually labelled by the following expression called the configuration: $(n_1 \ell_1)^{X(1)} (n_2 \ell_2)^{X(2)} \ldots (n_N \ell_N)^{X(N)}$, where $X(i)$ specifies the number of times $(n_i \ell_i)$ occurs. Gold has the ground-state configuration $1s^2 2s^2 2p^6 3s^2 3p^6 3d^{10} 4s^2 4p^6 4d^{10} 4f^{14} 5s^2 5p^6 5d^{10} 6s$.
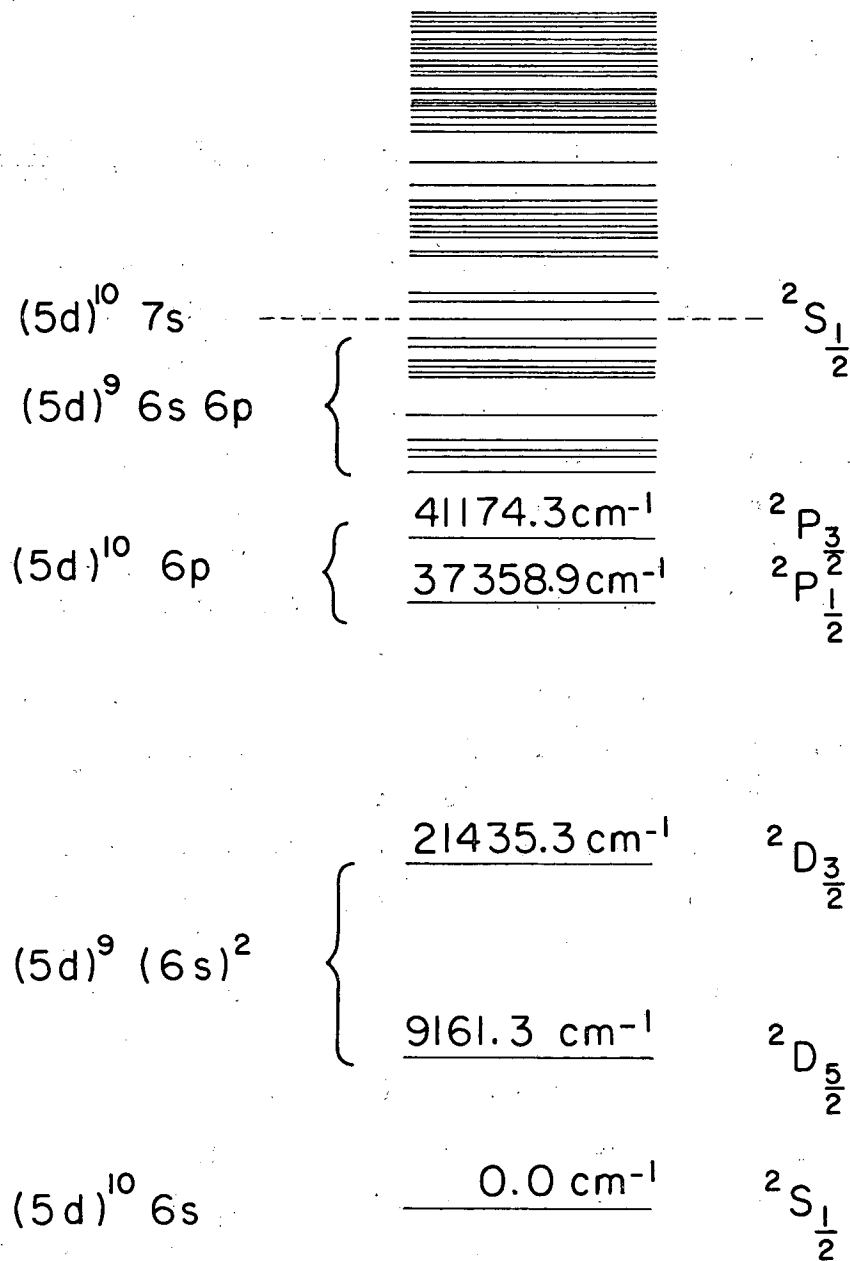
The treatment of the perturbation $\mathcal{H} - \mathcal{H}_{central}$ depends on the relative strengths of the electrostatic repulsion and spin-orbit interactions. If $e^2/r_{ij} >> \xi_i(r_i) \vec{\ell}_i \cdot \vec{s}_i$, the spin-orbit term can be considered as a further perturbation and the electrostatic repulsion can be treated first. The total orbital and spin angular momenta are defined by $\vec{L} = \sum_i \vec{\ell}_i$ and $\vec{S} = \sum_i \vec{s}_i$. It is easily shown that $\vec{L}$ and $\vec{S}$ commute with $\sum (e^2/r_{ij})$. Thus $\vec{L}$ and S are good quantum numbers and can be used to specify the energy levels produced by the electrostatic-repulsion interaction. These energy levels are called terms and are labelled by ^{2S+1}L in standard spectroscopic notation. Spherical symmetry implies that these energy levels are independent of $\vec{M_L}$ and M_S, and hence the degeneracy of a term is $(2L+1)(2S+1)$. Neither $\vec{L}$ nor $\vec{S}$ commutes with the further perturbation $\sum \xi_i(r_i) \vec{\ell}_i \cdot \vec{s}_i$ but their vector sum $\vec{J} = \vec{L} + \vec{S}$ does. Thus, the spin-orbit interaction splits each term into multiplets labelled $^{2S+1}L_J$. The degeneracy of a multiplet is $2J+1$.

The coupling scheme just described is called L-S or Russell-Saunders coupling. If $e^2/r_{ij} << \xi_i(r_i) \vec{\ell}_i \cdot \vec{s}_i$, the appropriate coupling scheme is called j-j coupling. For each electron, $\vec{\ell}_i$ and s_i are coupled to form a resultant $\vec{j}_i = \vec{\ell}_i + \vec{s}_i$, and the total angular momentum is defined by $\vec{J} = \sum_i \vec{j}_i$. The spin-orbit interaction is treated first and the electrostatic repulsion interaction second. In actual practice, neither coupling scheme applies and both interactions have to be diagonalized simultaneously. But $\vec{J}$ is always a good quantum number since it commutes with $\mathcal{H}$. Figure 1 shows the lower fine-structure energy levels of gold.[15]

The addition of an external magnetic field introduces the perturbation Hamiltonian

$$\mathcal{H}_{mag} = -\mu_0 (g_\ell \vec{L} + g_s \vec{S}) \cdot \vec{H}, \tag{4}$$

where the g factors are defined by the general rule $\vec{\mu}_X = \mu_0 g_X \vec{X}$, and μ_0 is the Bohr magneton. The degeneracy in M_J is lifted, and for magnetic fields less than $10^5 G$ the energy levels are given by:

$(5d)^{10}$ 7s $\quad$ --------------------------------------- $\quad$ $^2S_{\frac{1}{2}}$

$(5d)^9$ 6s 6p

$(5d)^{10}$ 6p $\quad\Big\{$ $\quad$ 41174.3 cm^{-1} $\quad$ $^2P_{\frac{3}{2}}$

$\quad$ 37358.9 cm^{-1} $\quad$ $^2P_{\frac{1}{2}}$

$(5d)^9$ $(6s)^2$ $\quad\Big\{$ $\quad$ 21435.3 cm^{-1} $\quad$ $^2D_{\frac{3}{2}}$

$\quad$ 9161.3 cm^{-1} $\quad$ $^2D_{\frac{5}{2}}$

$(5d)^{10}$ 6s $\quad$ 0.0 cm^{-1} $\quad$ $^2S_{\frac{1}{2}}$

MUB-10141

Fig. 1. Atomic fine-structure energy levels of gold.

$$\langle LSJM_J | \mathcal{H}_{mag} | LSJM_J \rangle = - g_J \mu_0 H M_J$$

where the g factor is given by:

$$g_J = g_\ell \frac{J(J+1) - S(S+1) + L(L+1)}{2J(J+1)} + g_s \frac{J(J+1) - L(L+1) + S(S+1)}{2J(J+1)} . \tag{5}$$

For a $^2S_{1/2}$ state, such as the ground state of gold, Eq. (5) yields the value $g_J = g_s$.* The fact that this is not the experimentally observed value for atoms in $^2S_{1/2}$ states is due to several causes.

By far the largest correction to the value $g_J = -2$ is that caused by the anomalous magnetic-dipole moment of the free electron, that is, the fact that for a free electron $g_s \neq -2$. For g_s the latest theoretical value from quantum electrodynamics is -2.0023192 (Ref. 16) and the best experimental value is $-2.002319244(54)$ (Ref. 17). Writing $g_J = \Delta g - 2$ for the correction from quantum electrodynamics, we get $(\Delta g)_{QE} = -0.0023192$.

Phillips has considered the effect of the motion of the nucleus.[18] This finite nuclear-mass effect will change the value of g_ℓ slightly, but for $^2S_{1/2}$ states this correction is irrelevant because $L = 0$.

The only relativistic correction to g_J relevant to $^2S_{1/2}$ states is that described by Margenau.[19] He determined the energy of a charged particle in a weak magnetic field and evaluated $\partial E / \partial H$ to obtain the magnetic moment. Dirac's equation was the basis of the calculation. Margenau showed that

$$(\Delta g)_M = (4/3) \langle T \rangle / mc^2 \tag{6}$$

where $\langle T \rangle$ is the average kinetic energy of the valence electron.

Lamb (L) considered the effect on g_J of internal diamagnetic fields in the atom.[20] Using a Fermi-Thomas model he showed that

$$(\Delta g)_L = (2/3) \langle T - W \rangle / mc^2 \tag{7}$$

where T and W are the kinetic and total energy, respectively, of the valence

---

*Because the Dirac theory of the electron predicts that it should have a magnetic moment of 1 Bohr magneton, g_s equals -2.

electron. To estimate the value of $(\Delta g)_L$, Lamb used the approximation $T + W \approx W_0 - W$, where $W_0 = - e^2/2a_0 n_0^2$ is the hydrogenic value of the energy and $W = - e^2/2a_0 n_0^2$ is actual energy.[†] Doing so for the Margenau (M) corrections as well, we obtain

$$(\Delta g)_M = \frac{10.64}{3} \left\{ \frac{2}{n_0^2} - \frac{1}{n^2} \right\} \times 10^{-5} \qquad (8)$$

$$(\Delta g)_L = \frac{5.32}{3} \left\{ \frac{1}{n_0^2} - \frac{1}{n^2} \right\} \times 10^{-5} . \qquad (9)$$

Phillips considered the effect of configuration mixing on g_J (Ref. 21). Her calculation was restricted to the alkalis. If configurations of the form $(np)^5 (n_0 s) (n' p)$ are mixed with the ground-state configuration $(n_0 s)$, where $n = n_0 - 1$, $n' \geqslant n_0$, then g_J is changed by an amount Δg for each configuration mixed in. Her expression for Δg is

$$(\Delta g)_{CM} = \sum_{i,k} (V_{oi} \xi_{ik}/E_{oi} E_{ok})^2 \delta g , \qquad (10)$$

where CM means configuration mixing, V_{oi} is the matrix element of the electrostatic interaction between the ground state o and the state i having a different configuration but the same L and S values, ξ_{ik} is the matrix element of the spin-orbit interaction between the state i and the state k of the same configuration but having different L and S, E_{oi} and E_{ok} are the energy differences between the state o and the states i and k, and δg is g_J for the state k minus g_J for the state o. Although $(\Delta g)_{CM}$ is a fourth-order effect, it increases rapidly with Z. The spin-orbit parameter for the jumping p electron varies as Z^4, whereas the excitation energy varies only as Z^2. Since the ratio ξ_{ik}/E_{ok} varies slowly with Z, we estimate Δg to vary roughly as Z^2.

B. Hyperfine Structure

The electrostatic interaction between the electrons and the nucleus can be written as

$$\mathcal{H}_e = \iint \frac{\rho_e \rho_n}{|\vec{r}_e - \vec{r}_n|} d^3 r_e \, d^3 r_n , \qquad (11)$$

[†] In these expressions, n is the principal quantum number, n_0 is the effective principal quantum number, and a_0 is the radius of the first Bohr orbit.

where ρ_e is $-e\Psi_e^*\Psi_e$ and ρ_n is $e\Psi_n^*\Psi_n$. If only stationary currents are considered, Ramsey shows that the magnetic interaction can be written as:[10]

$$\mathcal{H}_m = \iint \frac{(\vec{\nabla}_e \cdot \vec{M}_e)(\vec{\nabla}_n \cdot \vec{M}_n)}{|\vec{r}_e - \vec{r}_n|} \, d^3r_e \, d^3r_n \, , \tag{12}$$

where M_e and M_n are the vector potentials from which the current densities $\vec{j}_e$ and $\vec{j}_n$ can be derived. Expanding $|\vec{r}_e - \vec{r}_n|^{-1}$ in spherical harmonics and applying the addition theorem yields the Hamiltonian $\mathcal{H}_{hfs} = \mathcal{H}_e + \mathcal{H}_m$, where $\mathcal{H}_e$ is given as follows:

$$\mathcal{H}_e = \sum_{k=0}^{\infty} \sum_{\mu=-k}^{k} (-1)^{\mu} Q_{\mu}^{(k)}(n) \, F_{-\mu}^{(k)}(e), \tag{13}$$

and the spherical tensors are given by

$$Q_{\mu}^{(k)} = \left(\frac{4\pi}{2k+1}\right)^{1/2} \int r_n^k \, \rho_n \, Y_{\mu}^k(\theta_n, \phi_n) \, d^3r_n \tag{14}$$

$$F_{\mu}^{(k)} = \left(\frac{4\pi}{2k+1}\right)^{1/2} \int r_e^{-k-1} \, \rho_e \, Y_{\mu}^k(\theta_e, \phi_e) \, d^3r_e \, . \tag{15}$$

Now $\mathcal{H}_m$ has precisely the same form except that ρ_e and ρ_n are replaced by $(\vec{\nabla}_e \cdot \vec{M}_e)$ and $(\vec{\nabla}_n \cdot \vec{M}_n)$, respectively.

The diagonal-matrix elements of an operator of the form of (13) are easily obtained in an $|IJFM_F\rangle$ representation where the nuclear angular momentum $\vec{I}$ and electronic angular momentum $\vec{J}$ are coupled to a resultant $\vec{F} = \vec{I} + \vec{J}$, with $|I - J| \leq F \leq I + J$:

$$\langle IJFM_F |\mathcal{H}_e| IJFM_F \rangle = \sum_{k=0}^{\infty} (-1)^{I+J+F} \left\{ \begin{array}{ccc} I & J & F \\ J & I & k \end{array} \right\} \langle I \, ||Q^{(k)}||\, I \rangle \langle J \, ||F^{(k)}||\, J \rangle . \tag{16}$$

The parities of $Q^{(k)}$ and $F^{(k)}$ are $(-1)^k$ in the electric case and $(-1)^{k+1}$ in the magnetic case because ρ is a scalar and $\vec{\nabla} \cdot \vec{M}$ is a psuedoscalar. These parities imply that all odd electric-multipole moments and all even magnetic-multipole moments vanish. Of course, we assume that the nuclear and electronic states are states of definite parity. The

above series is further simplified by the triangular conditions on the 6-j symbol which require that $k \leqslant \min(2I, 2J)$. Thus, for gold the only hfs interaction that is relevant to the hyperfine structure of the $^2S_{1/2}$ ground state is the magnetic-dipole interaction.

The magnetic-dipole interaction between a single unpaired s electron and the nucleus was shown by Fermi to be given by[22]

$$\mathcal{H}_{hfs} = ha\, \vec{I} \cdot \vec{J}, \qquad \text{with } ha = -(8\pi/3)g_I g_J \mu_0^2 \left| \Psi(0) \right|^2, \tag{17}$$

where g_I is the nuclear g factor, $\left| \Psi(0) \right|^2$ gives the density of the s electron at the nucleus, and the other quantities have been previously defined. Fermi used the Dirac equation as the basis for his calculation; a more elegant, simplified derivation was obtained by Nierenberg.[11] Substituting for $\left| \Psi(0) \right|^2$ we obtain the expression

$$ha = -\frac{8}{3} g_I g_J \mu_0^2 \, \frac{ZZ_0^2}{a_0^3 n_0^3} \left(1 - \frac{d\sigma}{dn}\right) F_r(1/2, Z), \tag{18}$$

where a_0 is the radius of the first Bohr orbit, Z_0 is the effective atomic charge, n is the principal quantum number, σ is the quantum defect, n_0 equals $n - \sigma$, F_r is the relativistic correction of Racah,[23] and the other quantities have been previously defined.

Since
$$\vec{F}^2 = (\vec{I} + \vec{J})^2 = \vec{I}^2 + 2\vec{I} \cdot \vec{J} + \vec{J}^2, \tag{19}$$

in an $\left| IJFM_F \right\rangle$ representation we have

$$\left\langle IJFM_F \left| ha\, I \cdot J \right| IJFM_F \right\rangle = \frac{ha\left[F(F+1) - I)I+1) - J)J+1)\right]}{2}. \tag{20}$$

The hfs separation is defined by $\Delta\nu = a[I + (1/2)]$ and is equal to the energy difference expressed in MHz between the states $F = I + (1/2)$ and $F = I - (1/2)$. This means a is expressed in MHz also.

The addition of an external magnetic field destroys the spherical symmetry and lifts the degeneracy in M_F. The appropriate Hamiltonian is

$$\mathcal{H} = ha\, \vec{I} \cdot \vec{J} - g_I \mu_0 \vec{I} \cdot \vec{H} - g_J \mu_0 \vec{J} \cdot \vec{H}. \tag{21}$$

At low fields ($\mu_0 g_J H \ll h\Delta\nu$) where $\vec{I}$ and $\vec{J}$ are coupled to a resultant $\vec{F}$, the energy is given by

$$\langle IJFM_F | \mathcal{3C} | IJFM_F \rangle = \frac{ha[\,F(F+1)-I(I+1)-J(J+1)\,]}{2} - g_F \mu_0 H M_F , \tag{22}$$

where

$$g_F = g_J \frac{F(F+1) - I(I+1) + J(J+1)}{2F(F+1)} + g_I \frac{F(F+1) - J(J+1) + I(I+1)}{2F(F+1)} . \tag{23}$$

At high fields ($g_J \mu_0 H \gg h\Delta\nu$) I and J are decoupled, and in an $|IM_I J M_J\rangle$ representation the energy is given by

$$\langle IM_I J M_J | \mathcal{3C} | IM_I J M_J \rangle = ha M_I M_J - g_I \mu_0 H M_I - g_J \mu_0 H M_J . \tag{24}$$

The general case of intermediate field and coupling is easily solved in either representation if $J = 1/2$. The energy matrix splits up along the diagonal into a series of 2×2 matrices, each of which corresponds to a value of $M_F = M_I + M_J$, and each of which in an $|IM_I J M_J\rangle$ representation has the form:

$$
\begin{array}{cc}
\left| I, M_F - \tfrac{1}{2}, \tfrac{1}{2}, \tfrac{1}{2} \right\rangle & \left| I, M_F + \tfrac{1}{2}, \tfrac{1}{2}, -\tfrac{1}{2} \right\rangle \\
\end{array}
$$

$$
\left\{
\begin{array}{cc}
\dfrac{ha}{2}(M_F - \tfrac{1}{2}) - g_I \mu_0 H(M_F - \tfrac{1}{2}) - \tfrac{1}{2} g_J \mu_0 H & \dfrac{ha}{2}\left(I(I+1) - M_F^2 + \tfrac{1}{4}\right)^{1/2} \\[4mm]
\dfrac{ha}{2}\left(I(I+1) - M_F^2 + \tfrac{1}{4}\right)^{1/2} & -\dfrac{ha}{2}(M_F + \tfrac{1}{2}) - g_I \mu_0 H(M_F + \tfrac{1}{2}) + \tfrac{1}{2} g_J \mu_0 H
\end{array}
\right\}
$$

The quadratic secular equation which results can be solved to yield the Breit-Rabi formula

$$W(F, M_F) = \frac{h\Delta\nu}{2(2I+1)} - g_I \mu_0 H M_F + (F - I)h\Delta\nu \left(1 + \frac{4M_F X}{2I+1} + X^2\right)^{1/2} , \tag{25}$$
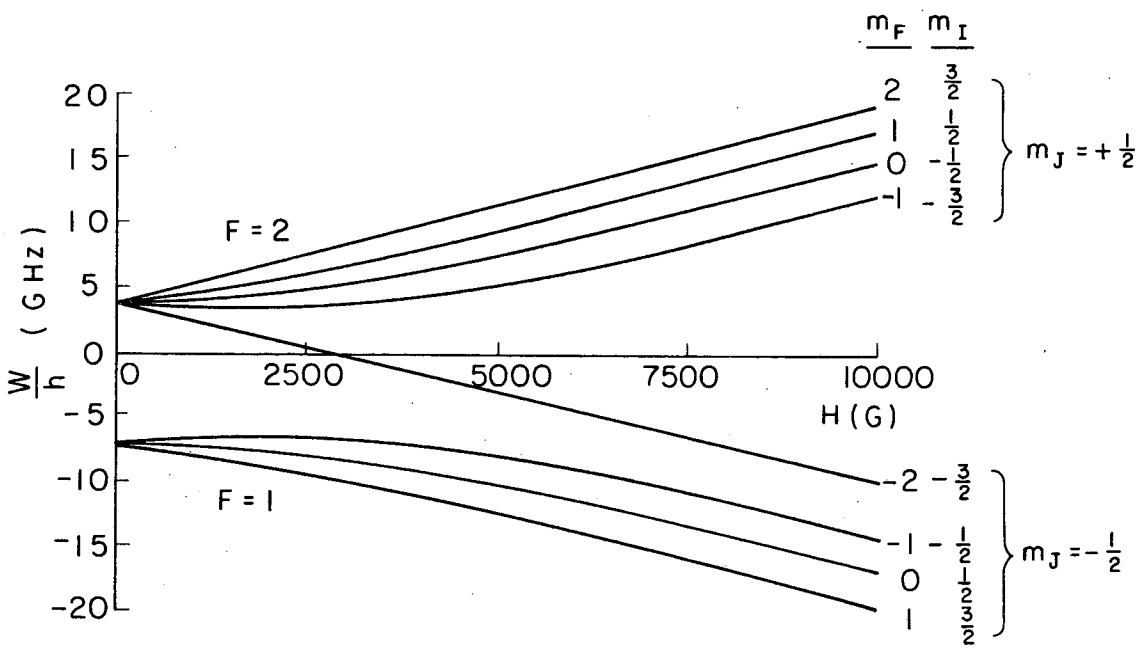
where $X = (g_I - g_J)\mu_0 H / h\Delta\nu$. The Breit-Rabi diagrams for Au[198] and Au[199] are given in Figs. 2 and 3, respectively.
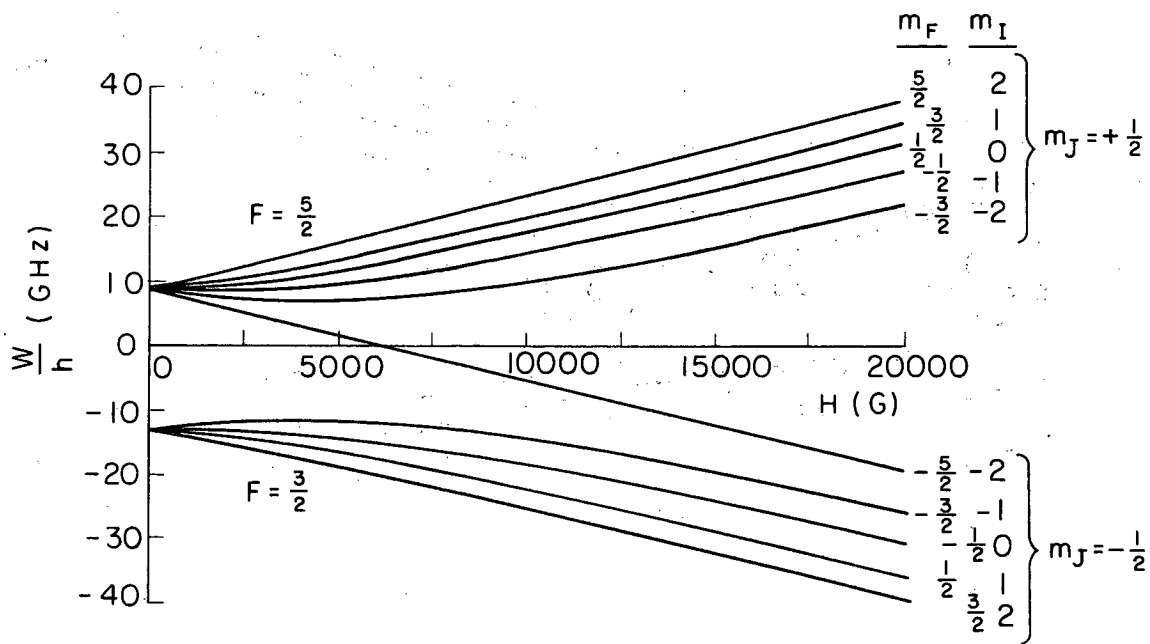
Fig. 2. Breit-Rabi diagram for Au^{198} (I = 2, J = 1/2).

Fig. 3. Breit-Rabi diagram for Au^{199} (I - 3/2, J = 1/2).

MU-B-10143

C. Higher-Order Corrections

The treatment of the hyperfine structure presented in Sec. II. B is a first-order perturbation-theory calculation. Since the operators involved are not spherically symmetric, I and J are not strictly good quantum numbers and contributions to the hyperfine structure from states of differing I and J should be considered. The nuclear-energy-level spacings are of the order of hundreds of keV, whereas the electronic-energy-level spacings are of the order of eV. This means we need consider the breakdown of J only.

Foley was the first to point out the importance of second-order corrections for the interpretation of nuclear g factors as measured by atomic beams.[24] His paper and a later relativistic one by Clendenin[25] described the perturbation of the hfs levels of a $^2P_{1/2}$ state by a nearby $^2P_{3/2}$ state. The result is that the hyperfine structure of the $^2P_{1/2}$ state can be described by the Breit-Rabi formula but with a $(^2P_{1/2})$ replaced by $a' = a(^2P_{1/2}) +$ correction terms, and g_I replaced by $g_I' = g_I +$ correction terms. Neither analysis applies to gold, but in view of the large hyperfine structure observed in Au^{198} and Au^{199} it is worthwhile to examine the matter of second-order effects in more detail.

In general, the second-order contributions to the energy of the ground-state hyperfine-structure level $|IJFM_F\rangle$ from excited-state hyperfine-structure levels $|IJ'FM_F\rangle$ will be given by:

$$\sum_{J'} |\langle IJFM_F |\mathcal{H}| IJ'FM_F\rangle|^2/(E_J - E_{J'})$$ (26)

where

$$\mathcal{H} = M^{(1)} \cdot N^{(1)} + Q^{(2)} \cdot F^{(2)} - \mu_0(\vec{L} + 2\vec{S}) \cdot \vec{H}$$ (27)

and where the scalar product of the tensors has the usual definition

$$T^{(k)} \cdot T^{(k)} = \sum_{\mu=-k}^{k} (-1)^\mu T^{(k)}_{-\mu} T^{(k)}_{\mu} .$$

Interactions higher than the electric quadrupole will be ignored.

The evaluation of (26) with all its terms for all excited states could be a hopelessly tedious job. However, certain rules and approximations simplify the calculation for gold. First, the states $|IJFM_F\rangle$ and $|IJ'FM_F\rangle$ must have the same parity. Second, $|J - J'| \leqslant k \leqslant J + J'$, where k is the order of the operators appearing in the various matrix elements. For (27), the fact that k takes on the values 1 and 2 implies that J' can only take on the values 3/2 and 5/2.

All of the terms involving the magnetic field will contain the matrix element

$$\langle IJFM_F | L_z + 2S_z | IJ'FM_F \rangle$$

$$= (-1)^{I+J+1+2F-M_F} \begin{pmatrix} F & 1 & F \\ -M_F & 0 & M_F \end{pmatrix} (2I+1) \begin{Bmatrix} F & 1 & F \\ J' & I & J \end{Bmatrix} \langle J ||L_z + 2S_z|| J' \rangle \ .$$

(28)

The reduced matrix element has the selection rules $\Delta L = 0$, $\Delta S = 0$ since neither L_z nor S_z can change L or S. Furthermore, because the reduced matrix element will contain $\int_0^\infty R_{6s} R_{n\ell} r^2 dr$ as a factor, Δn is required to be zero. The same reduced matrix element results, of course, from evaluating $L_z + 2S_z$ in an $|IM_I J M_J \rangle$ representation:

$$\langle IM_I J M_J | L_z + 2S_z | IM_I J' M_{J'} \rangle = (-1)^{J-M_J} \begin{pmatrix} J & 1 & J' \\ -M_J & 0 & M_J \end{pmatrix} \langle J ||L_z + 2S_z|| J' \rangle \ . (29)$$

The result of all these selection rules is that the second-order corrections involving the magnetic field vanish for all excited states of gold. The $\Delta n = 0$ rule restricts the calculation to the levels of the ground-state configuration, and the ground-state configuration of gold leads to only one fine-structure level.

The remaining correction terms involve the squares of and the product of the matrix elements $\langle IJFM_F | M^{(1)} \cdot N^{(1)} | IJ'FM_F \rangle$ and $\langle IJFM_F | G^{(2)} \cdot F^{(2)} | IJ'FM_F \rangle$. Nonrelativistically, these matrix elements will vanish for the following reason. Both matrix elements contain $\int_0^\infty R_{6s} \frac{1}{r^3} R_{n\ell} r^2 dr$ as a factor. The only excited states allowed consideration by the parity-selection rule and the restriction on J' are $^2D_{3/2}$ and $^2D_{5/2}$ states. These states correspond to the configurations $(nd)^9 n's$ which occur in the electronic structure of gold. A rule by Pasternak and Sternheimer[26] is that

$$\int_0^\infty R_{n\ell} \frac{1}{r^s} R_{n\ell'} r^2 dr = 0 \quad \text{if } s = 2, 3, \cdots \ell' - \ell + 1, \ \ell' > \ell \ . \tag{30}$$

Since R_{ns} differs from R_{6s} only by a constant near the nucleus where the

important contributions to the integral occur, we have [using (30)]:

$$\int_0^\infty R_{6s} \frac{1}{r^3} R_{nd} r^2 dr = (const) \int_0^\infty R_{ns} \frac{1}{r^3} R_{nd} r^2 dr = 0 . \tag{31}$$

This result need not be true relativistically so we will calculate the corrections following Schwartz.[27,28] The magnetic-dipole interaction can connect the $^2S_{1/2}$ ground state only with $^2D_{3/2}$. The matrix element of interest is

$$\langle I \tfrac{1}{2} FM_F | M^{(1)} \cdot N^{(1)} | I \tfrac{3}{2} FM_F \rangle = (-1)^{I+\frac{1}{2}+F} \begin{Bmatrix} I & 1/2 & F \\ 3/2 & I & 1 \end{Bmatrix}$$

$$\langle I \| M^{(1)} \| I \rangle \langle \tfrac{1}{2} \| N^{(1)} \| \tfrac{3}{2} \rangle . \tag{32}$$

The reduced matrix element in the electronic coordinates has as a factor

$$\int_0^\infty (fg' + f'g) r^{-2} dr$$ where the prime refers to the excited state, f and g

are the Dirac radial functions satisfying

$$(\frac{d}{dr} - \frac{\kappa}{r})f = \frac{1}{hc} (mc^2 + E + eV_c)g$$

$$(\frac{d}{dr} - \frac{\kappa}{r})g = \frac{1}{hc} (mc^2 - E - eV_c)f, \tag{33}$$

κ is the Dirac quantum number equal to $j+\frac{1}{2}$ if $j = \ell + \frac{1}{2}$ or $-(j+\frac{1}{2})$ if $j = \ell - \frac{1}{2}$, and C is a normalization constant. If zero binding energy is assumed ($V_c = Ze^2/r \ll mc^2$), a solution to (33) can be obtained in terms of Bessel functions, $\quad f = C[\frac{x}{2} J_{2\rho+1}(x) - (\rho+\kappa)J_{2\rho}(x)] \tag{34}$

$$g = \alpha Z C[J_{2\rho}(x)] , \tag{35}$$

where $\rho = (\kappa^2 - \alpha^2 Z^2)^{1/2}$, $x = (8Zr/a_0)^{1/2}$, and α is the fine-structure constant. This approximation should be good since the integrals to be calculated have major contributions near the nucleus where the potential is given by Ze/r^2. Using the formula

$$\int_0^\infty \frac{J_\mu(t)J_\nu(t)dt}{t^\lambda} = \frac{\Gamma(\lambda)}{2^\lambda} \frac{\Gamma(\frac{\mu+\nu-\lambda+1}{2})}{\Gamma(\frac{\mu+\nu+\lambda+1}{2})\Gamma(\frac{\mu-\nu+\lambda+1}{2})\Gamma(\frac{\nu-\mu+\lambda+1}{2})} , \quad (36)$$

we can show that

$$\int_0^\infty (fg'+f'g)r^{-k}dr = 2(8Z/a_0)^{k-1}C_\kappa C_{\kappa'}aZ\Gamma(2k)2^{-2k-1}$$

$$\times \frac{\Gamma(\rho+\rho'+1)}{\Gamma(\rho+\rho'+k+1)\Gamma(\rho'-\rho+k)\Gamma(\rho-\rho'+k)} \left\{\frac{-2k(k+\kappa+\kappa')}{(\rho-\rho'+k)(\rho'-\rho+k)}\right\} , \quad (37)$$

where ρ, κ are associated with f and g, and ρ', κ' are associated with f' and g'. For the particular matrix element of interest we have $k = 1$, $\kappa = 1$, $\kappa' = -2$, so that $k+\kappa+\kappa' = 0$ and the matrix element vanishes.

This leaves only the second-order quadrupole contributions to the hyperfine structure of the ground state from $^2D_{3/2}$ and $^2D_{5/2}$ excited states to be calculated. Evaluating the 6-j symbols and reduced matrix elements, we obtain:

for $I = 3/2$

$$\Delta\nu_{2nd\ order} = \frac{4e^4Q^2}{25h} \left\{\frac{(III)^2}{\Delta E_{III}} - \frac{(II)^2}{\Delta E_{II}}\right\} \quad (38)$$

for $I = 2$

$$\Delta\nu_{2nd\ order} = \frac{7e^4Q^2}{80h} \left\{\frac{(III)^2}{\Delta E_{III}} - \frac{(II)^2}{\Delta E_{II}}\right\} \quad (39)$$

where

$$\Delta\nu = \Delta\nu_{1st\ order} + \Delta\nu_{2nd\ order}.$$

$$(II) = 2C_1C_{-2}(8Z/a_0)^2 \int_0^\infty (f_1f_{-2} + g_1g_{-2}) r^{-3}dr$$

$$(III) = 2C_1C_3(8Z/a_0)^2 \int_0^\infty (f_1f_3 + g_1g_3)r^{-3}dr$$

and

$$\Delta E_{II} = E(^2S_{1/2}) - E(^2D_{3/2}), \quad \Delta E_{III} = E(^2S_{1/2}) - E(^2D_{5/2}).$$

The subscript on C refer to the Dirac quantum number κ.

The normalization constants C_1, C_{-2}, and C_3 are evaluated by fitting the diagonal-matrix elements of the magnetic-dipole interaction to the observed magnetic hyperfine structure in Au^{197} of the states $^2S_{1/2}, ^2D_{3/2}$, and $^2D_{5/2}$.[8,9] If we assume a quadrupole moment of 1 barn for Au^{198} and Au^{199} and if we consider only the lowest $^2D_{3/2}$ and $^2D_{5/2}$ states, we get:

for Au^{198}

$$\Delta\nu_{\text{2nd order}} = -34 \text{ Hz}$$

for Au^{199}

$$\Delta\nu_{\text{2nd order}} = -61 \text{ Hz} .$$

Ignoring the uncertainty in Q, we think it unlikely that the calculation is good to better than 10%. Because the nuclear quadrupole moment of Au^{197} is 0.6 barn (Ref. 8), we also think it unlikely that the quadrupole moments of Au^{198} and Au^{199} are larger than 1.0 barn. Contributions from higher $^2D_{3/2}$ and $^2D_{5/2}$ states will fall off rapidly due to increasing energy denominators and decreasing matrix elements. It is safe to say that the second-order quadrupole contributions to the ground-state hyperfine structure of gold are completely negligible with respect to present measurements for isotopes 197, 198, and 199, and very likely for all the other isotopes as well.

D. Nuclear Shell Model and Configuration Mixing

A nuclear model that has explained a great body of empirical facts and that seems applicable to the gold nuclei is the shell model. In this model, the nucleons are assumed to move independently of one another in some spherically symmetric potential U(r). This potential is usually taken to be somewhere between the simple harmonic-oscillator potential and the infinite square-well potential. In addition, a strong negative spin-orbit interaction is assumed. This model leads to the energy levels of Fig. 4. The states are labelled by the quantum numbers $|n\ell j\rangle$ where n is the number of nodes in the radial part of the wave function (including that at the origin) minus ℓ, ℓ is the orbital angular momentum, and $j = \ell \pm \frac{1}{2}$. Degeneracy in m_j means each level can

3 d

2 g

1 i

126

3 p

2 f

1 h

82

3 s

2 d

1 g

50

2 p

1 f

28

20

1 d
2 s

8

1 p

1 s

$3/2$
$7/2$
$5/2$
$11/2$
$9/2$

$11/2$

$1/2$ $3/2$
$13/2$ $3/2$
$13/2$ $5/2$

$1/2$ $13/2$
$3/2$

$5/2$

$7/2$ $9/2$

$9/2$
$7/2$

$1/2$ $3/2$
$11/2$ $3/2$
$11/2$ $5/2$
$7/2$

$1/2$ $3/2$
$11/2$
$7/2$ $5/2$

$9/2$ $1/2$
$5/2$ $1/2$
$5/2$ $3/2$

$9/2$ $1/2$
$5/2$ $3/2$

$7/2$

$7/2$

$3/2$

$1/2$
$5/2$

$3/2$

$1/2$
$5/2$

$1/2$
$3/2$

$1/2$
$3/2$

$1/2$

$1/2$
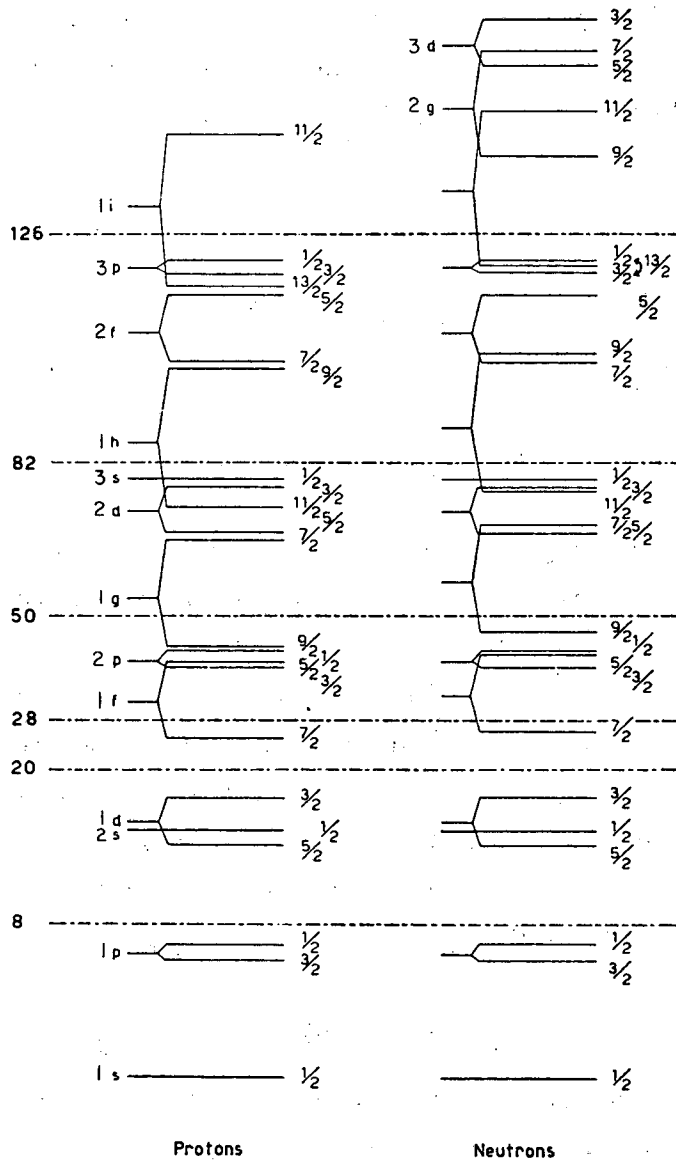
Protons

Neutrons

MU – 21466 (a)

Fig. 4. Nuclear shell-model energy levels.

be occupied by $2j+1$ protons and $2j+1$ neutrons. The energy levels in the protons having larger angular momentum are depressed slightly to take the Coulomb repulsion into account. As can be seen from Fig. 4, the model yields the so-called magic numbers at closed shells of 2, 8, 20, 28, 50, 82, and 126 nucleons. Nuclei containing these numbers of neutrons or protons are unusually stable.

The nucleons couple their angular momenta by j-j coupling to a resultant angular momentum or spin I. Closed shells of nucleons have zero spin. Usually the nucleons cancel angular momenta in pairs and the spin of odd-A nuclei is that of the last odd nucleon. For odd-odd nuclei the coupling rules of Nordheim as modified by Brennan and Bernstein account for many observed odd-odd spins:[29]

a) for particle-particle or hole-hole coupling:

$$\text{if } j_p = \ell_p \pm \tfrac{1}{2} \, , \ j_n = \ell_n \pm \tfrac{1}{2} \ \text{(weak coupling) then } I = \left| j_n \pm j_p \right|$$

$$\text{if } j_p = \ell_p \pm \tfrac{1}{2} \, , \ j_n = \ell_n \mp \tfrac{1}{2} \ \text{(strong coupling) then } I = \left| j_n - j_p \right| \, .$$

$$(40)$$

b) for particle-hole coupling: $I = \left| j_n + j_p - 1 \right| \, .$ $\qquad (41)$

For weak coupling in a half-filled shell, the ambiguity of a) is removed and $I = \left| j_n - j_p \right|$. Schwartz has shown these rules to have a theoretical basis in a residual proton-neutron force of the form[30]

$$V = - V_0 \left[(1-a) + a \, \vec{s}_1 \cdot \vec{s}_2 \right] \delta(\vec{r}_1 - \vec{r}_2) \qquad \text{with } a \approx 1/10.$$

The magnetic moment of a nucleus as predicted by the shell model is known as the Schmidt moment and is given by

$$\mu_{Sch} = j\left[g_\ell \pm \frac{1}{2\ell+1} (g_s - g_\ell) \right], \quad j = \ell \pm \tfrac{1}{2} \qquad (42)$$

where $g_\ell = 0$ for neutrons, $g_\ell = 1$ for protons, $g_s = -3.82560$ for neutrons, and $g_s = 5.58510$ for protons.

The fact that most observed magnetic moments differ from the Schmidt values has been explained in a number of ways. One approach is that of quenched g factors. The free-nucleon g factors are considered to be modified in the nucleus possibly by the presence of meson-exchange currents.

Table I. Values of a_0 for type I excitations.

Nucleus	I	Type I $a_0(\Delta\ell = 0)$		Contribution from even numbers of
Odd proton (neutron)	$L+\frac{1}{2}$	$\dfrac{n_1(2j_2+1-n_2)\,\ell_1(L+2)}{(2j_2+1)(2L+3)(2\ell_1+1)} \times$	$\dfrac{V_s R}{\Delta E}$	Protons (neutrons)
			$-\dfrac{(V_t-V_s)R}{2\Delta E}$	Neutrons (protons)
	$L-\frac{1}{2}$	$\dfrac{n_1(2j_2+1-n_2)\,\ell_1(L-1)}{(2j_2+1)(2L+1)(2\ell_1+1)} \times$	$-\dfrac{V_s R}{\Delta E}$	Proton (neutron)
			$\dfrac{1}{2}\dfrac{(V_t-V_s)R}{\Delta E}$	Neutron (proton)

Table II. Values of a_2 for type I excitations.

Nucleus	I		Type I $a_2(\Delta\ell = 2)$		Contribution from even numbers of
Odd proton (neutron)	$L+\frac{1}{2}$	$\frac{3}{8}$	$\dfrac{n_1(2j_2+1-n_2)L}{(2L+3)\,(2\ell_>-1)} \times$	$\dfrac{V_s R}{\Delta E}$	Protons (neutrons)
				$-\dfrac{(V_t-V_s)R}{2\Delta E}$	Neutrons (protons)
	$L-\frac{1}{2}$	$\frac{3}{8}$	$\dfrac{n_1(2j_2+1-n_2)(L+1)}{(2L+1)\,(2\ell_>-1)} \times$	$-\dfrac{V_s R}{\Delta E}$	Protons (neutrons)
				$\dfrac{(V_t-V_s)R}{2\Delta E}$	Neutrons (protons)

Table III. a_0 for types II and III excitations.

Type	a_0
II	$-\dfrac{n(2I-p)(L-1)L}{(2I-1)(2L+1)^2}\dfrac{V_s R}{\Delta E}$
III	$\dfrac{(p-1)(2j_1+1-n)(L+1)(L+2)}{(2j_1+1)(2L+1)(2L+3)}\dfrac{V_s R}{\Delta E}$

Table IV. Values of a_2 for types II and III excitations.

Type	I	a_2
II	$L+\frac{1}{2}$	$n(2I-p)\dfrac{3}{8}\dfrac{(L+1)}{(2L+3)^2}\dfrac{V_s R}{\Delta E}\quad j_1 > I$
	$L-\frac{1}{2}$	$-n(2I-p)\dfrac{3}{8}\dfrac{L(L+1)}{(L-1)(4L^2-1)}\dfrac{V_s R}{\Delta E}\quad j_1 < I$
III	$L+\frac{1}{2}$	$\dfrac{3}{8}\dfrac{(p-1)(2j_1+1-n)(L+1)}{(2L+3)^2}\dfrac{V_s R}{\Delta E}\quad j_1 > I$
	$L-\frac{1}{2}$	$-\dfrac{3}{8}\dfrac{(2j_1+1-n)(p-1)(L+1)}{(L-1)(4L^2-1)}\dfrac{V_s R}{\Delta E}\quad j_1 < I$

The hyperfine-structure anomaly has its origin in two effects. First, the nucleus is not a point dipole, as assumed in the derivation of (18), but rather, magnetism is distributed throughout the nuclear volume. The fact that the probability density of the electron is not constant over the nuclear volume renders the magnetic-dipole interaction sensitive to this distribution of nuclear magnetism. This is known as the Bohr-Weisskopf effect.[34] Second, the nucleus is not a point charge, as the use of a Coulomb potential in the electronic Hamiltonian assumes, but charge is distributed throughout the nuclear volume. This modification of the Coulomb potential shifts the atomic energy levels slightly; this is known as the Breit-Rosenthal effect.[35] The relevance of this effect to the hyperfine structure is that it changes the probability density of electrons at the nucleus and hence affects the magnetic-dipole interaction for s electrons (and p electrons considered relativistically). The total effect is expressed by the following definition

$$\frac{a_1}{a_2} = \frac{g_1}{g_2} (1 + {}^1\Delta^2) = \frac{g_1}{g_2} \frac{1 - \delta_1}{1 - \delta_2} \frac{1 + \epsilon_1}{1 + \epsilon_2} . \tag{52}$$

Ordinarily, the ϵ's refer to the Bohr-Weisshopf effect and the δ's to the Breit-Rosenthal effect. In this thesis I shall follow the convention of Stroke et al.,[33] that in calculating ϵ's one uses wave functions based on a distributed-charge potential that varies from isotope to isotope within an element, thus including a portion of the Breit-Rosenthal effect in ϵ. The portion that remains as δ can be ignored since the effect of ϵ on ${}^1\Delta^2$ will be much larger than that of δ unless both isotopes have the same spins and nearly equal magnetic moments.

The calculation of the hfs anomaly proceeds as follows: One calculates relativistically the perturbation of the atomic energy levels produced by the following vector potentials (due to spin and orbital angular momenta) of the nucleons:

$$\vec{A}_s(\vec{r}) = \int \frac{\vec{M}_s(\vec{R}) \times (\vec{r} - \vec{R})}{|\vec{r} - \vec{R}|^3} \, d\vec{R}$$

$$\vec{A}_\ell(\vec{r}) = \int \frac{\Phi^*(\vec{R}) \, \vec{v} \, \Phi(\vec{R})}{|\vec{r} - \vec{R}|} \, d\vec{R} , \tag{53}$$

where $\vec{r}$ and $\vec{R}$ are the position vectors of the electron and the nucleus,

respectively, $\vec{M}_s(\vec{R})$ is the magnetization due to nuclear spin, $\vec{v}$ is the nucleon velocity, and $\Phi(\vec{R})$ is the nuclear wave function.

This calculation yields to first order

$$W = e \int \Psi^*(\vec{r})\vec{\alpha} \cdot \vec{A}\Psi(\vec{r})d\vec{r}, \tag{54}$$

where W is the amount the upper F level is displaced by the interaction, i.e., $W = Ih\Delta\nu/(2I+1)$. Equation (54) is computed with the assumption of first a point nucleus and then a finite nucleus. The relation $W_{ext} = W_{pt}(1 + \epsilon)$ then yields the following expression for ϵ:

$$\epsilon = \left\{ \int\int_{Nuc} \sum_i \Phi^* \left[g_s^i \left(s_z^i \int_0^{R_i} FG\,dr - D_z^i \int_0^{R_i} FG\,\frac{r^3}{R_i^3}\,dr \right) \right. \right.$$

$$\left. \left. + g_\ell^i \ell_z^i \int_0^{R_i} \left(1 - \frac{r^3}{R_i^3}\right) FG\,dr \right] \Phi\,d\tau_N \right\} \left(\mu \int_0^\infty F_0 G_0\,dr \right)^{-1}, \tag{55}$$

where μ is the nuclear magnetic-dipole moment, Φ is the nuclear wave function corresponding to a maximum value of the z component of spin, F_0 and G_0 are the Dirac radial wave functions corresponding to a point nucleus and F and G are those derived from an extended charge distribution. The integration over electronic angular variables has been completed, and

$$D_z^i = \frac{1}{2} \left[s_x^i \frac{3X_i Z_i}{R_i^2} + s_y^i \frac{3Y_i Z_i}{R_i^2} + s_z^i \left(\frac{3Z_i^2 - R_i^2}{R_i^2} \right) \right]. \tag{56}$$

Stroke et al. used a polynomial approximation of a trapezoidal nuclear charge distribution and numerically solved the Dirac equation. The resulting radial functions were used to evaluate (56). The nuclear wave functions they used allowed for configuration mixing as described in Sec. II.D. They obtained the following result for ϵ:

$$-\epsilon = \frac{1}{\mu} \left\{ a_s(sp)g_s \left[(b_s)_2 \left(1+(\tfrac{2}{5})\zeta\right) \mathfrak{I}_1(sp) + (b_s)_4 \left(1+(\tfrac{4}{7})\zeta\right) \mathfrak{I}_2(sp) \right] \right.$$

$$\left. + a_\ell(sp)g_\ell \left[(b_\ell)_2 \mathfrak{I}_1(sp) + (b_\ell)_4 \mathfrak{I}_2(sp) \right] \right]$$

$$+ \sum_i a_0^i \left[\left((b_s)_2 \left(\frac{9}{10} \right) \mathfrak{S}_1(i) + (b_s)_4 \left(\frac{6}{7} \right) \mathfrak{S}_2(i) \right) g_s^i \right.$$

$$\left. - \left((b_\ell)_2 \mathfrak{S}_1(i) + (b_\ell)_4 \mathfrak{S}_2(i) \right) g_\ell^i \right]$$

$$\left. + \sum_i a_2^i \left[\left(\frac{2}{5} \right) (b_s)_2 \mathfrak{S}_1(i) + \left(\frac{4}{7} \right) (b_s)_4 \mathfrak{S}_2(i) \right] g_s^i \right\} , \qquad (57)$$

where $a_s(sp) = \frac{1}{2}$, $a_\ell(sp) = I - \frac{1}{2}$, $\zeta = \frac{2I-1}{4(I+1)}$, for $I = \ell + \frac{1}{2}$;

and $a_s(sp) = \frac{-I}{2I+2}$, $a_\ell(sp) = \frac{I(2I+3)}{2I+2}$, $\zeta = \frac{2I+3}{4I}$, for $I = \ell - \frac{1}{2}$.

The coefficients $(b_s)_n$, $(b_\ell)_n$, and $\mathfrak{S}_n$, $n = 1, 2$, are tabulated by Stroke et al. for many isotopes and excitations. They also give the energy required for each type of excitation. The b coefficients arise from the electronic integration and the $\mathfrak{S}$'s from the nuclear integration. The coefficients a_0 and a_2 are given in Tables I through IV. Having calculated $\epsilon(1)$ and $\epsilon(2)$ corresponding to isotopes (1) and (2) by this procedure, the anomaly $^1\Delta^2$ is calculated with the formula

$$1 + {}^1\Delta^2 = \frac{1 + \epsilon(1)}{1 + \epsilon(2)} . \qquad (58)$$

III. APPARATUS AND EXPERIMENTAL TECHNIQUES

A. Atomic-Beam Apparatus

Figure 5 illustrates schematically the operation of a typical flop-in atomic-beam apparatus. The A and B fields are strongly inhomogeneous, H (at. beam) $\approx$ 10,000 G, $\partial H/\partial z \approx$ 10,000 G/cm, with the fields and gradients pointing in the same direction. Due to the interaction between the field gradients and the magnetic moments of the atoms, atoms are deflected in these fields. For a given small range of angles of emission from the oven, there exists a range of velocities for which the atoms will pass through the collimator. Normally, they will again be deflected in the same direction in the B magnet and thus be thrown out. However, if transitions induced in the C region change the sign of the magnetic moment of the atoms, the atoms will be refocused or flopped-in to the detector. The stop-wire simply prevents fast atoms, which are not strongly deflected, from reaching the detector.

In a flop-out apparatus, the A and B gradients are arranged in opposite directions. In such an apparatus the beam is refocused unless the sign of the magnetic moment is changed in the C region. Although it is usually possible for one to observe more transitions with a flop-out apparatus then with a flop-in one, transitions of atoms with $J = 1/2$ can be observed equally well with either apparatus. For radioactive detection of the beam, the flop-in type is preferred since it provides a signal on top of essentially zero background whereas the flop-out type provides a signal on top of a large background.

Figure 6 illustrates the A and B magnet pole tips. The field produced by such pole tips has been discussed by several authors i.e., Ref. 10. The A and B magnets are powered by 300-V, 5-A, constant-current power supplies.

The ovens, radio-frequency loops, and various beam flags and stops are lined up with an alignment telescope. A reference axis is provided by targets which can be dropped into place externally. The position of these targets is checked periodically, with the A and B magnet pole tips used as reference.

The magnetic field in the C region, which must be as homogeneous as possible, is provided by an electromagnet Varian Associates V4012A

Oven   **A**– Magnet   **C**–Magnet   **B**–Magnet   Detector

H_A H_C H_B

∇H_A $\nabla H_C = 0$ ∇H_B
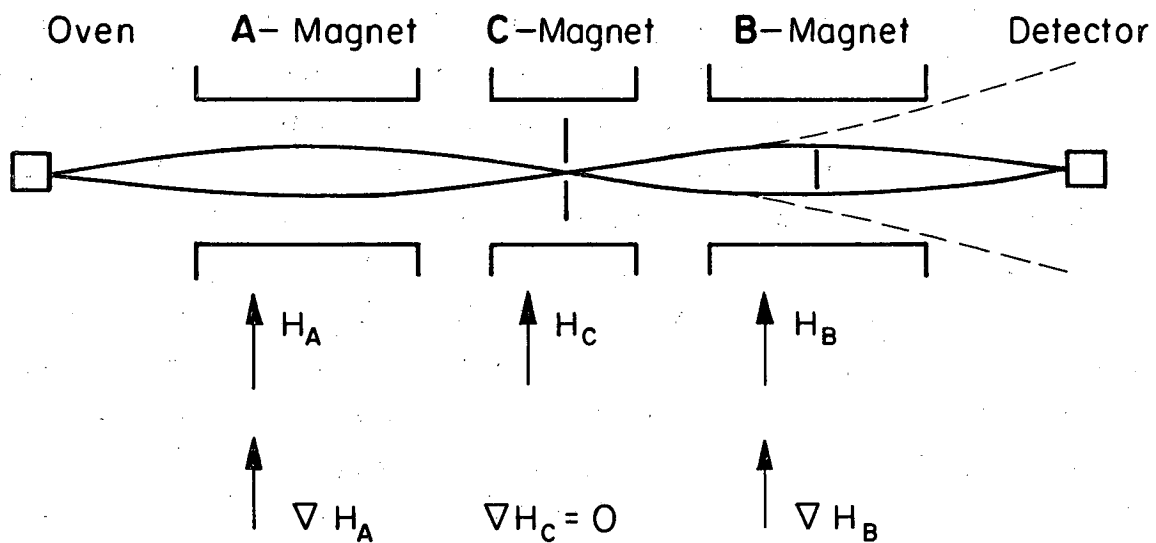
MUB-10144

Fig. 5. Schematic atomic-beam apparatus of the flop-in type.

O $\frac{1}{2}$ I
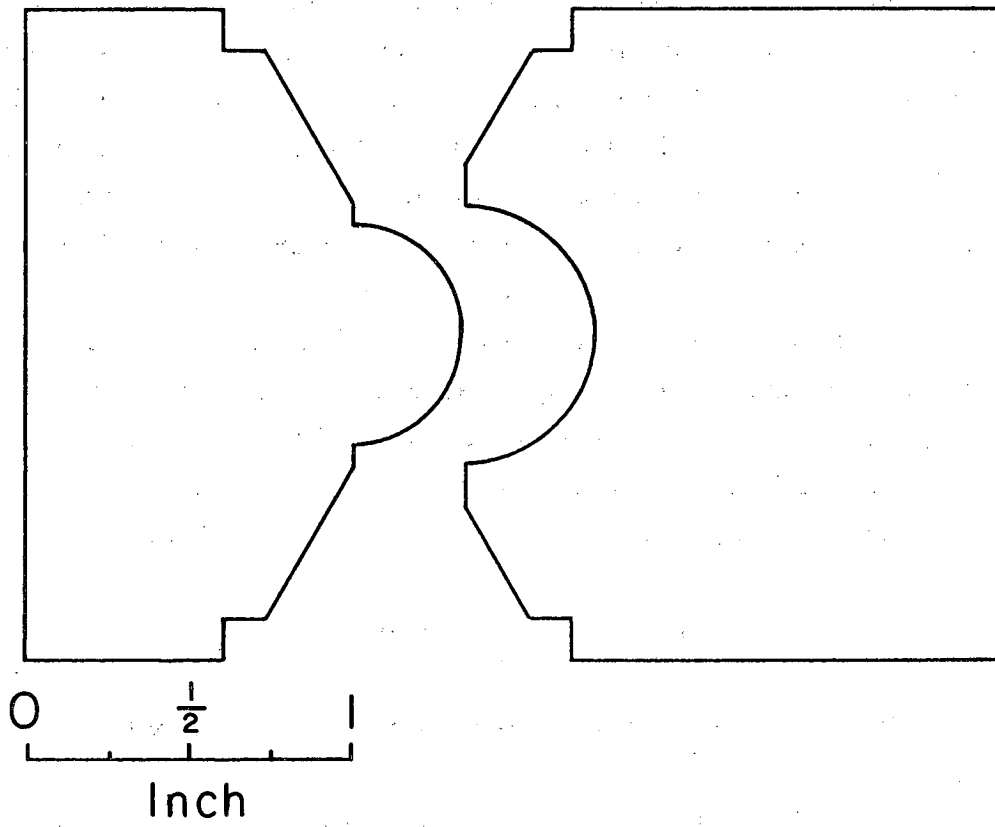
Inch

MUB-10145

Fig. 6. Cross section of the A and B magnet pole tips.

with 12-inch pole tips.   Its constant-current power supply (Varian V2100)
is further controlled by a nuclear magnetic resonance (NMR) field regulator
(Harvey-Wells FC-502).   Proton resonances strong enough for good field
locking were obtained in the range 800 to 7000 G.   The marginal oscillator
used in the NMR locking circuit to provide the proton resonant frequency is
prevented from drifting by weakly coupling it to a very stable oscillator
(Schomandl ND5 and NDF2) at the same frequency.   C field stabilities were
typically a few parts per million per hour.   Figure 7 illustrates the method
of regulation.   The C field was measured for a given experiment or run by
observing the so-called standard $\Delta F = 0$, $\Delta M_J = 1$) transition in either K^{39}
or Cs^{133}.   The accurately known values for all the hfs parameters of these
isotopes then enables one to deduce H from the observed frequency of the
transition.

Figure 8 is an overall view of the experimental area and apparatus.
The various chambers of the apparatus are differentially pumped by oil-dif-
fusion pumps.   Pressures are typically 10^{-6} torr.   Valves permit the pressure
of the oven, buffer, or C-can chambers to be increased to atmospheric pres-
sure and reduced again without shutdown of the diffusion pumps.

B.   Beam Production and Detection

It is not hard to produce beams of gold atoms with sufficient specific
activity in either Au^{198} or Au^{199}.

For Au^{198}, about 0.1 g of small gold chips was irradiated for 16
hours in a neutron flux of 10^{14} neutrons per second per cm^2 in the General
Electric Research Reactor at Vallecitos, California.   Normally 13.0 curies
of activity were produced from the 100% abundant Au^{197} which has a thermal
neutron- capture cross section of 98.8 barns.   These chips were placed di-
rectly in the oven.

For Au^{199}, about 2.5 g of small platinum chips was irradiated for
48 hours in a neutron flux of 10^{14} neutrons per second per cm^2 in the
Vallecitos reactor.   Platinum-199 was thus produced from the 7.21% abundant
Pt^{198}, which has a cross section for thermal-neutron capture of 4 barns.   The
Pt^{199} decays with a half-life of 30 minutes to Au^{199}.   Typically, 2 curies of
gold activity were produced.   The gold was separated from the platinum by
the following process: The reactor sample, along with about 20 mg of stable
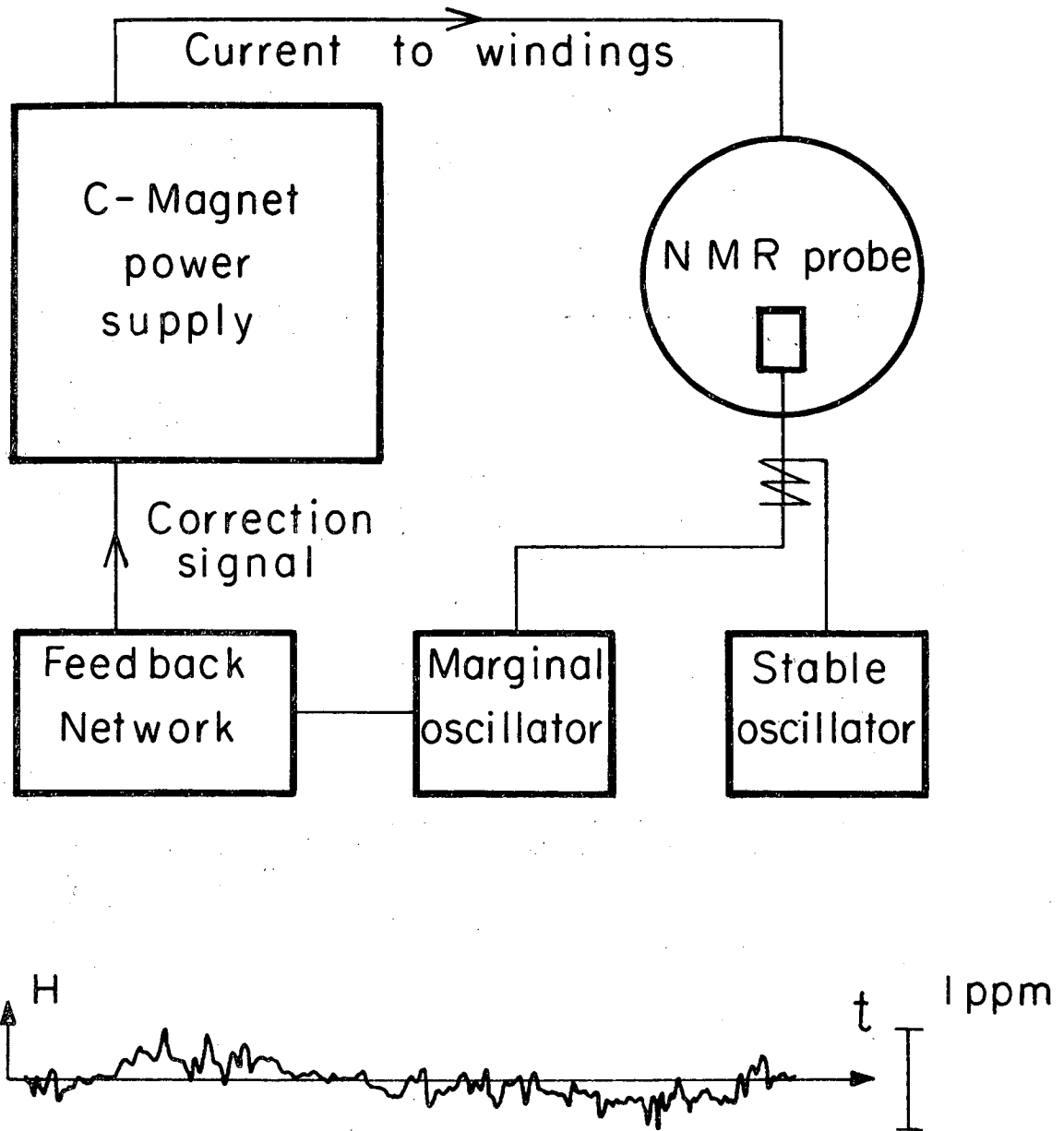
Fig. 7. Block diagram of the C magnet regulation circuit. The
trace at the bottom indicates the short term stability at
4500 G for a period of two minutes. Long term stability
is approximately 5 ppm.
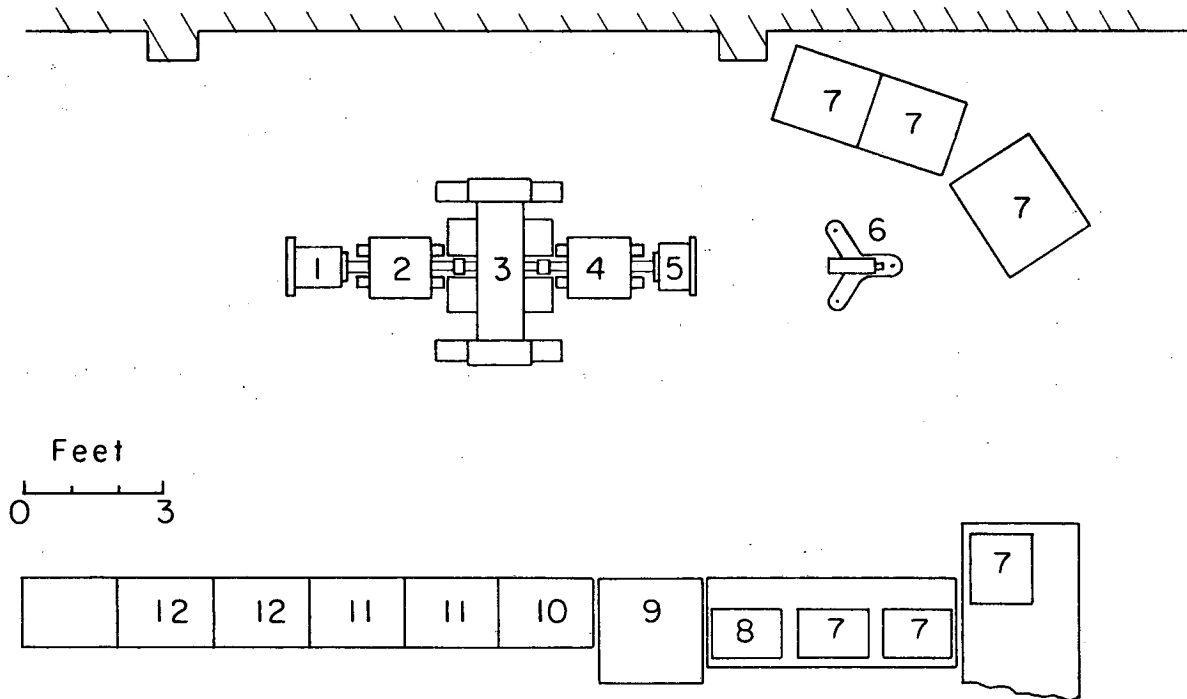
MUB-10146

MUB-10147

Fig. 8. Overall view of the experimental area showing: 1) oven
chamber, 2) A magnet, 3) C magnet, 4) magnet, 5) de-
tector chamber, 6) alignment telescope, 7) radio-frequency
electronics, 8) chart recorder, 9) C magnet supply, 10) oven
power supplies, 11) A and B magnet supplies and vacuum
gauge power supplies, 12) diffusion-pump supplies and ac
power distribution.

gold carrier, was dissolved in boiling aqua regia. The solution was cooled and mixed with ethyl acetate in a separatory funnel. The acid and platinum were drained off, leaving the gold in the ethyl acetate; this was dripped into boiling dilute hydrochloric acid to evaporate the ethyl acetate. Saturated hydroquinone solution was added to the HCl solution to precipitate the gold. After centrifugation and drying, the sample, now in the form of a small button of gold particles, was placed in the oven. The entire process was carried out in a junior cave or shielded Berkeley box which has 2 inches of lead shielding.

The oven design is illustrated in Fig. 9. The carbon snout and liner prevented the possibility of the gold from either alloying with the tantulum oven body or from wetting the tantulum and creeping out of the oven. An all-carbon oven could have been used, but carbon ovens are difficult to heat to high temperatures since they are such effective radiators of energy. The oven was heated by electron bombardment. Approximately 100 watts of power was sufficient to produce stable beams of the proper intensity. This corresponds to an oven temperature of about 1500° C.

Beams of potassium and cesium were obtained from a resistance-heated oven located in the buffer chamber between the oven chamber and the A magnet. This oven could be withdrawn to allow the radioactive beam to pass by. An oven charge consisted of calcium metal filings and either KCl or CsCl. At a few hundred degrees centigrade the calcium reduces the salt and an alkali beam is produced. We detected these alkali beams by using a hot iridium wire to ionize them and a picoammeter to indicate the ion current. Ion currents of 10^{-10} A were typical.

We detected radioactive beams by collecting atoms for 5 minutes on a sulfur surface placed at the detector position. Two buttons with such sulfur surfaces were used, one at the center to detect resonances, and one at the side to monitor the beam level by collecting the thrown-out beam. We measured the relative amounts of activity collected on these buttons by placing them in Geiger counters.

The counters are illustrated in Fig. 10. The guard tube and shielding guard against stray activity within the lab and against cosmic rays. The background counting rate for these counters is typically 2 counts per minute. The counters are some distance from the beam apparatus because of the high radiation field near the apparatus. The buttons are sent from the machine to the counting laboratory through a pneumatic tube. They are then cycled
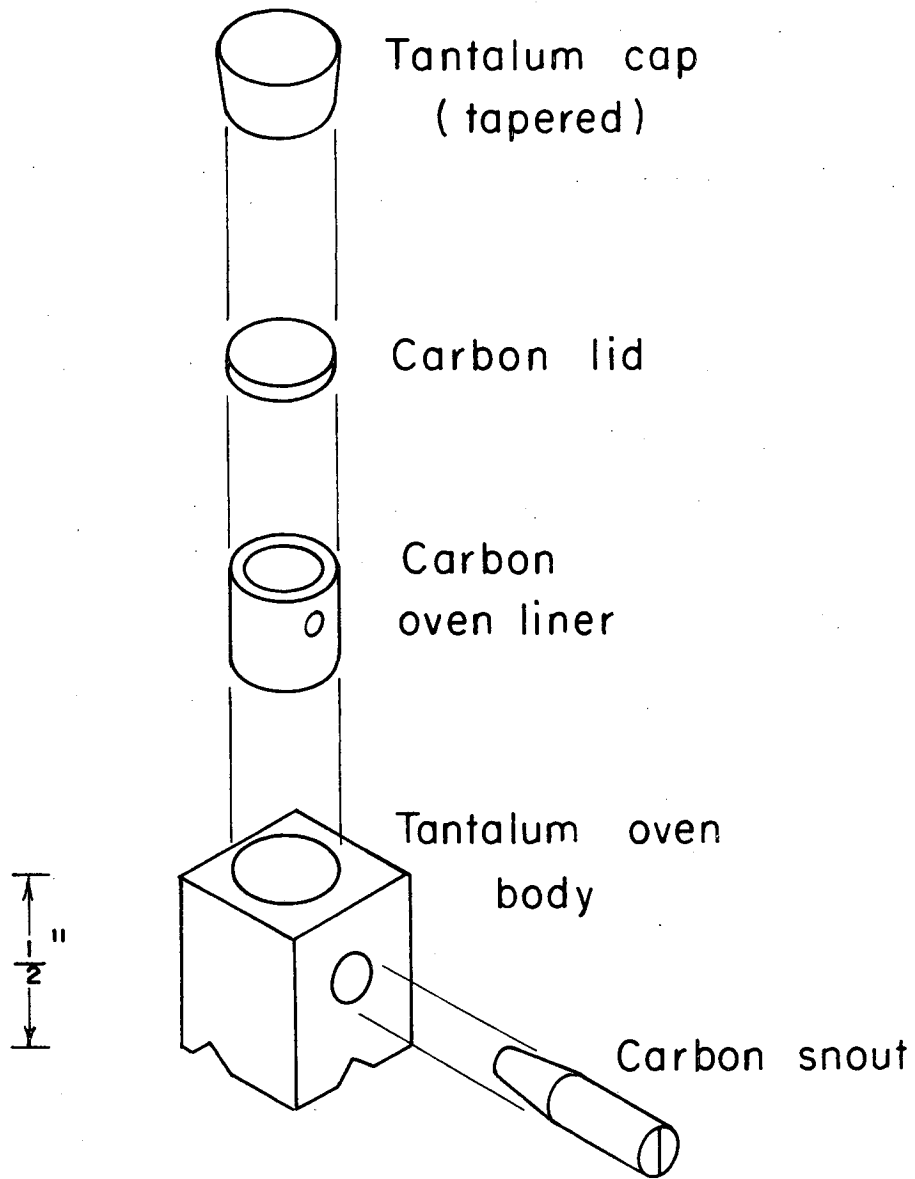
Slit width = 0.004"

MUB-10148

Fig. 9. Exploded view of oven from which gold beams were produced.
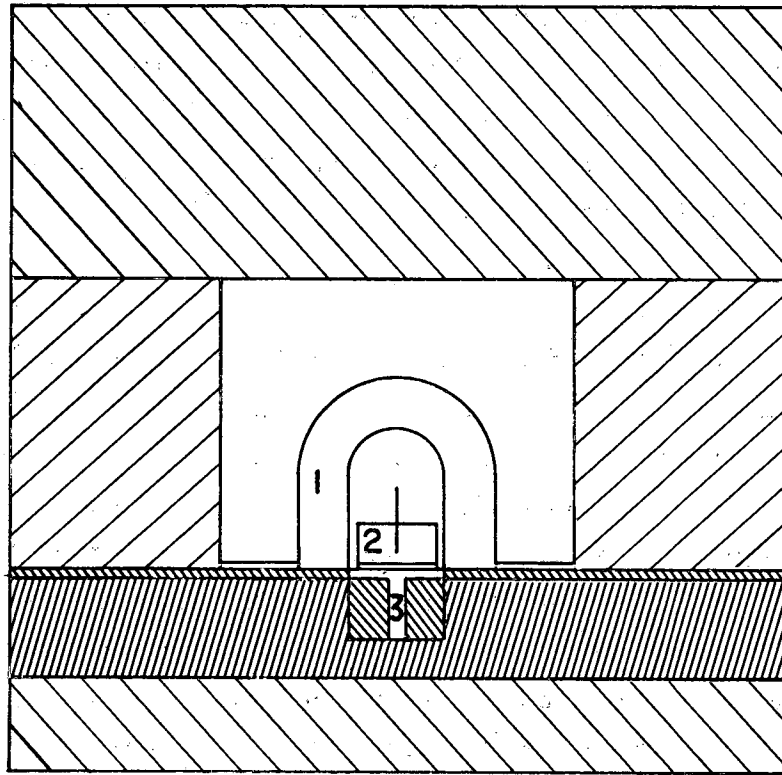
MUB-10149

Fig. 10. Cross section through a Geiger counter. (1) guard counter, (2) inner counter, (3) sample in drawer, lead, brass

through four counters, spending about 5 minutes in each. The four-counter averages, these averages normalized by the counting rate of the side button, and the uncertainty in the normalized averages are computed by a routine for the IBM 1620.

C. Radio-Frequency Equipment

The precision of measurement necessary in a hyperfine-structure-anomaly experiment requires the use of accurate, stable radio-frequency signals. In this experiment we used signals in the range 30 kHz to 22 GHz that were good to 1 part in 10^9. The use of microwaves was necessary to observe $\Delta F = 1$ transitions, since both Au^{198} and Au^{199} have large $\Delta\nu$'s. The design and construction of this microwave equipment was the major experimental difficulty.

In the lower frequency range (from 1 kHz to 30 MHz) we used the Schomandl oscillators (models ND5 and NDF2), simply amplifying the signal with an amplifier (Boonton No. 230A) before sending it to the hairpin or radio-frequency loop in the C region. This range could be extended to 300 MHz by using the Schomandl harmonic amplifier (model NB7). For the range 300 MHz to 1 GHz we used the Schomandl oscillator (model FD3) was used with a UHF amplifier (Electro-International AP-502R). This range could be extended to 3 GHz and beyond if necessary by using crystal multiplication and travelling-wave-tube amplifiers. From 3.3 GHz to 22 GHz, klystrons, phase-locked to the Schomandl FD3, were used as signal sources. The principle of phase-locking is illustrated in Fig. 11. The reference-oscillator frequency is set so that its Nth harmonic differs by 10 MHz from the desired klystron frequency. The mixer beats the klystron frequency against the reference frequency times N and sends the beat frequency of about 10 MHz to the Schomandl FDS-3 Syncriminator; here it is compared in phase with a standard 10-MHz signal and the phase difference is used to produce a correcting voltage that is applied to the reflector of the klystron. The dotted lines in Fig. 11 indicate frequency-measuring devices used only for klystron frequencies lower than 15 GHz.

Frequencies from 0 to 3.0 GHz could be counted directly with a Hewlett-Packard 5245L counter and the appropriate heterodyning plug-in unit. This range could be extended to 15 GHz by adding a Hewlett-Packard
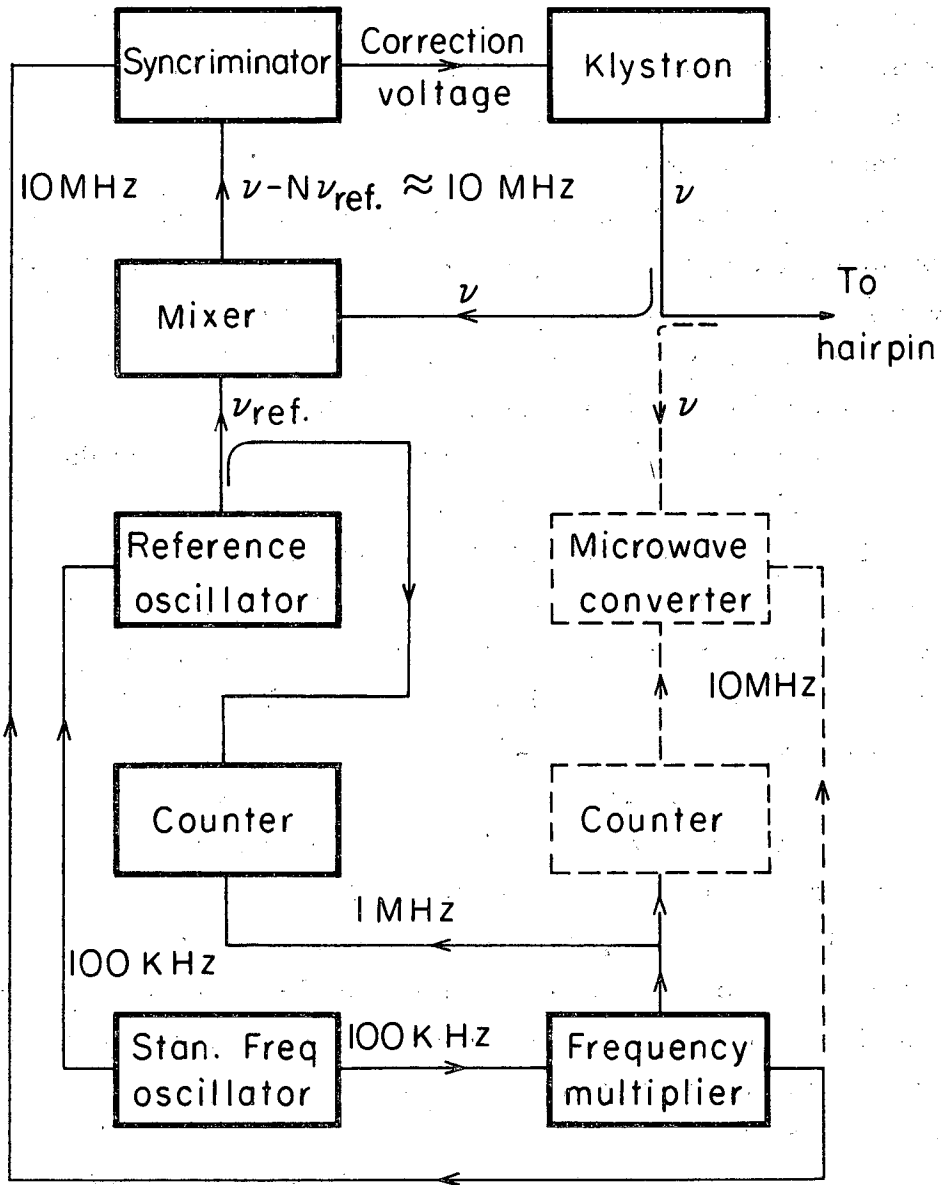
Fig. 11.   Block diagram of the klystron phase-locking circuit
and frequency-measuring circuit.

2590A microwave converter, which is essentially a transfer oscillator phase-locked to the frequency being measured. At higher frequencies, the reference frequency for the phase-locking circuit from the Schomandl FD3 would be measured with a counter, and a waveguide frequency meter would be used to check which harmonic was being generated and whether the klystron was locked 10 MHz above or below this harmonic. The beat frequency from the mixer was fed to a oscilloscope (Tektronix 561A) that was externally triggered by a 10-MHz standard frequency. This procedure made identification of so-called spurious locking points trivial, and there was never any ambiguity about how the klystron frequency was to be computed from the Schomandl frequency.

All counters, phase-locking devices, and reference oscillators had as frequency references 100-kHz, 1-MHz, or 10-MHz signals; these came from the combination of a 100-kHz oscillator (J. Knight FS 1100T) which has a specified stability of $\pm 5 \times 10^{-10}$ per 24 hours, and a standard-frequency multiplier (General Radio 1112-A). The 100-kHz oscillator was continuously monitored against station WWBV 60-kc standard-frequency broadcasts by a phase-comparison receiver (Gertsch PCR-1 VLF) and its crystal was reset whenever the offset was $\approx 1 \times 10^{-8}$. The observed stability of the 100-kHz oscillator is 5×10^{-11} per 24 hours.

For this experiment, the beam apparatus was fitted with a new C can or vacuum chamber between the pole tips of the C magnet. The new chamber allowed greater freedom in the placement of the proton sample of the NMR field-locking device. A large opening in the top of the can allowed hairpins mounted on a plate to be moved back and forth without loss of vacuum. Shimming coils to correct for field inhomogeneities were included in the sides of the chamber but were not used in this experiment. A final new feature was the valves that were placed at the ends of the can. These allowed hairpins to be quickly changed without disturbing the vacuum in the rest of the apparatus.

For work at low magnetic fields on the standard or $\Delta F = 0$, $\Delta M_F = 0$ transition, we used the hairpin on the left in Fig. 12. It consists of a standard 50-ohm coaxial line tapering gradually into a short. In the earlier phases of this experiment, this hairpin was also used for high-field work. However, subsequent work on the alkali g factors (see Appendix B) revealed that this introduced systematic errors into the results. Figure 13 shows two graphs, one of the quantity $R = [g_J(Cs^{133})/g_J(K^{39})] - 1$ measured at various magnetic fields with this shorted hairpin, the other showing the same quantity R

50 – ohm coaxial line

Beam

Short

Beam

50-ohm termination
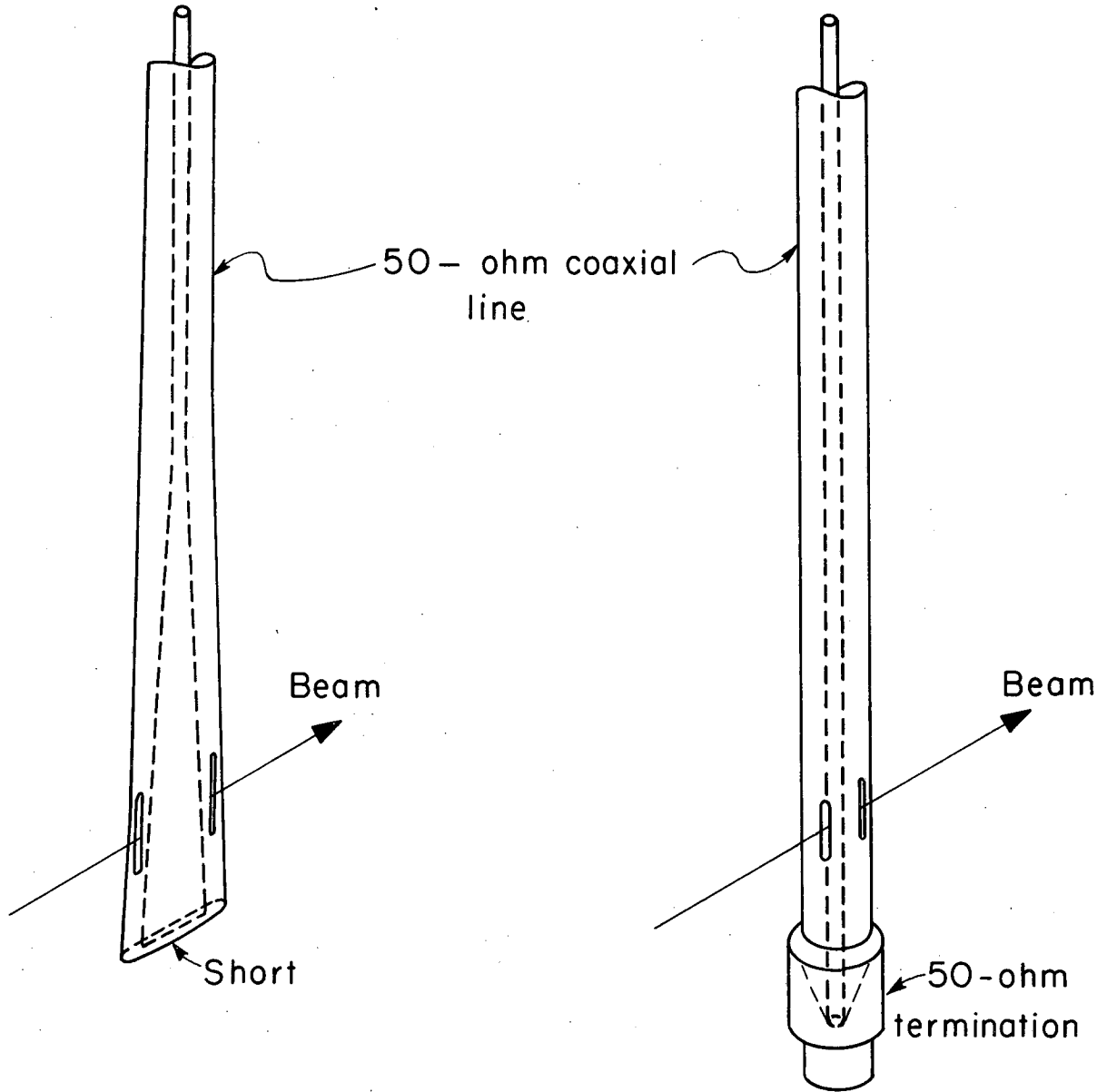
MUB4740

Fig. 12. Sketch of the shorted and terminated types of hairpins.
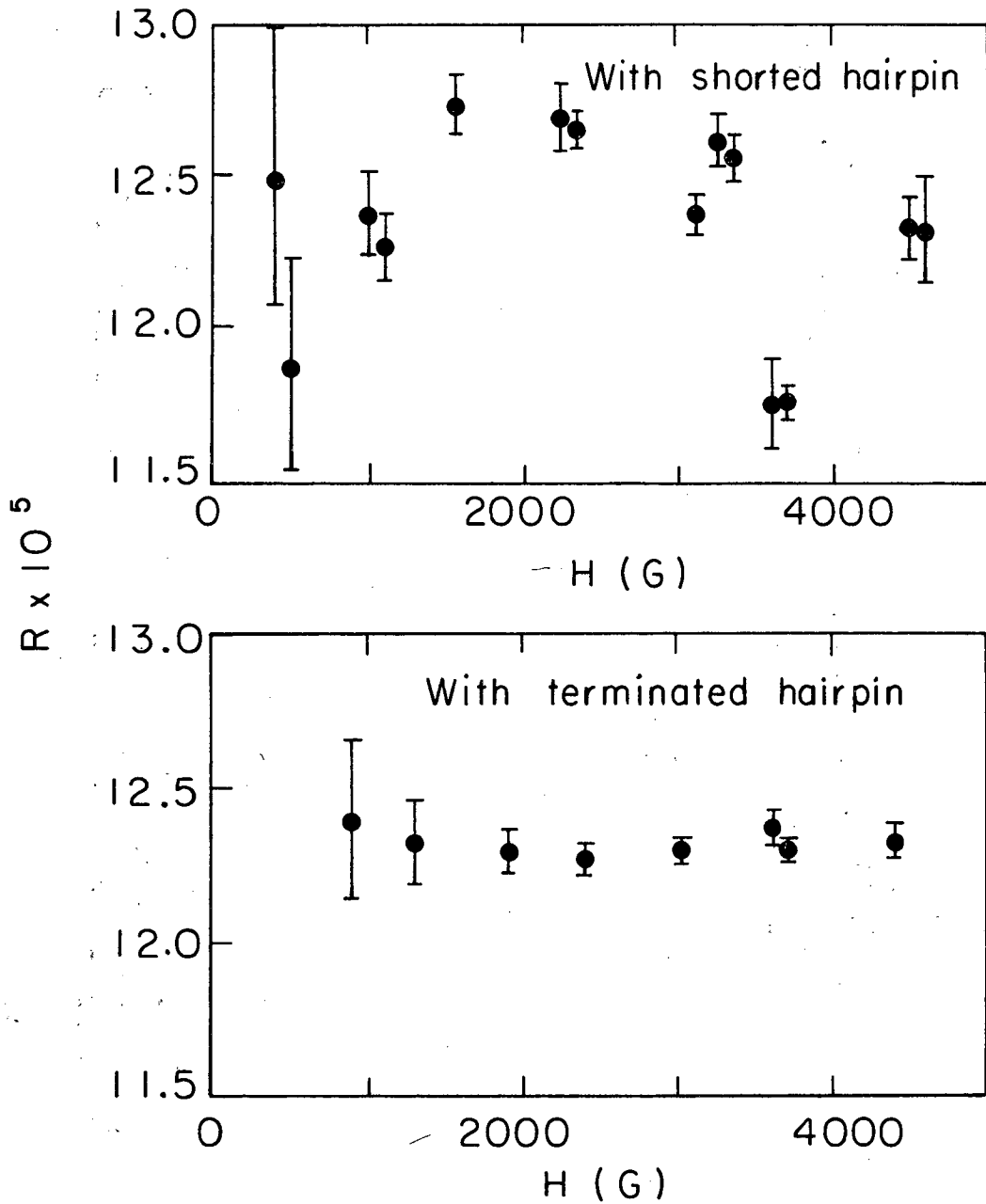
Fig. 13. Comparison of the performance of the shorted and terminated types of hairpins at high magnetic field and frequencies.

obtained as a function of magnetic field with the hairpin illustrated on the right in Fig. 12. The quantity R is independent of the magnetic field. The scatter of the results for the shorted hairpin probably results from peculiar standing-wave patterns set up in the tapered section at high frequencies. The power for the potassium frequency was maximum at a different location than the power for the cesium frequency. Since the C field was not perfectly homogeneous, the measurements on the two isotopes were not done in the same field, or equivalently, the calibration of the magnetic field was inaccurate. The hairpin designed to eliminate this effect, illustrated on the right in Fig. 12, consisted of a standard 50-ohm coaxial line terminated in a matched load. As is seen in Fig. 13, this modified hairpin yielded much more consistent results. This improved high-frequency hairpin was also used for making the initial observations of $\Delta F = 1$ transitions in Au^{199}.

The initial observations of $\Delta F = 1$ transitions in Au^{198} were made with a waveguide hairpin since coaxial cables are too "lossy" above 10 GHz. Such a hairpin is shown in Fig. 14. It was moved into position in the center of the C-can so that one could observe Au transitions, and the coaxial hairpin was moved to the center to observe calibration resonances.

For precise observation of the $\Delta F = 1$ transitions that determine $\Delta \nu$ and g_I we used cavity hairpins, shown in Fig. 15. In designing the cavity hairpins, we considered the following two considerations: The space available in the C can limits the cavity diameter to 7/8 inch and its length to 5 inches. The mode chosen must provide the correct magnetic-field configuration for the transition to be observed. For $\Delta M_F = 0$ transitions H_{rf} must be parallel to H, and for $\Delta M_F = 1$ transitions H_{rf} must be perpendicular to H. For the first runs with cavity hairpins we used cavities 2 inches long. Later these runs were repeated with cavities 5 inches long so that we could obtain narrower lines. The line width of a field-independent transition varies as $\delta \nu = v / L$, where v is the mean velocity of the beam ($v \approx 4 \times 10^4$ cm/sec for gold) and L is the length of the transition region. We observed lines that approached this natural line width of 3 kHz for a 5-inch cavity.

When the frequency and length of the cavity are known, the diameter can be calculated from the formula $(fD)^2 = (cf/\pi)^2 + (cn/2)^2(D/L)^2$, where f is the frequency in MHz, D is the diameter in inches, L is the length in inches, c is the velocity of light in inches/sec, n is the third index specifying the mode, and r is the Bessel root appropriate to the model chosen.[36]
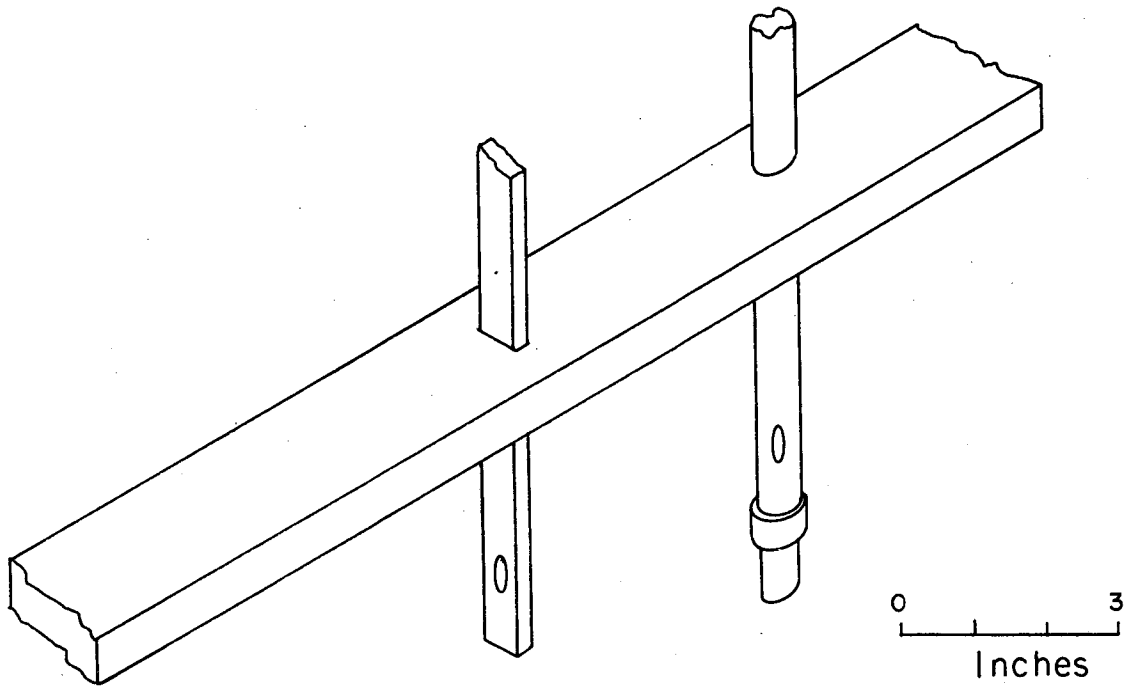
Fig. 14. Sketch of the K-band waveguide hairpin.

MUB-10152
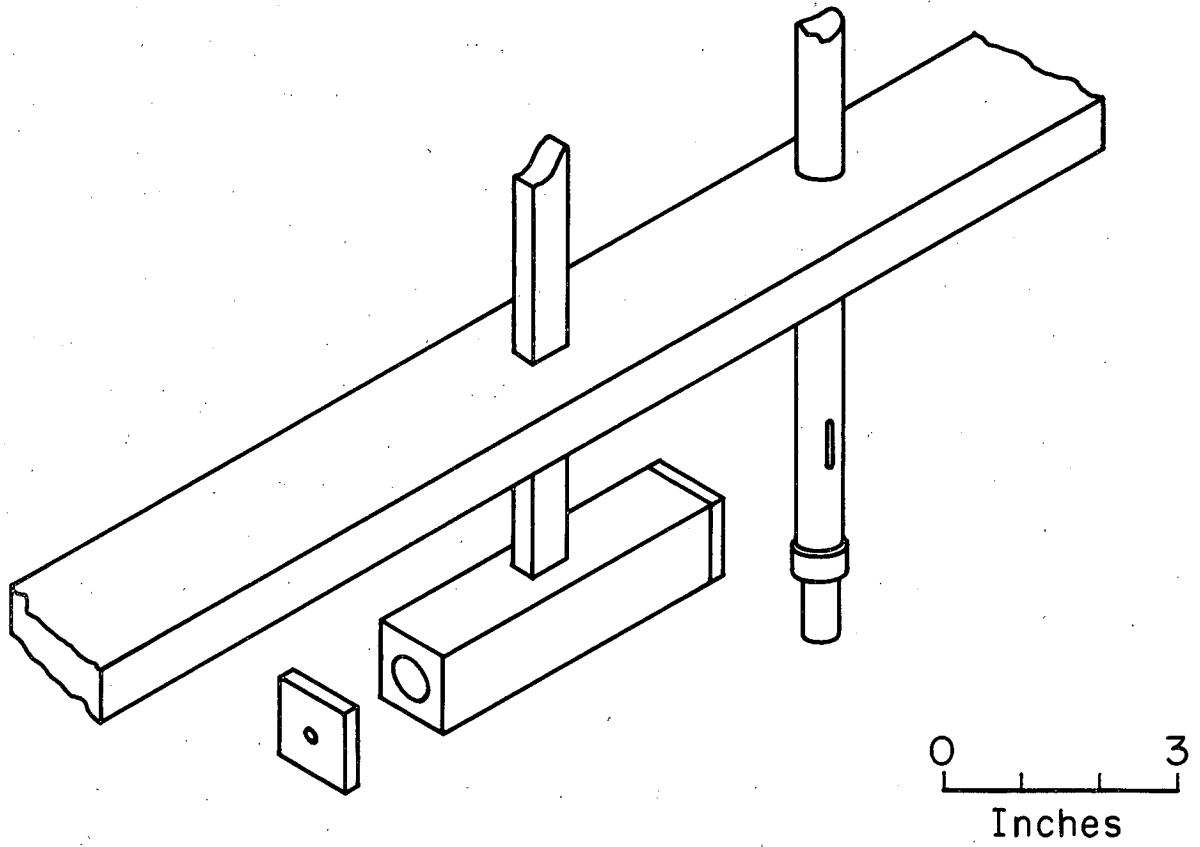
Fig. 15. Sketch of the K-band cavity hairpin.

MUB-10038

The diameter was calculated for a number of likely modes and those cavities with diameters sufficiently small to fit the machine were then candidates for hairpins. For $\Delta M_F = 1$ transitions the TE_{011} mode was chosen since H_{rf} lies along the beam axis; this mode was used for all Au^{198} work. The TM_{111} mode which is degenerate with the TE_{011} mode was suppressed to a certain extent by insulating the end caps of the cavity from the rest of the cavity with 0.001-inch Mylar. The TM_{111} requires the flow of surface current across this crack but the TE_{011} does not. For the Au^{199} frequencies, the only mode providing dimensions small enough was TM_{010}. This mode, which has H_{rf} in circles centered about the beam axis, was therefore suitable for both $\Delta M_F = 0$ and $\Delta M_F = 1$ transitions. Both modes, TE_{011} and TM_{010}, had the Poynting vector in the radial direction and hence Doppler shifts could be neglected. Figure 16 shows the field configurations for the two modes.

The cavities were machined as accurately as was practical and then tuned to a final frequency either by honing if the frequency was higher than desired, or by silver plating if it was lower than desired. Values for Q of about 5000 were typical although high Q values are not necessary. The power required to observe transitions varied from a few μW to a few hundred μW.

D. Run Procedure and Planning

The first step of every run was to set the magnetic field and start the diffusion pumps. The next day the magnetic field was locked with the NMR field-locking device, the necessary radio-frequency equipment was assembled, and the stability of the magnetic field was monitored by observing the standard transition in an alkali beam. The third day the sample was received and any necessary chemistry performed. The oven was loaded, placed in the apparatus, and aligned. I preferred to run at night to avoid interference of any kind. Buttons were exposed for 5-minute periods, each at a different frequency. After exposure they were immediately sent up the pneumatic tube to the counting room where the relative counting rates were plotted versus frequency. When a resonance was found, it was swept once, and then at the peak frequency, the power was varied to determine the optimum power. The resonance was then swept at optimum power as often as desired. The magnetic field was calibrated before and after each sweep. The samples lasted for as long as 2 weeks.
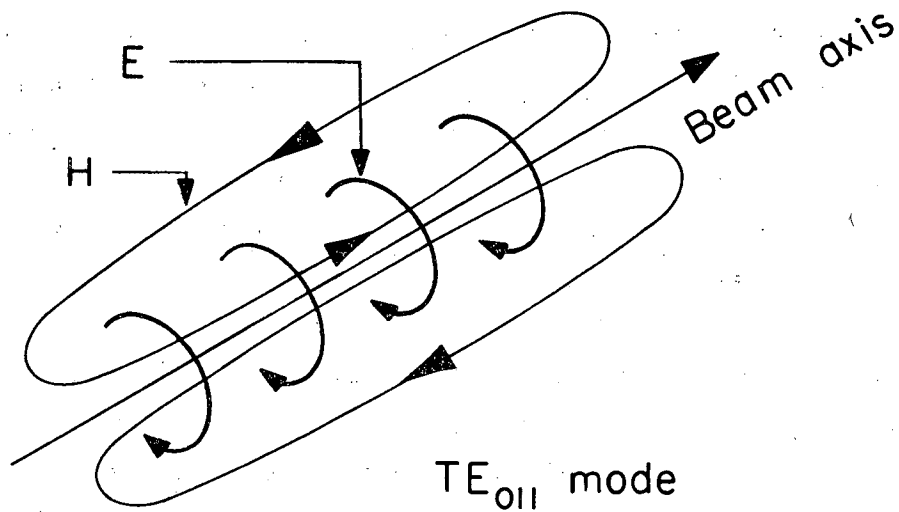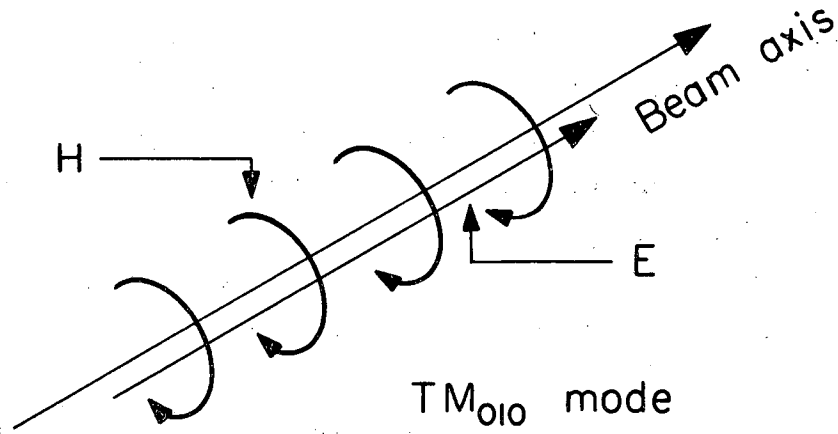
Fig. 16. Sketch of the field configurations of the two types of cavity modes used in the cavity hairpins.

For $J = 1/2$, the selection of the proper transitions to observe in order to determine the parameters $\Delta\nu$, g_J, and g_I most accurately is easy. The first restriction is that imposed by the use of a flop-in machine, that is, $\Delta M_J = 1$. In addition there are the low-field selection rules $\Delta F = 0, 1$ and $\Delta M_F = 0, \pm 1$; and the high-field selection rules $\Delta M_J = 0, \pm 1$ and $\Delta M_I = 0, \pm 1$.

To determine g_J, we observed the standard transition at high magnetic field. The frequency of transition can be obtained from (24): $h\nu = -aI - \mu_0 H g_J$. Since $(\partial\nu/\partial g_J) = -\mu_0 H/h \approx 10^4$, this method provides a sensitive measure of g_J.

To determine $\Delta\nu$ we chose to observe those $\Delta F = 1$ transitions at zero magnetic field whose frequency of transition was field independent at that point, i.e., $\partial\nu/\partial H \approx 0$. For Au^{198} these are the transitions $(5/2, \pm 1/2) - (3/2, \mp 1/2)$, and for Au^{199} the transition $(2, 0) - (1, 0)$. Because $\partial\nu/\partial H \approx 0$, it is possible to obtain a narrow line since field inhomogeneity was the major cause of line width.

To determine g_I, we observed the transitions $(5/2, -3/2) - (3/2, -1/2)$ and $(5/2, -1/2) - (3/2, -3/2)$ in Au^{198}, and the transitions $(2, 0) - (1, -1)$ and $(2, -1) - (1, 0)$ in Au^{199}. These transitions form doublets and the splitting of each doublet is equal to $\Delta W = 2g_I\mu_0 H$. For all such doublets (there are many others) with $M_F + M_F' < 0$ there exists a value of the magnetic field for which the doublet frequencies are field independent.[37] If transitions are observed at this magnetic field it is possible to obtain narrow lines and an accurate determination of g_I. This value of the field for Au^{198} was 3214.5 G and for Au^{199} was 1047.6 G.

HYPERFINE F-9, a program for the IBM 7094, provided tables of frequency versus magnetic field. The input consisted of the quantum numbers of the transition and the best available values of a, g_I, and g_J. A program write-up is available from the Atomic Beam Group at the Lawrence Radiation Laboratory.

TEE PEE, a program for the IBM 7094, was useful in planning the gold runs. The program was written by Prof. William A. Nierenberg and a complete write-up of it too is available from the Atomic Beam Group of the Lawrence Radiation Laboratory. This program calculates the quantity $|\langle IJFM_F | \vec{J} | IJF'M_F' \rangle|^2$ as a function of magnetic field. More specifically, it calculates the square of the matrix element of J_z if $M_F - M_F' = 0$, and of

J_x if $M_F - M'_F = \pm 1$. If the oscillating magnetic field in the hairpin is linear and given by $H_{rf} = H_0 \sin \omega t$, and if H_{rf} is along z if $\Delta M_F = 0$ and along x if $\Delta M_F = \pm 1$, and if contributions from g_I are ignored as being too small, then the probability that an atom will make the transition between the states $|IJFM_F\rangle$ and $|IJF'M'_F\rangle$ on passing through the hairpin is given by

$$\frac{1}{4} \left[\frac{\mu_0 \, g_J \, H_0 \, t}{\hbar} \right]^2 \; | \langle IJFM_F | \vec{J} | IJF'M'_F \rangle |^2 \,,$$

where H_0 is the strength of the radio-frequency field in Gauss and t is the time that it takes an atom to pass through the hairpin.

The program provides both a check on transitions accidently forbidden at a particular field and an indication as to how much rf power would be necessary to observe a transition. Frequently in setting up a run I would observe a transition in some alkali and vary the rf power until the resonance was maximized but not overpowered. Comparison of the transition probability for this transition with that for the desired transition in gold would then tell me what rf power was needed for the gold-resonance search. After the gold resonance had been found, I usually varied the rf power at the peak frequency to check whether or not this power was really optimum. This final check was very important in the final runs since cavity hairpins require very little rf power and overpowering a resonance broadens it considerably.

Figure 17 gives the results of the program for the transitions observed in Au^{198} and Au^{199}. Notice that the doublet-transition probabilities are equal precisely at the field-independent point. This fact seems to be true for many isotopes, including all the alkalis.[38]
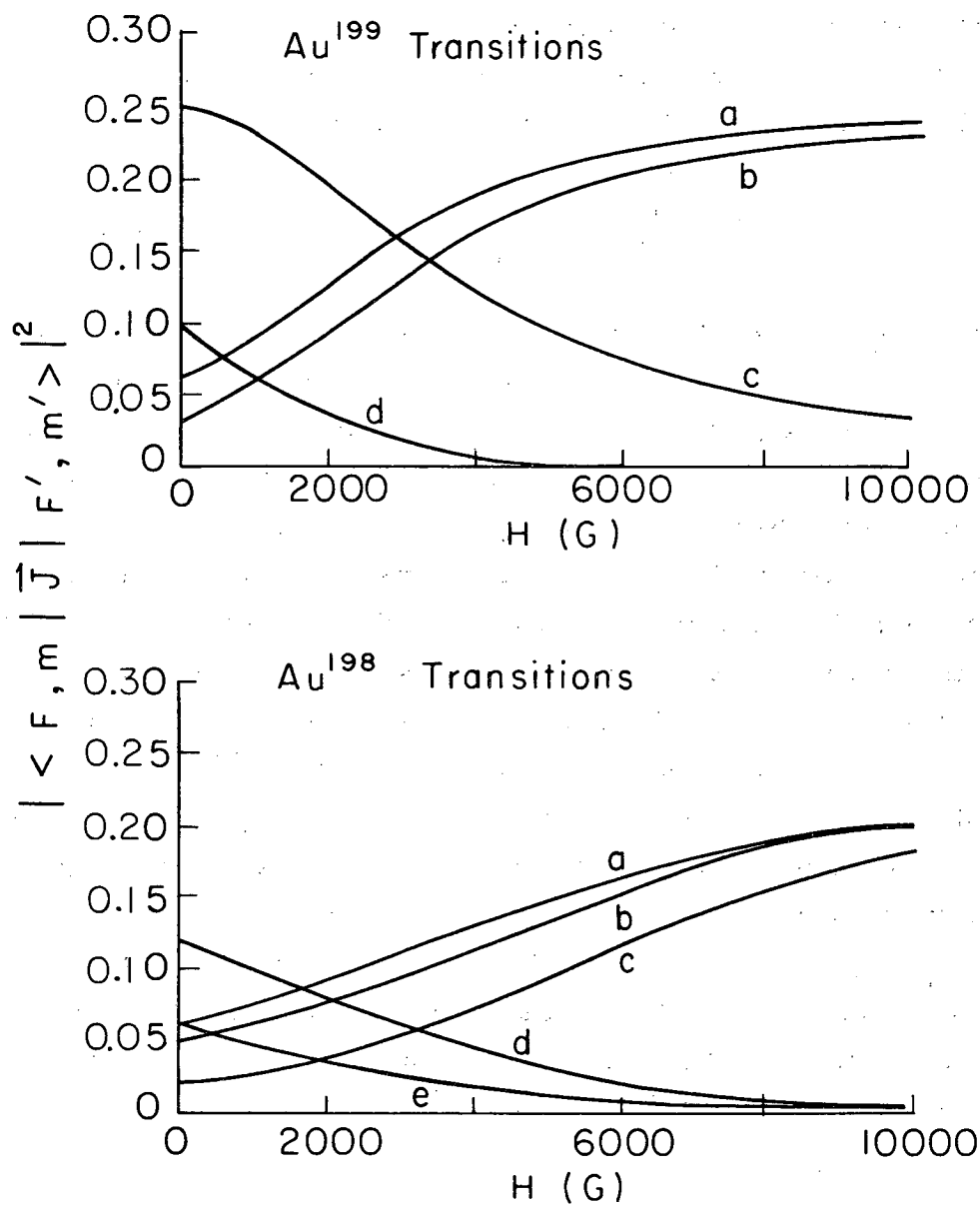
Fig. 17. Transition-probability matrix elements plotted versus
magnetic field. For Au^{199} the transitions are (a) $(2, -1)$
$-(2, -2)$, (b) $(2, 0)-(1, -1)$, (c) $(2, 0)-(1, 0)$, (d) $(2, -1)-(1, 0)$;
for Au^{198} the transitions are (a) $(5/2, 1/2)-(3/2, -1/2)$,
(b) $(5/2, -3/2) - (5/2, -5/2)$, (c) $(5/2, -1/2) - (3/2, -3/2)$,
(d) $(5/2, -3/2) - (3/2, -1/2)$, (e) $(5/2, -1/2) - (3/2, 1/2)$.

MUB-10154

IV.   DATA AND RESULTS

A.   Description of Data

The experimental data obtained during this research are presented in Tables V and VI.   The residuals listed there are the observed frequencies minus the frequencies calculated by the least-squares fitting routine, with the final values at $\Delta\nu$, g_I, and g_J resulting from the fit.   The weight factor, which indicates the relative weight given a datum in the fitting routine, is equal to $[\text{(error in } \nu_{obs})^2 + (\frac{\partial\nu}{\partial H})^2 \text{(error in H)}^2]^{-1}$.   The observed frequencies listed in these tables have been corrected for the difference between the J.Knight 100-kHz oscillator signal used as reference in this experiment and the standard signal broadcast by station WWVB, National Bureau of Standard, Boulder, Colorado.   The WWVB signal is based on Atomic Time, A1, which defines the second by taking the (4,0) - (3, 0) hyperfine transition of Cs^{133} to be exactly 9192.631770 MHz.   All my measurements are based on this definition of the second.   We have kept a record of $\Delta\nu/\nu$, where $\Delta\nu = \nu_{JKnight} - \nu_{WWVB}$, in our laboratory since 1962.   The value of $\Delta\nu/\nu$ on the days of the runs for this research is given in Table VII. If $\Delta\nu/\nu > 0$, our standard 100 kHz was too fast, implying that the gate on our counters was not open long enough, and, hence, our recorded frequencies were too low. The result is that the observed frequencies of transition for Au^{198} given in Table V have had 0.0002 MHz added to them for resonances 47A1 through 50C2; the observed frequencies of transition for Au^{199} given in Table VI have had 0.0001 MHz added to them for resonances 46A1 through 49C4. None of the calibration frequencies required correction.

Run 4 was a series of measurements made to determine the sign of μ_I and to get a better value of $\Delta\nu$ for Au^{198}.   Run 8 was made to determine g_J.   Resonances 8A through 8G were observed at 4000 and 8000 G but using a hairpin that we later found gave systematic errors; therefore these data were discarded and Run 32 made to replace the discarded data.   Resonances 8H and 8I at 2500 G were considered reliable and included in the least-squares analysis.

Resonance 32A was the first $\Delta F = 1$ transition observed in the experiment.   After identifying it we observed the field-independent $\Delta F = 1$ transition labelled Resonance 32B.   Resonances 32C, 32D, 32F were observed to determine g_J.   Run 32E was an attempt to observe one member of the doublet

Table V. Experimental data for Au[198]

Run	Calib. isotope	$\nu_{calib.}$ (MHz)	H(G)	Gold transition $(F_1, m_1) - (F_2, m_2)$	ν_{Au} (MHz)	Residual	Weight factor
4A	K^{39}	44.2149(55)	50.0063(50)	(5/2, -3/2)-(5/2, -5/2)	28.1840(50)	+ 0.0039	30160
4B	K^{39}	200.5925(75)	150.0168(37)	(5/2, -3/2)-(5/2, -5/2)	85.4300(35)	- 0.0030	58990
4C	K^{39}	684.5815(55)	350.0238(21)	(5/2, -3/2)-(5/2, -5/2)	203.6012(35)	- 0.0031	72290
4D	K^{39}	2750.4857(70)	1100.0625(25)	(5/2, -3/2)-(5/2, -5/2)	694.0465(45)	- 0.0022	42730
8H	Cs^{133}	1947.397(13)	2500.1780(88)	(5/2, -3/2)-(5/2, -5/2)	1846.123(10)	- 0.0064	5915
8I	Cs^{133}	1947.391(13)	2500.1741(88)	(5/2, -3/2)-(5/2, -5/2)	1846.115(8)	- 0.0106	7516
32A	Cs^{133}	0.5441(70)	1.555(20)	(5/2, 1/2)-(3/2, 1/2)	21451.585(13)	- 0.0038	3391
32B	Cs^{133}	0.6030(70)	1.723(20)	(5/2, 1/2)-(3/2, -1/2)	21450.720(26)	+ 0.0033	1479
32C1	Cs^{133}	6119.922(18)	4599.9002(75)	(5/2, -3/2)-(5/2, -5/2)	4303.085(14)	- 0.0032	3244
32C2	Cs^{133}	6119.913(18)	4599.8965(75)	(5/2, -3/2)-(5/2, -5/2)	4303.087(12)	+ 0.0039	3902
32D1	Cs^{133}	6119.906(18)	4599.8934(75)	(5/2, -3/2)-(5/2, -5/2)	4303.083(12)	+ 0.0043	3902
32D2	Cs^{133}	6119.901(18)	4599.8912(75)	(5/2, -3/2)-(5/2, -5/2)	4303.082(12)	+ 0.0063	3902
32F1	Cs^{133}	11998.303(24)	6900.0110(90)	(5/2, -3/2)-(5/2, -5/2)	8118.300(24)	+ 0.0082	1151
32F2	Cs^{133}	11998.328(24)	6900.0204(90)	(5/2, -3/2)-(5/2, -5/2)	8118.310(24)	+ 0.0004	1151
32F3	Cs^{133}	11998.323(24)	6900.0185(90)	(5/2, -3/2)-(5/2, -5/2)	8118.305(24)	- 0.0011	1151
37A1	Cs^{133}	3126.650(10)	3214.4947(54)	(5/2, -1/2)-(3/2, -3/2)	19564.390(30)	+ 0.0018	1111
37A2	Cs^{133}	3126.656(10)	3214.4979(54)	(5/2, -1/2)-(3/2, -3/2)	19564.390(30)	+ 0.0018	1111
37A3	Cs^{133}	3126.657(10)	3214.4982(54)	(5/2, -1/2)-(3/2, -3/2)	19564.390(30)	+ 0.0018	1111
37B1	Cs^{133}	3126.632(10)	3214.4851(54)	(5/2, -3/2)-(3/2, -1/2)	19565.820(30)	+ 0.0004	1111
37B2	Cs^{133}	3126.633(10)	3214.4856(54)	(5/2, -3/2)-(3/2, -1/2)	19565.820(30)	+ 0.0004	1111
37B3	Cs^{133}	3126.636(10)	3214.4871(54)	(5/2, -3/2)-(3/2, -1/2)	19565.820(30)	+ 0.0004	1111
37C1	Cs^{133}	3126.655(10)	3214.4974(54)	(5/2, -1/2)-(3/2, -3/2)	19564.390(30)	+ 0.0018	1111
37C2	Cs^{133}	3126.655(10)	3214.4974(54)	(5/2, -1/2)-(3/2, -3/2)	19564.390(30)	+ 0.0018	1111
37C3	Cs^{133}	3126.655(10)	3214.4974(54)	(5/2, -1/2)-(3/2, -3/2)	19564.390(30)	+ 0.0018	1111
37C4	Cs^{133}	3126.639(10)	3214.4889(54)	(5/2, -3/2)-(3/2, -1/2)	19565.820(30)	+ 0.0004	1111
37C5	Cs^{133}	3126.639(10)	3214.4889(54)	(5/2, -3/2)-(3/2, -1/2)	19565.820(30)	+ 0.0004	1111
37C6	Cs^{133}	3126.639(10)	3214.4889(54)	(5/2, -3/2)-(3/2, -1/2)	19565.820(30)	+ 0.0004	1111
47A1	Cs^{133}	3126.684(17)	3214.5127(91)	(5/2, -3/2)-(3/2, -1/2)	19565.8202(27)	+ 0.0004	137200
47A2	Cs^{133}	3126.712(17)	3214.5278(91)	(5/2, -3/2)-(3/2, -1/2)	19565.8202(25)	+ 0.0004	160000
47B1	Cs^{133}	3126.659(35)	3214.500(19)	(5/2, -1/2)-(3/2, -3/2)	19564.3877(25)	- 0.0007	160000
47B2	Cs^{133}	3126.662(35)	3214.501(19)	(5/2, -1/2)-(3/2, -3/2)	19564.3877(25)	- 0.0007	189000
50A1	Cs^{133}	3126.7240(60)	3214.5345(32)	(5/2, -3/2)-(3/2, -1/2)	19565.8198(7)	- 0.0000	2041000
50A2	Cs^{133}	3126.7240(60)	3214.5345(32)	(5/2, -3/2)-(3/2, -1/2)	19565.8198(8)	- 0.0000	1563000
50A3	Cs^{133}	3126.7250(60)	3214.5350(32)	(5/2, -1/2)-(3/2, -3/2)	19565.3885(7)	+ 0.0002	2041000
50A4	Cs^{133}	3126.7250(60)	3214.5350(32)	(5/2, -1/2)-(3/2, -3/2)	19564.3885(7)	+ 0.0002	2041000
50B1	Cs^{133}	3126.7290(60)	3214.5372(32)	(5/2, -1/2)-(3/2, -3/2)	19564.3885(7)	+ 0.0002	2041000
50B2	Cs^{133}	3126.7290(60)	3214.5372(32)	(5/2, -3/2)-(3/2, -1/2)	19565.8198(8)	- 0.0000	1563000
50B3	Cs^{133}	3126.7200(60)	3214.5323(32)	(5/2, -3/2)-(3/2, -1/2)	19565.8196(8)	- 0.0002	1563000
50B4	Cs^{133}	3126.7220(60)	3214.5324(32)	(5/2, -1/2)-(3/2, -3/2)	19564.3879(7)	- 0.0004	2041000
50B5	Cs^{133}	0.310(10)	0.886(29)	(5/2, -1/2)-(3/2, 1/2)	21450.7173(9)	+ 0.0002	1234000
50B5	Cs^{133}	0.310(10)	0.886(29)	(5/2, 1/2)-(3/2, -1/2)	21450.7173(9)	+ 0.0006	1234000
50B6	Cs^{133}	0.310(10)	0.886(29)	(5/2, -1/2)-(3/2, 1/2)	21450.7169(9)	- 0.0002	1234000
50B6	Cs^{133}	0.310(10)	0.886(29)	(5/2, 1/2)-(3/2, -1/2)	21450.7169(9)	+ 0.0002	1234000
50C1	Cs^{133}	0.315(10)	0.900(29)	(5/2, -1/2)-(3/2, 1/2)	21450.7164(12)	- 0.0007	694400
50C1	Cs^{133}	0.315(10)	0.900(29)	(5/2, 1/2)-(3/2, -1/2)	21450.7164(12)	- 0.0003	694400
50C2	Cs^{133}	0.286(10)	0.817(29)	(5/2, -1/2)-(3/2, 1/2)	21450.7168(10)	- 0.0002	999900
50C2	Cs^{133}	0.286(10)	0.817(29)	(5/2, 1/2)-(3/2, -1/2)	21450.7168(10)	+ 0.0001	999900

Table VI. Experimental data for Au^{199}

Run	Calib. isotope	$\nu_{calib.}$ (MHz)	H(G)	Gold transition $(F_1, m_1)-(F_2, m_2)$	ν_{Au} (MHz)	Residual	Weight factor
6A	K^{39}	44.2092(75)	50.0010(68)	(2, -1)-(2, -2)	35.3835(75)	+ 0.0017	12440
6B	K^{39}	200.5910(75)	150.0160(37)	(2, -1)-(2, -2)	108.2210(60)	- 0.0029	22860
6C	K^{39}	503.0970(85)	280.0329(33)	(2, -1)-(2, -2)	207.1910(40)	- 0.0035	43790
6D	K^{39}	2750.4095(85)	1100.0352(30)	(2, -1)-(2, -2)	956.658(10)	- 0.0044	90570
10A	Cs^{133}	500.4140(75)	1049.899(12)	(2, 0)-(1, -1)	10589.038(13)	+ 0.0015	6400
10B	Cs^{133}	500.4140(75)	1049.899(12)	(2, 0)-(1, -1)	10589.0395(40)	+ 0.0035	62500
10C	Cs^{133}	500.4140(75)	1049.899(12)	(2, 1)-(1, 0)	10589.3190(90)	- 0.0023	12350
10D	Cs^{133}	500.4140(75)	1049.899(12)	(2, -1)-(1, 0)	10589.3215(50)	+ 0.0002	40000
13A	K^{39}	0.7051(70)	1.0020(99)	(2, -1)-(1, 0)	10962.0255(90)	+ 0.0049	7746
13B	K^{39}	0.7042(65)	1.0008(92)	(2, -1)-(1, 0)	10962.0240(60)	+ 0.0025	12910
13C	K^{39}	0.7035(70)	0.9998(99)	(2, 0)-(1, 0)	10962.7215(90)	- 0.0014	12350
13D	K^{39}	0.7026(70)	0.9985(99)	(2, 0)-(1, 0)	10962.723(10)	- 0.0004	10000
13G	Cs^{133}	498.9456(80)	1047.594(13)	(2, -1)-(1, 0)	10589.3185(40)	- 0.0007	62500
13H	Cs^{133}	498.9480(80)	1047.598(13)	(2, -1)-(1, 0)	10589.3187(55)	- 0.0005	33060
13I	Cs^{133}	498.9500(80)	1047.601(13)	(2, 0)-(1, -1)	10589.0360(70)	+ 0.0015	20410
13J	Cs^{133}	498.9528(80)	1047.605(13)	(2, 0)-(1, -1)	10589.0368(30)	+ 0.0023	111100
26A	Cs^{133}	5546.432(10)	2100.2126(36)	(2, -1)-(2, -2)	2214.1790(80)	- 0.0000	10950
26A	Cs^{133}	5546.343(10)	2100.1809(36)	(2, -1)-(2, -2)	2214.1350(60)	+ 0.0025	15800
26B	Cs^{133}	8627.052(12)	3200.3745(43)	(2, -1)-(2, -2)	4063.048(10)	+ 0.0057	6050
26D	Cs^{133}	8345.833(15)	5500.3926(59)	(2, -1)-(2, -2)	9102.635(15)	- 0.0091	2419
26E	Cs^{133}	11468.376(25)	6700.4070(94)	(2, -1)-(2, -2)	12084.595(24)	- 0.0013	868
46A1	Cs^{133}	498.9408(70)	1047.586(11)	(2, 0)-(1, -1)	10589.0345(10)	- 0.0001	1000000
46A2	Cs^{133}	498.9324(70)	1047.573(11)	(2, 0)-(1, -1)	10589.0357(12)	+ 0.0011	694000
46B1	Cs^{133}	498.9296(70)	1047.569(11)	(2, -1)-(1, 0)	10589.3195(13)	+ 0.0002	591700
46B2	Cs^{133}	498.9503(70)	1047.601(11)	(2, -1)-(1, 0)	10589.3195(12)	+ 0.0002	694400
49B1	Cs^{133}	498.9430(60)	1047.5898(94)	(2, 0)-(1, -1)	10589.0345(5)	- 0.0001	4000000
49B2	Cs^{133}	498.9440(60)	1047.5914(94)	(2, 0)-(1, -1)	10589.0345(8)	- 0.0001	1563000
49B3	Cs^{133}	498.9550(60)	1047.6086(94)	(2, 0)-(1, -1)	10589.0345(6)	- 0.0001	2778000
49B4	Cs^{133}	498.9610(60)	1047.6181(94)	(2, 0)-(1, -1)	10589.0345(4)	- 0.0001	6250000
49B5	Cs^{133}	498.9440(60)	1047.5913(94)	(2, -1)-(1, 0)	10589.3192(5)	- 0.0001	4000000
49B6	Cs^{133}	498.9450(60)	1047.5929(94)	(2, -1)-(1, 0)	10589.3192(6)	- 0.0001	2778000
49B7	Cs^{133}	498.9530(60)	1047.6055(94)	(2, -1)-(1, 0)	10589.3192(8)	- 0.0001	1563000
49B8	Cs^{133}	498.9630(60)	1047.6212(94)	(2, -1)-(1, 0)	10589.3192(4)	- 0.0001	6250000
49C1	Cs^{133}	0.265(10)	0.757(29)	(2, 0)-(1, 0)	10962.7231(4)	+ 0.0002	6241000
49C2	Cs^{133}	0.267(10)	0.763(29)	(2, 0)-(1, 0)	10962.7227(4)	- 0.0002	6240000
49C3	Cs^{133}	0.269(10)	0.769(29)	(2, 0)-(1, 0)	10962.7229(5)	+ 0.0000	3996000
49C4	Cs^{133}	0.302(10)	0.863(29)	(2, 0)-(1, 0)	10962.7231(6)	+ 0.0001	2775000

Table VII. $\Delta\nu/\nu$ of 100-kHz crystal standard

|	Run	Date	$(\Delta\nu/\nu) \times 10^9$
for Au^{198}:	4	8/15/63	+ 9
	8	10/1/63	+ 14
	32	11/23/64	+ 8
	37	6/24/65	+ 3
	47	10/20/65	+ 8
	50	11/19/65	+ 9
for Au^{199}:	6	9/7/63	+ 10
	10	10/11/63	+ 13
	13	12/4/63	+ 2
	26	7/26/64	+ 2
	46	9/23/65	+ 6
	49	11/12/65	+ 9

at the field-independent point; no resonance was observed because of the small transition probability and in sufficient microwave power. With a more powerful klystron available, Run 37 was made to measure the doublet separation.

Run 47 was the first run made with a cavity hairpin; we began the run using about 100 mW of rf power. This yielded a resonance 45-kHz wide. By tracing out the power plot of Fig. 18 we determined that only about 10 μW of rf power was necessary to induce transitions with a cavity hairpin. After optimizing power we obtained a 10-kHz line, which is about the natural line width with a cavity 2 inches long.

Run 50 was made with a cavity hairpin 5-in. long in order to get final values for $\Delta\nu$ and the doublet separation. Each of the three transitions was swept twice with the C field and cavity in their normal orientations, once with the cavity direction reversed, and once with the C field reversed. This multiple sweeping provided a check on any possible resonance shifts such as the Millman effect.[10] None were observed. Line widths were typically 1 or 2 kHz wider than the natural line width of 3 kHz for a 5-inch cavity. We made a careful power plot for each transition before making the four sweeps mentioned above. The $\Delta\nu$ resonances consisted of the unre-solved lines $(5/2, \pm1/2) - (3/2, \mp 1/2)$, and therefore in the least-squares fitting routing each observation was entered twice, once with the quantum numbers corresponding to each transition. The error in the computer re-sult for a (Au^{198}) has been increased to compensate for this doubling of the number of $\Delta\nu$ observations.

Run 6, the first run with Au^{199}, was made to determine the sign of μ_I and get a better value of $\Delta\nu$. Resonances 6E, 6F, and 6G were ob-servations of $\Delta F = 1$ transitions. However, because the high frequencies involved and the use of the shorted strap hairpin gave us peculiar line shapes, these data were discarded. Resonances 6A, 6B, 6C, and 6D were at lower frequencies and the data were retained. Run 10 was made to observe the doublet at the field-independent point. Run 13 was made to replace the $\Delta F = 1$ resonances discarded from Run 6. These resonances are labeled 13A, 13B, 13C, and 13D in Table VI. The doublet was observed again yielding resonances 13G, 13H, 13I, and 13J. The standard transition was observed at 3100, 5400, and 6500 G and we obtained resonances 13E, 13F, 13K, 13L, 13M, and 13N. However, the shorted hairpin was used and later
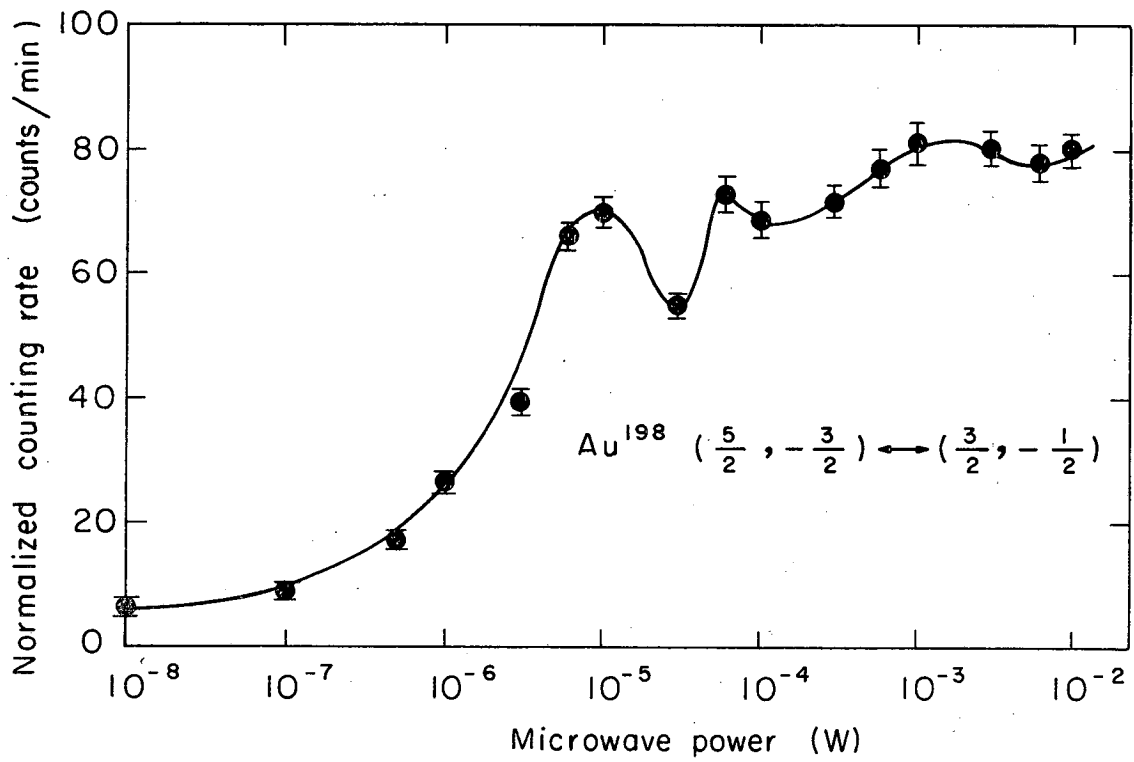
Fig. 18. Variation of resonance peak with microwave power for a K-band cavity hairpin 2 inches long.

information required that these data be discarded; Run 26 was made to replace these discarded data and obtain a value for g_J. Resonance 26A2 was taken with the C field reversed to check for a possible Millman effect[10] in the coaxial-style hairpin (shown on the right in Fig. 12) which was used for all the high-field g_J work. Run 26C was a failure due to vacuum problems.

Run 46 was the first run made for Au^{199} with a cavity hairpin. The line widths were typically the natural line width of 10 kHz for a cavity 2 inches long. Approximately 1 mW of rf power was required to induce the $\Delta M_F = 1$ transitions of the doublet using this TM_{010} mode hairpin. Run 49 was made to obtain final values of $\Delta \nu$ and the doublet separation. To check for shifts in the resonance frequency, we switched field and cavity directions in the same way we did for Au^{198}. The line widths were again approximately the natural line width for a cavity 5 inches long.

Figures 19 through 22 show a sample resonance for each member of the doublet, for a $\Delta \nu$ transition, and for a g_J-determining standard transition in Au^{198}. Figures 23 through 26 do the same for Au^{199}. The errors in the counting rates were calculated with the assumption that the statistical error in the total number of counts N was $\sqrt{N}$.

B. Description of Results

The computer routine used to calculate the values of a, g_J, and g_I giving the best least-squares fit to the data is called HYPERFINE 4DP, the DP indicating that this is a double-precision routine. A complete description of the mathematics involved is available from the Atomic Beam Group, Lawrence Radiation Laboratory. The program diagonalizes the Hamiltonian

$$\mathcal{H} = a \vec{I} \cdot \vec{J} - g_J \left(\frac{\mu_0}{h}\right) H J_z - g_I \left(\frac{\mu_0}{h}\right) H I_z \tag{59}$$

for gold with a $^2S_{1/2}$ ground state. All energies are expressed in units of MHz. The program assumes the interval rule by setting $a(I + \frac{1}{2}) = \Delta \nu$ exactly if no electric-quadrupole or magnetic-octupole interaction is allowed. This is the case for the ground state of gold.

The results of the least-squares fit are given in Table VIII. In calculating g_J, the routine uses the values of $g_J(K^{39})$ and $g_J(Cs^{133})$ given in Appendix A. From these results other parameters can be calculated, again
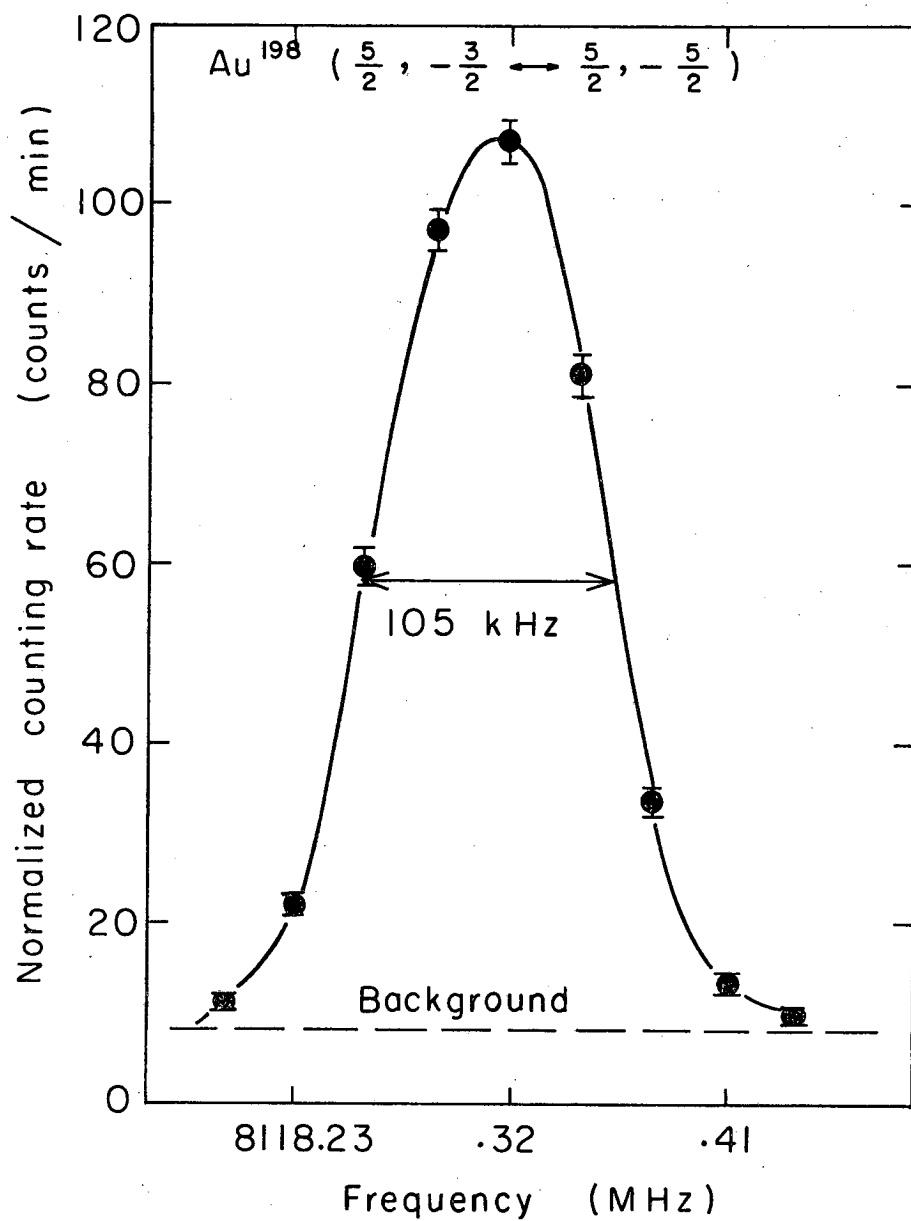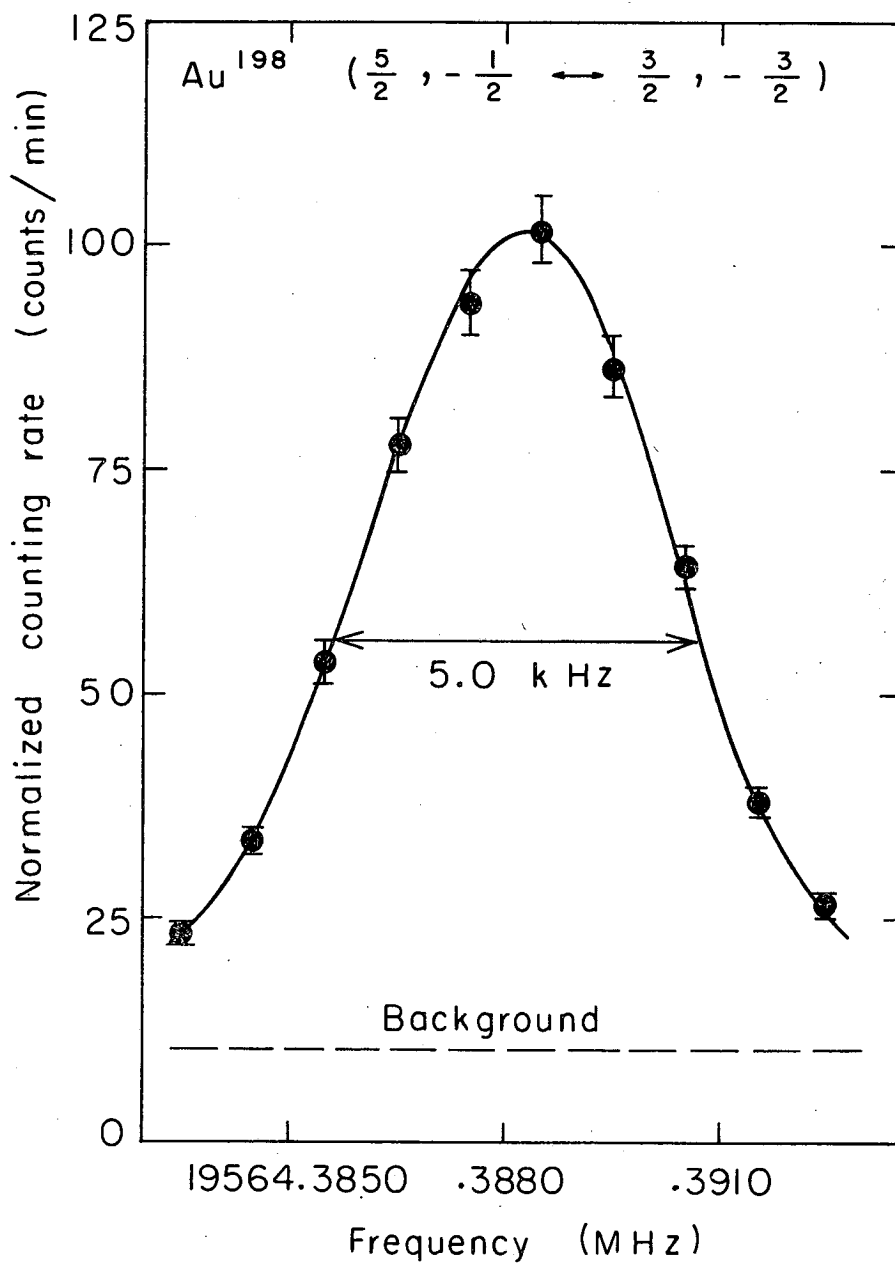
Fig. 19. Standard-transition resonance in Au^{198} at 6900 G.
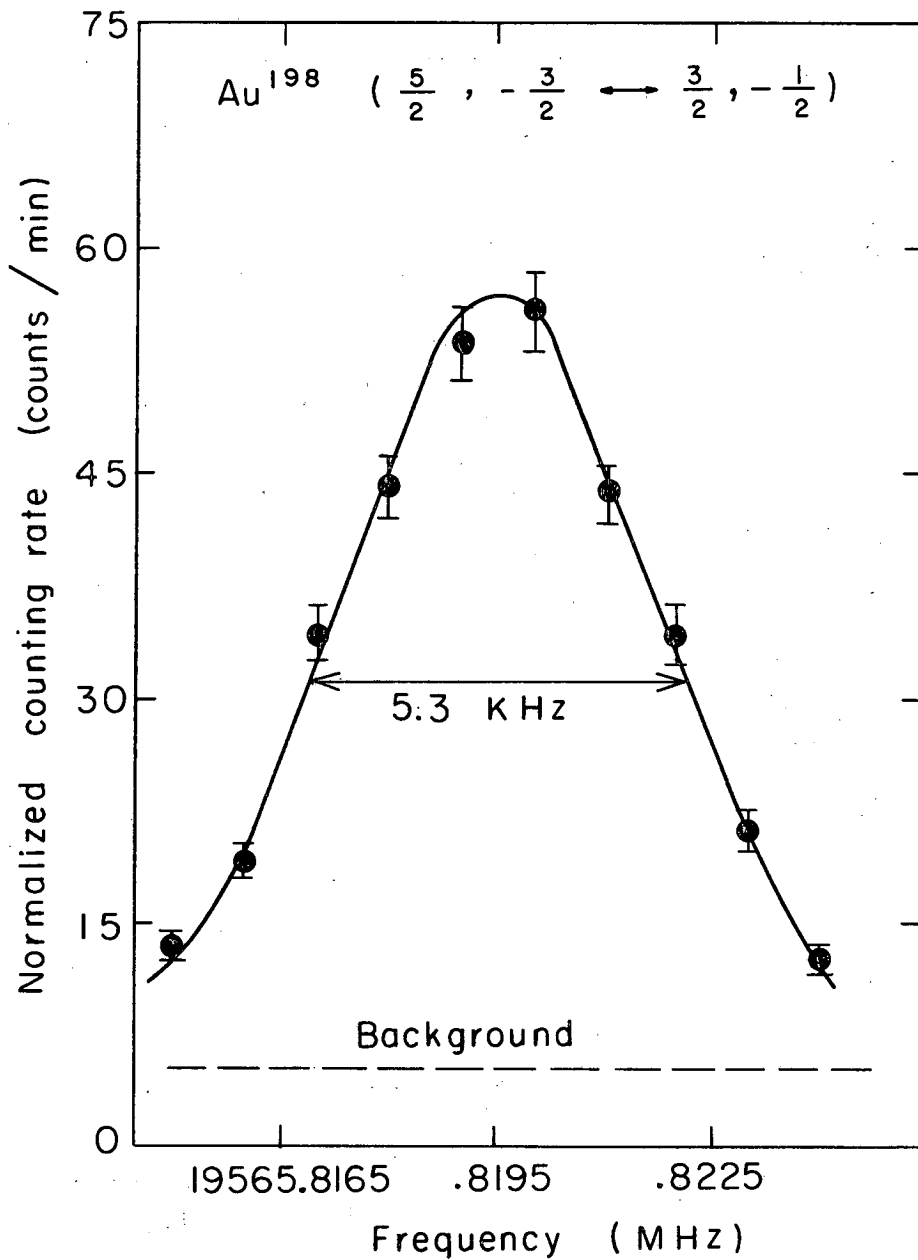
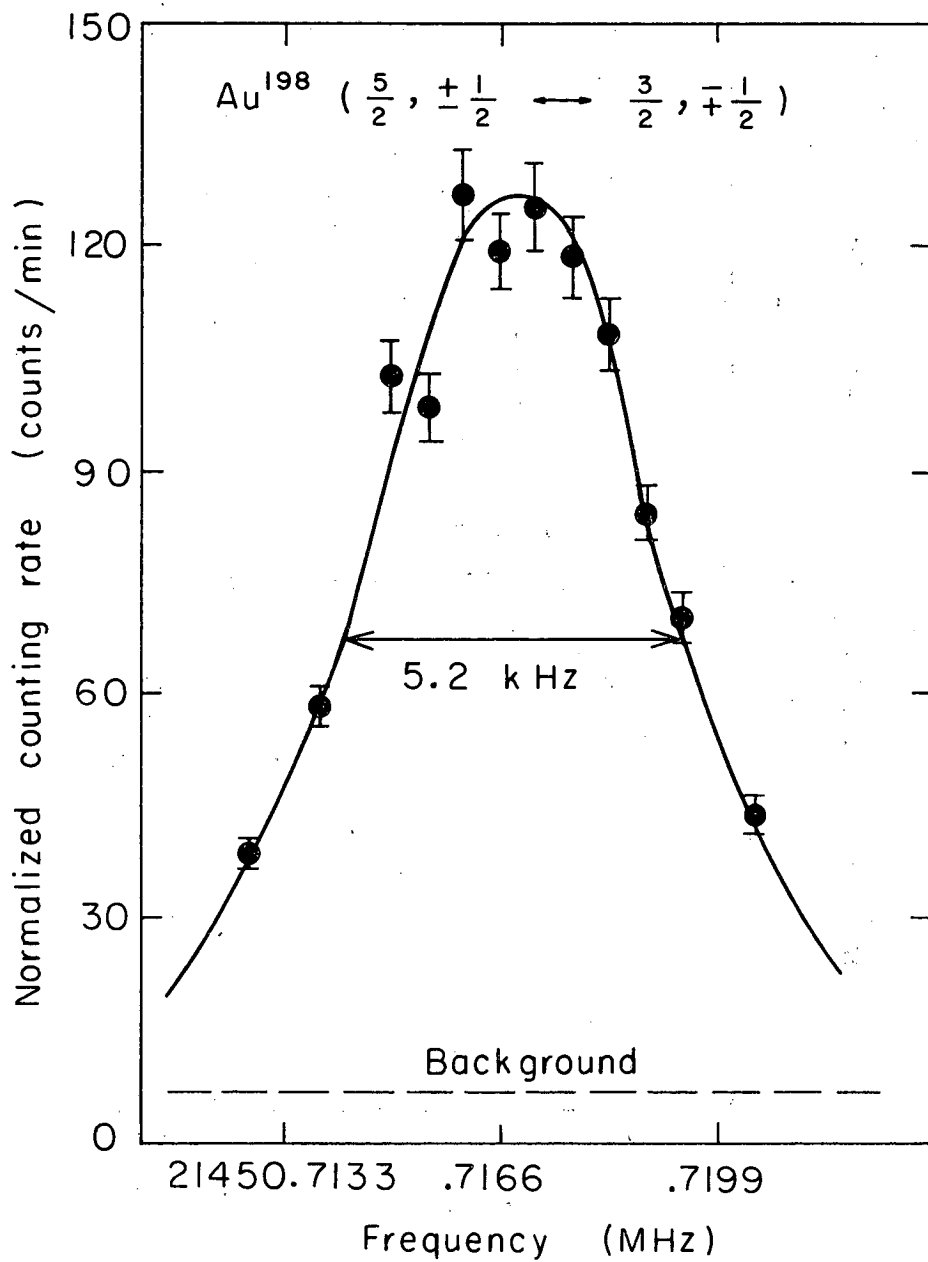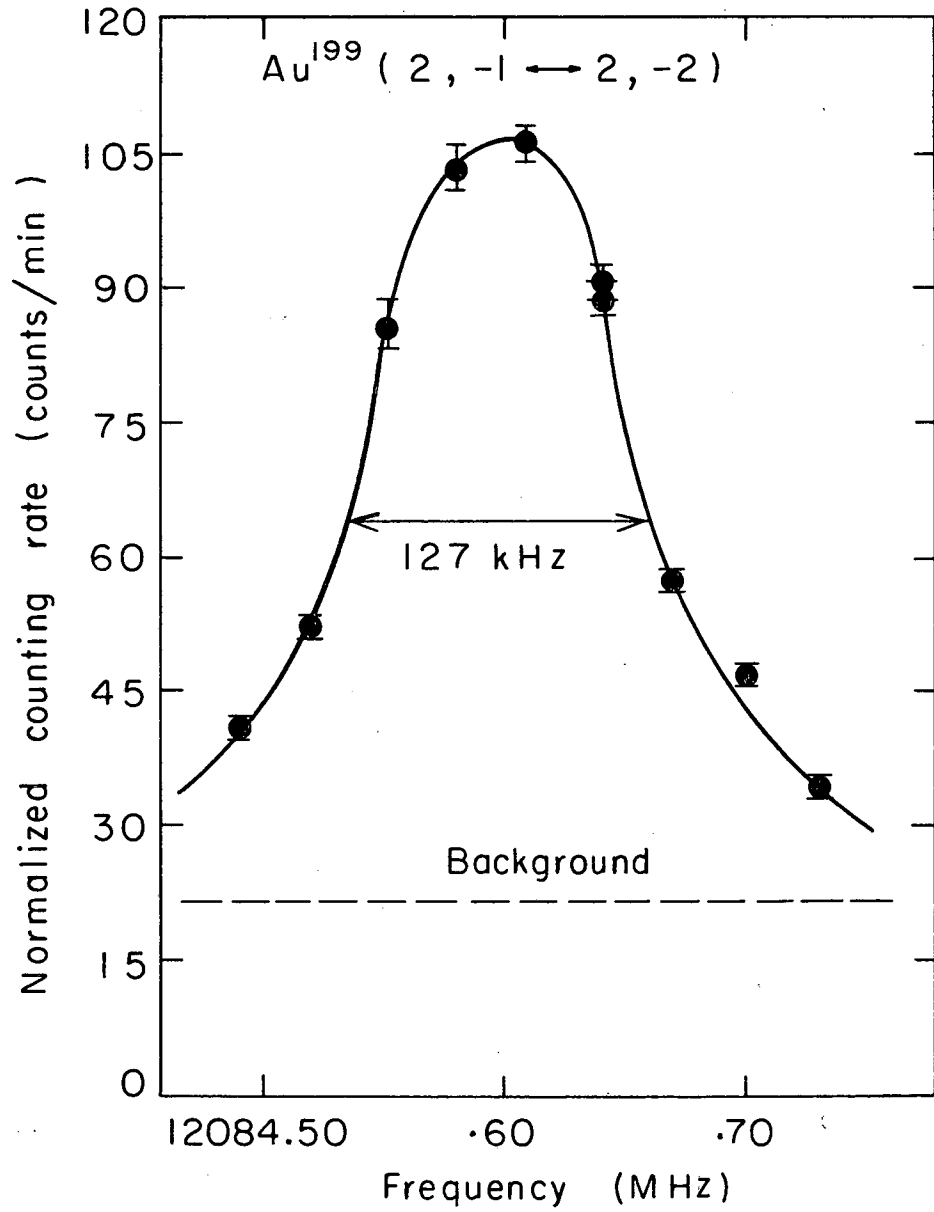Fig. 20. Doublet-transition resonance in Au198 at 3214.5 G.

Fig. 21. Doublet-transition resonance in Au[198] at 3214.5 G.
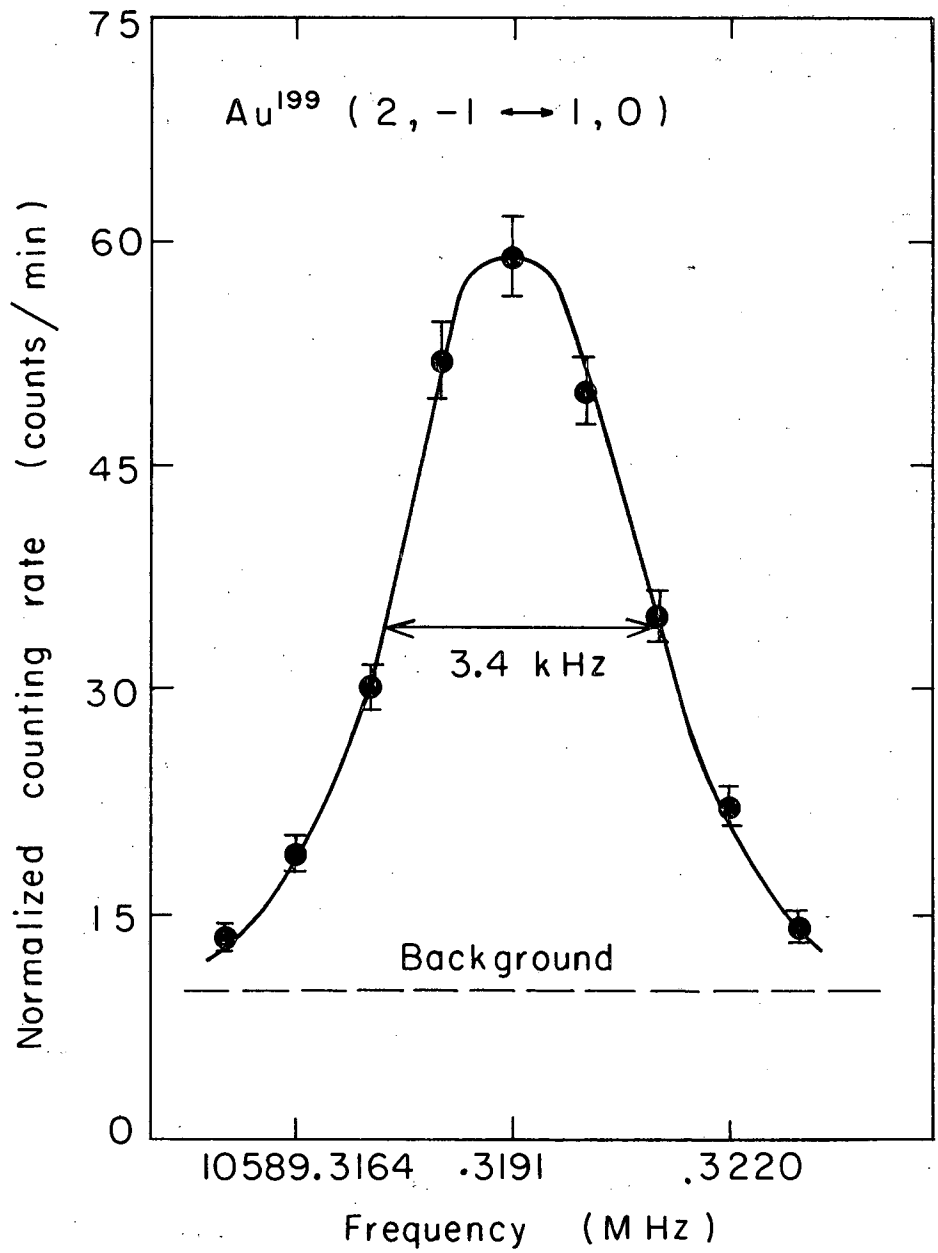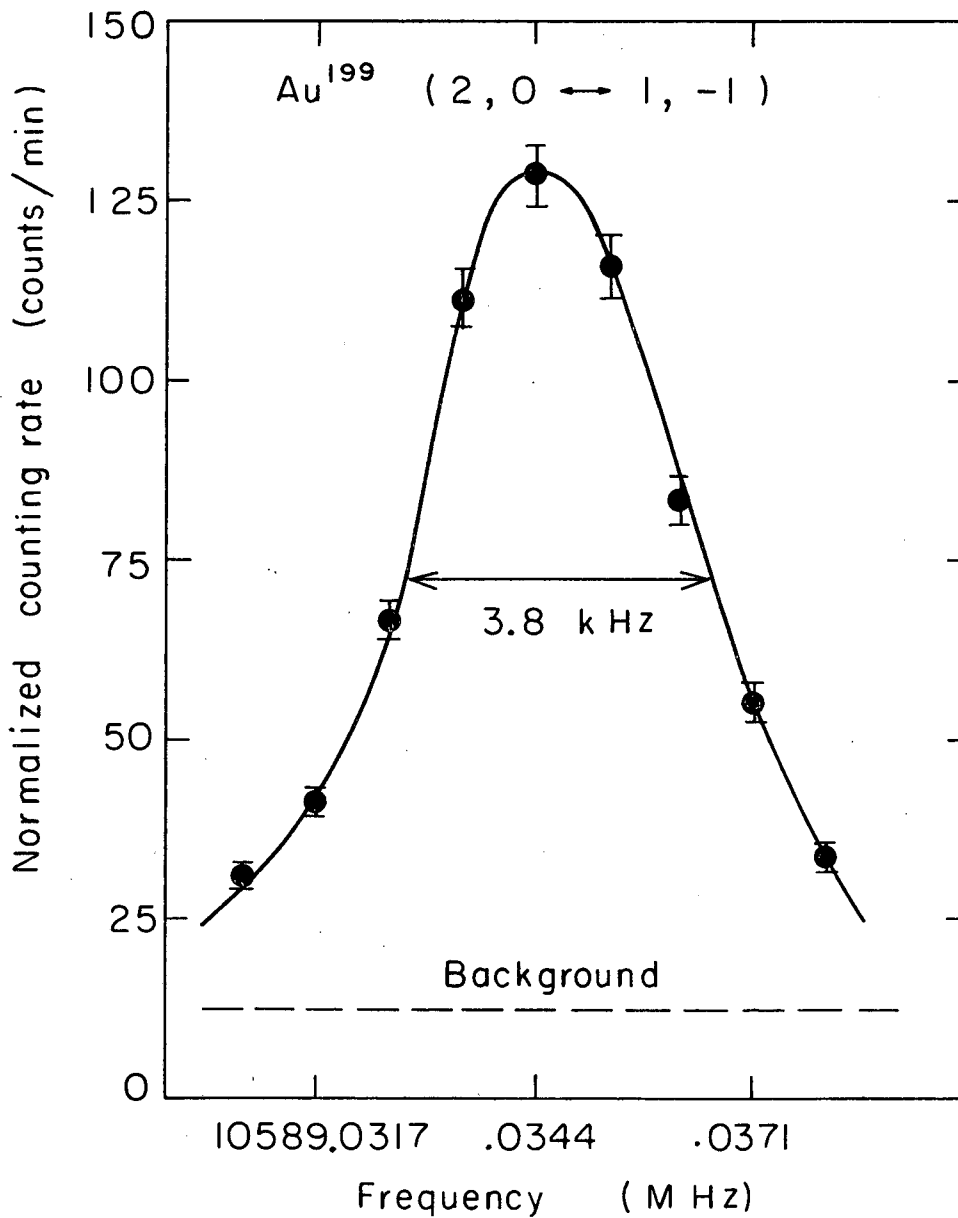
Fig. 22. A $\Delta\nu$-transition resonance in Au^{198} at 0.89 G.

Fig. 23. Standard-transition resonance in Au^{199} at 6700 G.

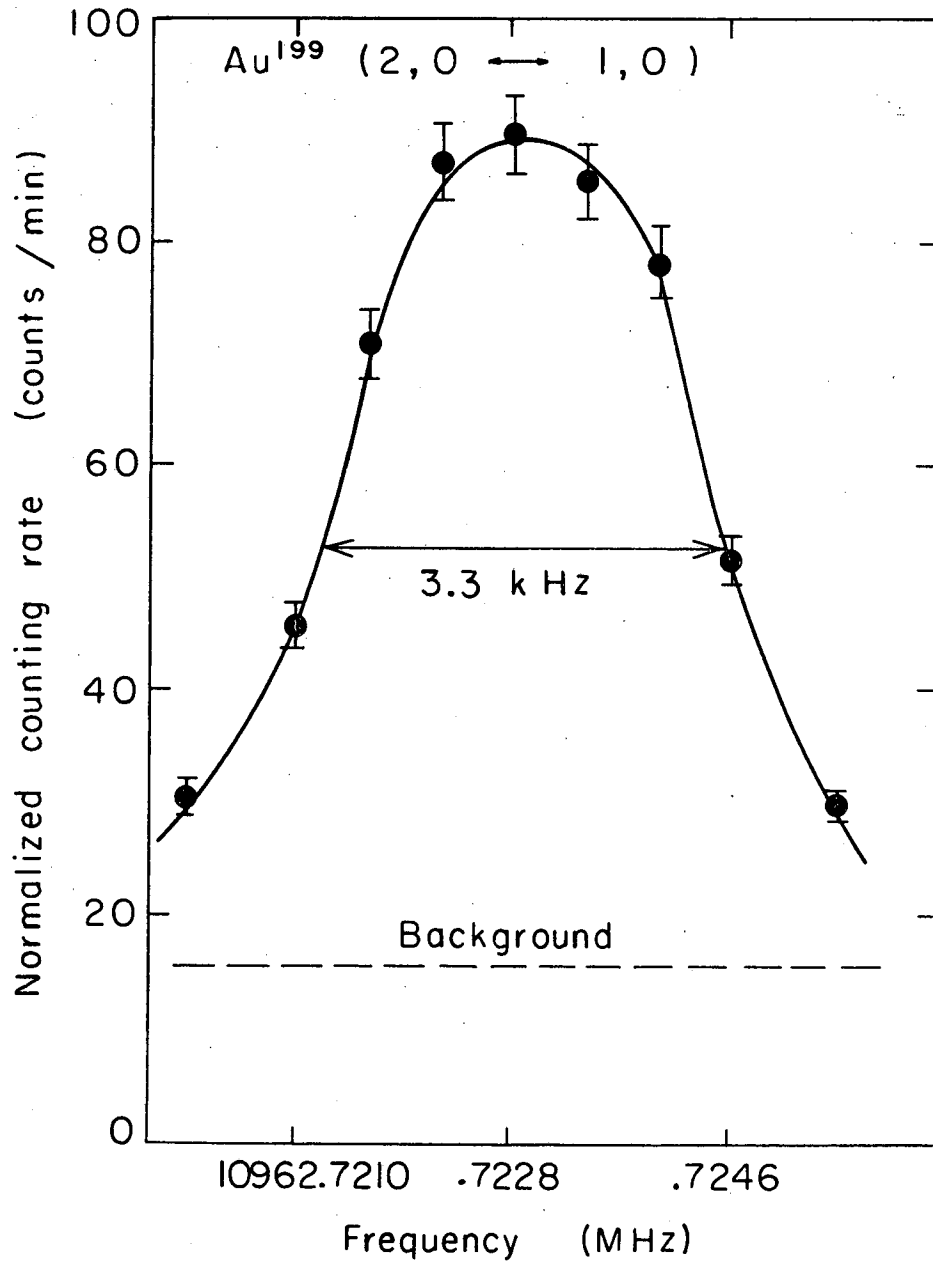Fig. 24. Doublet-transition resonance in Au^{199} at 1047 G.

Fig. 25.   Doublet-transition resonance in Au[199] at 1047 G.

Fig. 26. A $\Delta\nu$-transition resonance in Au^{199} at 0.77 G.

Table VIII. Results of the least-squares fit.

Parameter	Au^{198}(I=2)	Au^{199}(I=3/2)
a	8580.286697(97) MHz	5481.361327(71) MHz
$g_I \times 10^4$	1.59084(57)	0.9706(12)
g_J	-2.0033055(17)	-2.0033037(19)
Number of observations	47	37
χ^2	5.37	4.93

with the constants listed in Appendix A. These calculated parameters are given in Table IX. The final results, with errors increased to 2 standard deviations to account for any possible undetected systematic errors, are given in Table X. Since the g_J's of Au^{198} and Au^{199} agree to within 1 standard deviation, an average value has been listed for the quantities $g_J(Au^{198, 199})/g_J(K^{39})$ and $g_J(Au^{198, 199})/g_J(Cs^{133})$. These results supersede all of our previously published preliminary results.[39-42]

The nuclear magnetic moment calculated from the experimental value of g_I, with $\mu_I(nm) = g_I I (\frac{m_p}{m_e})$, is labelled $\mu_I(uncorr)$ in Tables IX and X. This value differs from the true value of the nuclear magnetic moment. This is because the external magnetic field in which the measurement of g_I was made is modified at the nucleus by the diamagnetic field produced by the atomic electrons. The true nuclear magnetic moment, labelled $\mu_I (corr)$ in Tables IX and X is obtained from $\mu_I(uncorr)$ by $\mu_I(corr) = (1-\sigma)^{-1} \mu_I(uncorr)$. The parameter σ has been calculated by Kopferman for all the elements.[43]

Since all second-order contributions to the hyperfine structure have been shown to be zero or negligible, we can be confident that the least-squares fit (or in this case the Breit-Rabi formula) yields the true g_I and g_J and the true a associated with s electrons.

The fit is very good, as shown by the low χ^2 and the small residuals (Tables V and VI) that are distributed randomly with respect to sign. The low χ^2 indicates that I was somewhat conservative in assigning errors to the input data. However, I feel my own judgment of data quality is as important in assigning errors as is the compatibility of these data with other data in a least-squares fit. Therefore, I have left the errors as originally assigned. Throughout this thesis the error in the last figures is indicated by a number in parentheses.

Note that although $\Delta\nu$ is listed in Table IX as being calculated from a, this designation is due only to the fact that program defines $\Delta\nu = a(I+\frac{1}{2})$ and fits a value of a to the data. The experimentally measured and determined quantity is really $\Delta\nu$. The meaning of a is discussed in Sec. V. Similarly for the electronic g factors, the ratios $g_J(Au^{198})/g_J(K^{39})$, $g_J(Au^{199})/g_J(K^{39})$, $g_J(Au^{198})/g_J(Cs^{133})$, and $g_J(Au^{199})/g_J(Cs^{133})$ are the quantities that were really determined by the experiment. The least-squares-fitting routine requires that some values be assumed for $g_J(Cs^{133})$ and for

Table IX.   Parameters calculated from the results of Table VIII

Parameter	$Au^{198}(I=2)$	$Au^{199}(I=3/2)$
$\Delta\nu$	21450.71674(24) MHz	10962.72265(14) MHz
μ_I(uncorr)	0.58419(21) nm	0.26733(33) nm
μ_I(corr)	0.58979(21) nm	0.26989(33) nm
$^{197}\Delta^{---}$	8.528(39) %	3.65(13) %
$g_J(Au^{---})/g_J(K^{39})$	1.00050445(87)	1.00050355(93)
$g_J(Au^{---})/g_J(Cs^{133})$	1.00038140(87)	1.00038049(93)

Table X.   Final results

Parameter	$Au^{198}(I=2)$	$Au^{199}(I=3/2)$
$\Delta\nu$	21450.7167(5) MHz	10962.7227(3) MHz
μ_I(uncorr)	0.5842(4) nm	0.2673(7) nm
μ_I(corr)	0.5898(4) nm	0.2699(7) nm
$^{197}\Delta^{---}$	8.53(8) %	3.7(3)%

$$g_J(Au^{198,\,199})/g_J(K^{39}) = 1.000504(2)$$

$$g_J(Au^{198,\,199})/g_J(Cs^{133}) = 1.000381(2)$$

$g_J(K^{39})$ and then fits a value of $g_J(Au^{198})$ or $g_J(Au^{199})$ to the data. Precisely the same ratios and values of a and g_I result if the assumed values of $g_J(K^{39})$ and $g_J(Cs^{133})$ are changed by ± 50 parts per million and doubtless a much larger change in the absolute scale of the g factors could be tolerated.

V. INTERPRETATION OF RESULTS

A. Electronic Results

If Eq. (18) is evaluated for Au^{198} and Au^{199} with n_0 = 1.215 (Ref. 44), $(1 - \frac{d\sigma}{dn})$ = 1.482 (Ref. 45), and F_r = 2.1976; if these results are corrected for a value of δ = 11.2% (Ref. 46) and for the values $\epsilon(199)$ = 8.3% and $\epsilon(198)$ = 4.8% (the values of ϵ to be calculated in Sec. V. B), we get $a(198)$ = 8790 MHz and $a(199)$ = 6080 MHz. Since the calculation is probably good only to 10%, these values agree with the observed a's. The calculated values are larger than the observed values, however, if the error is ignored. Childs and Goodman have noted that this is true for Au^{197} as well.[8] They ascribed the discrepancy to core polarization. Although it is possible to promote core s electrons to d states, this is a negligible third-order effect. The total effect of core polarization can be described by mixing configurations, of the type $ns6s^2$ and ns6sn's n < 6 < n', with the ground-state 6s configuration.[8] In any event, the effect of core polarization will only be to introduce the same correction factor into Eq. (18) for all isotopes. Hence the anomaly will be unaffected and no attempt will be made here to calculate the extent of core polarization. As we have shown that second-order hfs contributions are zero or negligible, we can conclude that the a values computed by the least-squares routine describe the hyperfine structure due to s electrons in the isotopes Au^{198} and Au^{199}.

If the g factors of potassium and cesium are assumed to be correct as given in Appendix A, then we have for the absolute g factor of gold, g_J = - 2.003305(2). The Margenau and Lamb corrections can be calculated with knowledge of the value of the effective principal quantum number, n_0 = 1.215 (Ref. 44). This calculation yields $(\Delta g)_M$ = 47×10^{-6} and $(\Delta g)_L$ = 12×10^{-6}. If we combine this calculation with the quantum electrodynamical correction of $- 2319 \times 10^{-6}$, we get $g_J(Au)_{theory}$ = - 2.002260 exclusive of corrections from configuration mixing. If configuration mixing is to explain the difference between this value and the observed value, it is unlikely that the rough method of estimate used by Phillips[21] could provide a correction of - 0.001045. Her method begins to break down for the alkalis at rubidium and is quite poor for cesium (see Appendix B). For gold one would expect the agreement to be so poor as to make the calculation worthless. Presumably, one could obtain good agreement if the calculation were done

very carefully and if enough spectroscopic data especially x-ray data, were available, since no mechanism other than configuration mixing seems to be able to account for the increase in g_J with increasing Z.

B.   Nuclear Results

The spin of Au^{199} is 3/2, as is the spin of all the odd-A gold isotopes.[1,3,13] The most reasonable explanation for this is that these spins are due to the $d_{3/2}$ hole in the proton configuration $(1g_{7/2})^8$ $(2d_{5/2})^6$ $(1h_{11/2})^{12}$ $(2d_{3/2})^3$, where only states above the closed shell at 50 protons are listed.   This assignment of the $2d_{3/2}$ protons is consistent with the observed positive nuclear quadrupole moment of Au^{197} (Ref. 8).   It is also consistent with the fact that the observed moment is closest to the Schmidt moment corresponding to $j = \ell - \frac{1}{2}$.   If the odd neutron in Au^{198} is assumed to be in a $3p_{1/2}$ state, then the rules (40) unambiguously predict that the spin is 2.   This is indeed the observed spin.   This neutron assignment is also consistent with the observed spin and parity of Hg^{199} (Ref. 47).

The Schmidt predictions for the magnetic moments are: $\mu(199)$ = 0.124 nm, and $\mu(198)$ = 0.762 nm.   Several mechanisms are available to explain the deviation of the observed moments from these values.

One mechanism that does not work is the use of higher seniority coupling schemes.   If for example the proton configuration is taken to be $[(1h_{11/2})^{10}_{j_1=2}] [(2d_{3/2})^3_{j_2=3/2}]$, with j_1 and j_2 coupling to a spin of 3/2, the predicted moment for Au^{199} becomes 1.84 nm.   Of the nearly 20 such coupling schemes that are allowed by the Pauli exclusion principle and would be more or less reasonable for Au^{199}, not one predicts a positive magnetic moment smaller than 0.7 nm.   For Au^{198}, an odd-odd nucleus, the possible coupling schemes are even greater.   But again, no reasonable scheme comes close to predicting the magnetic moment observed.

Another mechanism that fails to predict the observed magnetic moments is the configuration-mixing theory of Arima and Horie.   The coefficients of Tables I and III are evaluated with parameters given by Stroke et al.,[33] and are used in Eq. (49) to obtain values of μ_I.   Assuming various arrangements of even numbers of nucleons in unfilled shells, one obtains 32 different corrections to the Schmidt moments.   This is because the coefficients of Tables I and III depend on the occupation numbers of the states involved

in the excitation. For gold the only excitations considered were:

$$\text{for protons} \begin{cases} 2d_{3/2} - 2d_{5/2} \\ 1h_{9/2} - 1h_{11/2} \end{cases} \qquad \text{for neutrons} \begin{cases} 3p_{1/2} - 3p_{3/2} \\ 1i_{11/2} - 1i_{13/2} \end{cases}.$$

However, not one scheme of the 32 tried gave a magnetic moment for Au^{199} smaller than 0.5 nm. Arima and Horie did a similar calculation for Au^{197} and Au^{199} using various nuclear potentials.[48] For both isotopes they got magnetic moments varying from 0.3 to 0.4 nm. The agreement is not bad for Au^{199} but it is poor for Au^{197}. Their predicted value for $\mu(Au^{198})$ is equal to the Schmidt value.

Kisslinger and Sorensen computed the magnetic moments of many nuclei based on a shell model with simple residual forces.[49] They con‐ sidered both configuration mixing and collective motion or phonon cor‐ rections to the Schmidt moments. Their approach should be particularly well-suited to the gold nuclei which are neither spherical nor strongly de‐ formed. For Au^{195}, Au^{197}, and Au^{199} they found μ_I to be 0.9 nm. They point out that this prediction differs drastically from the observed moments because of the configuration-mixing corrections; these could be made smaller by choosing a potential more like Arima and Horie's. However, they also point out that this causes the magnetic moments for the excited states of the gold nuclei to be unreasonably large.

In view of the seeming hopelessness of theoretically predicting the magnetic moments, we will construct an interpretation of the observed moments by the following scheme: The theoretical magnetic moments of Au^{197}, Au^{199}, and Hg^{199} will be made to fit the observed moments either by choosing the proper value of g_s in the Schmidt formula (the method of quenched g factors) or by choosing the proper admixture coefficient in Eq. (49) for some single-excitation configuration-mixing scheme. For each value of g_s and a, a value of ϵ can be calculated using Eq. (57). The scheme which then predicts the best values of $_{197}\Delta^{199}$ and $_{197}\Delta^{198}$ will be chosen as best describing the observed facts. The value of $\epsilon(198)$ can be taken to be $\epsilon(Au^{199}) + \epsilon(Hg^{199})$, or $\epsilon(Au^{197}) + \epsilon(Hg^{199})$, and both choices will be considered. Hg^{199} is used to give information on the odd neutron in Au^{198} since nothing is known about Pt^{197}. Table XI

Table XI. Predicted values of $^{197}\Delta^{199}$

Mechanism	Excitation energy (MeV)	$\epsilon(\text{Au}^{197})$ (%)	$\epsilon(\text{Au}^{199})$ (%)	$^{197}\Delta^{199}$ (%)
Effective g_s	- - -	13.0	4.9	7.7
$\nu(p_{1/2}-p_{3/2})$	0.5	13.6	8.3	4.9
$\nu(i_{11/2}-i_{3/2})$	2.0	13.7	8.4	4.9
$\pi(h_{9/2}-h_{11/2})$	2.0	13.1	6.1	6.6
$\pi(d_{3/2}-d_{5/2})$	1.5	13.1	6.4	6.4

Experimentally, $^{197}\Delta^{199} = 3.7(3)$ %

gives the results of this calculation for $^{197}\Delta^{199}$.

It is easily seen that the use of effective g_s factors leads to a poor value for the anomaly. Both neutron excitations give reasonable agreement and we choose $\nu(p_{1/2}-p_{3/2})$ as best describing the situation since it has the lower excitation energy.

Because Hg^{199} has a single $p_{1/2}$ neutron, there can be no configuration mixing for the interaction of Eq. (48). Hence, we compute ϵ for Hg^{199}, using an effective g_s. We get $\epsilon(Hg^{199}) = -3.5\%$. The value of the moment was taken to be 0.503 mn (Ref. 50). This value allows for two values of ϵ:

a) $\epsilon(Au^{198}) = \epsilon(Au^{197}) + \epsilon(Hg^{199}) = 10.1\%$

b) $\epsilon(Au^{198}) = \epsilon(Au^{199}) + \epsilon(Hg^{199}) = 4.8\%$.

The resulting anomalies are:

a) $^{197}\Delta^{198} = 3.2\%$,

and

b) $^{197}\Delta^{198} = 8.4\%$.

Obviously, only b) gives a reasonable result. Thus the best fit to the data is obtained by using the nuclear parameters of Au^{199}, rather than those of Au^{197}.

The magnetic moment of Au^{198} can be calculated by coupling $\mu(Hg^{199})$ to $\mu(Au^{197})$ or $\mu(Au^{199})$. The former choice gives $\mu(Au^{198})=0.65$ nm and the latter choice gives $\mu(Au^{198}) = 0.77$ nm. Although neither agrees very well with the observed moment of 0.59 nm, this is probably as good as can be expected for an odd-odd nucleus. The fact that the moment calculated with the Au^{197} moment agrees better than that calculated with the Au^{199} moment seems to contradict the preceding paragraph. However, the theory of odd-odd nuclei being what it is, this is not surprising.

In conclusion, then, we can explain the magnetic-dipole moments of Au^{198} and Au^{199} and their anomalies with respect to Au^{197} by assuming different amounts of $p_{1/2}-p_{3/2}$ quasi-particle excitations in the neutron states of these isotopes. All purely theoretical attempts to do the same fail.

VI. CONCLUSIONS

This research has definitely shown that the hyperfine-structure anomaly is not necessarily a "1% effect" as it is often labelled. The usefulness of this anomaly as a parameter describing the nucleus is not great because it is hard to interpret, particularly for odd-odd nuclei. However, it can be useful, as in this research, as a check on the validity of a configuration-mixing scheme to explain nuclear magnetic moments.

The failure of all current nuclear models to predict the observed magnetic moments of the gold nuclei makes the acquisition of more nuclear data for these isotopes desirable. Even more desirable is information about the radioactive odd-A platinum isotopes, about which nothing is known. With such information available, a thorough theoretical investigation of the nuclei in this mass region could be made.

ACKNOWLEDGMENTS

APPENDICES

A. Values of physical constants assumed[a]

$$\mu_0/h = 1.399613(14) \text{ (Ref. 51)}$$

$$m_p/m_e = 1836.10(12) \text{ (Ref. 52)}$$

$$\Delta\nu(Au^{197}) = 6099.320184(13) \text{ (Ref. 53)}$$

$$g_I \times 10^4 (Au^{197}) = 0.520994(33) \text{ (Ref. 53)}$$

$$g_J(K^{39}) = -2.0022954(22)^b$$

$$g_J(Cs^{133}) = -2.0025417(24)^b$$

$$(1 - \sigma)^{-1} = 1.00958 \text{ (Ref. 43)}$$

---

[a] None of the errors indicated in the values above were used in computing the errors in the results of this thesis.

[b] See Appendix B.

B. Measurement of the electronic g factors of
Cs, Rb, K, and Na

Early in this work I was trying to extract the values of $\Delta\nu$ and g_I for Au^{198} and Au^{199} from observations of the standard transition in each isotope alone. The value of g_J for K^{39} and Cs^{133} had to be known accurately because these isotopes were used to calibrate the magnetic field. The lack of good values for the g factors of all the alkalis inspired us to measure them. Tuncay Incesu, and I made the Rb and Cs measurements, and Professor Adnan Saplakoglu and Erol Aygun made them for Na. The Na result is included here for completeness.

Our method was as follows: First, the standard transition was observed in K^{39}, then in the other alkali under investigation, then again in K^{39}, etc., until approximately 25 observations were made for each isotope. A single observation consisted of the average of six recorded frequencies. These six frequencies consisted of three pairs of frequencies symmetrically spaced about the peak of a resonance from somewhere near the peak to somewhere near half-maximum. All this was done as rapidly as possible to eleminate effects of magnetic-field drift. Typically, we could switch from one alkali to the other in about 2 minutes. The measurements were made at a variety of magnetic-field strengths, with the strength used at any one time (1000 to 5000 G) depending on the alkali.

In the first series of measurements on cesium we used the shorted hairpin on the left in Fig. 12, and discovered the difficulties of using such a hairpin at high fields. This effect was discussed in Sec. III.C. All subsequent measurements were made with a terminated coaxial hairpin.

Figures 27 through 30 show chart-recorder traces of the resonances obtained in each of the alkalis during the series of experiments. All of the resonances observed are very free from structure and asymmetry and display excellent signal-to-noise characteristics.

The average of the two potassium frequencies bracketing a particular frequency for the other alkali involved was used to calibrate the magnetic field for that alkali frequency. The least-squares fitting routine, HYPERFINE 4DP, mentioned earlier was used to fit the data. A value was assumed for $g_J(K^{39})$ and the g_J of the other alkali was varied until the best fit was obtained. Table XII gives the results of the least-squares fit and
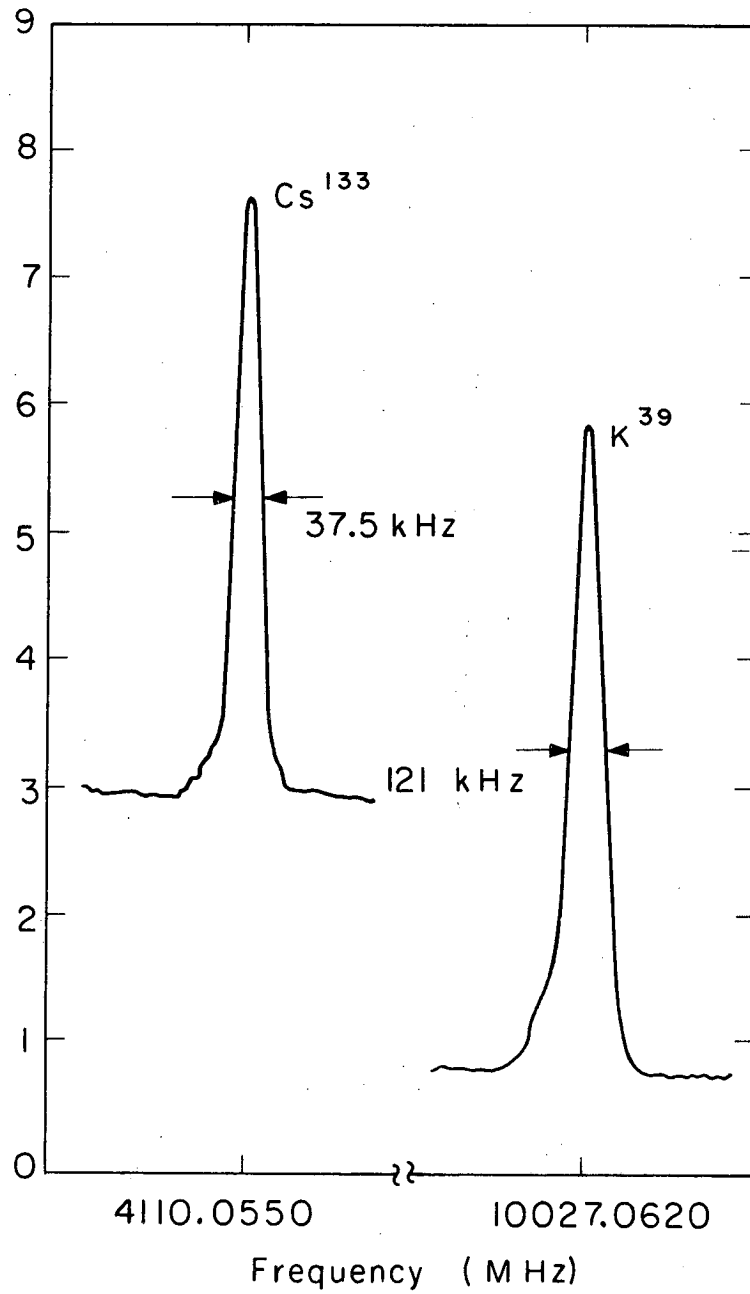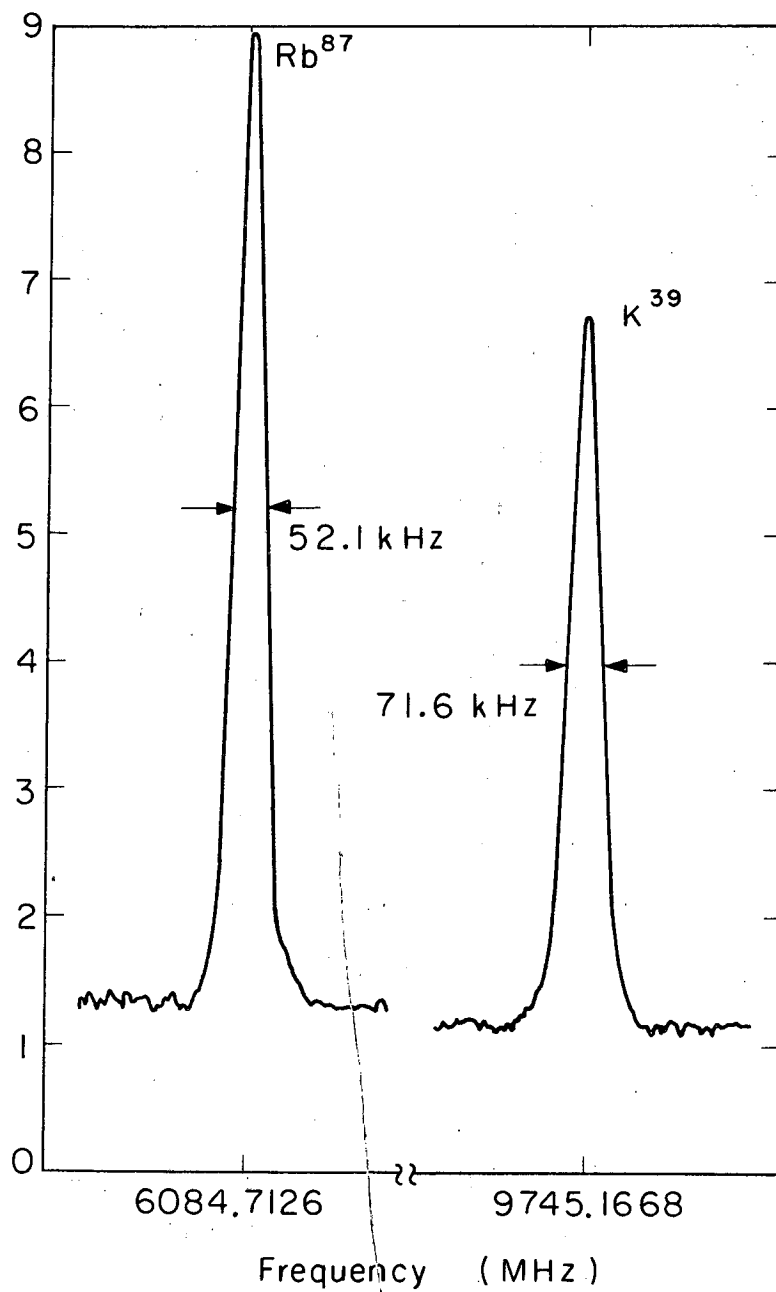
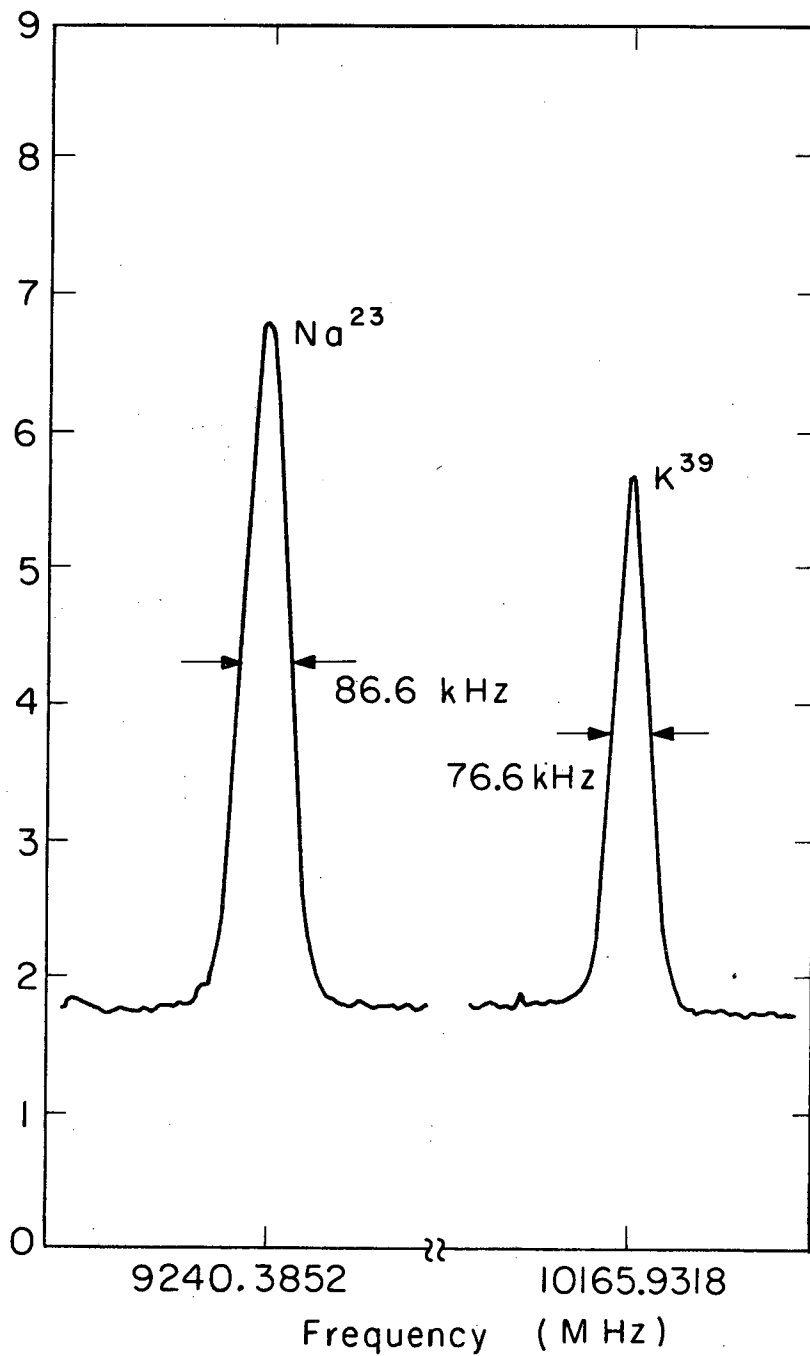Fig. 27. Chart-recorder tracings of the standard transition in Cs^{133} and K^{39} at 3700 G.
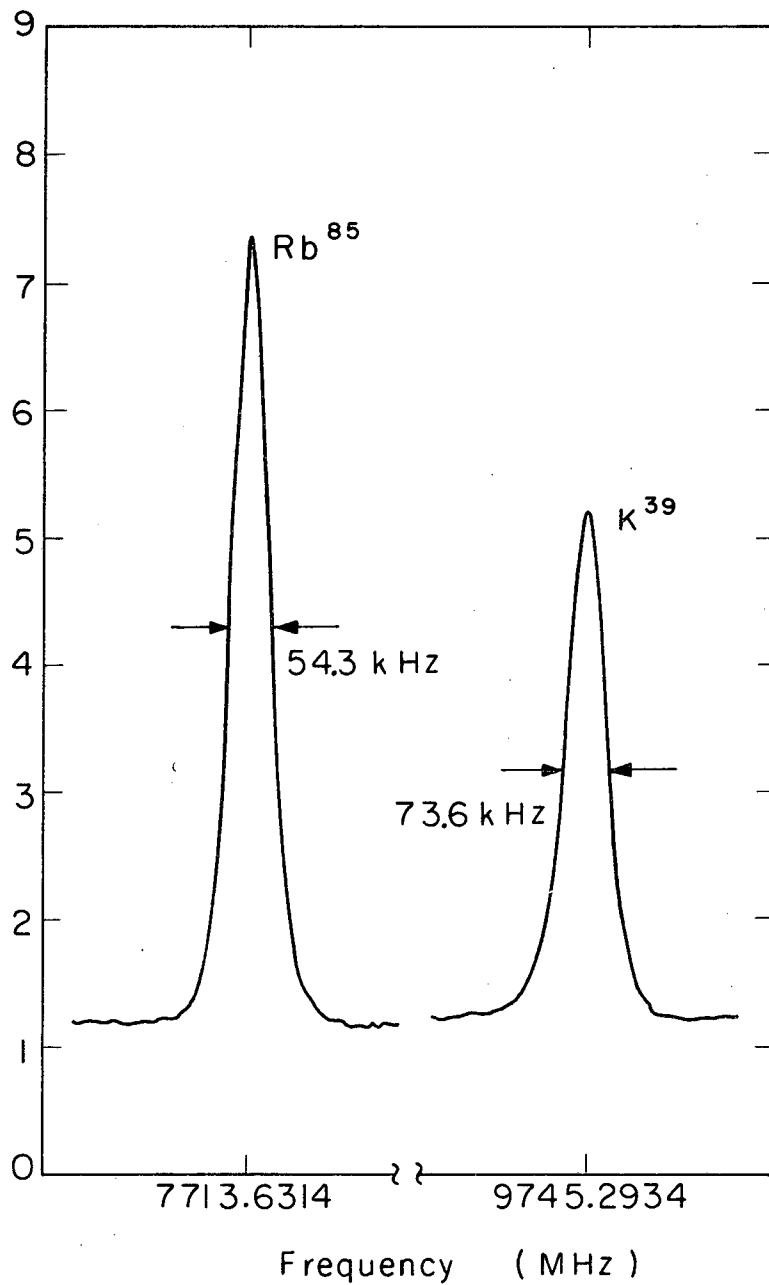
Fig. 28. Chart-recorder tracings of the standard transition in Rb[85] and K[39] at 3600 G.

Fig. 29. Chart-recorder tracings of the standard transition in Rb[87] and K[39] at 3600 G.

Fig. 30. Chart-recorder tracings of the standard transition in Na^{23} and K^{39} at 3750 G.

MUB-10167

Table XII. g_J Data and least-squares results

	H (G) at which measurements were made	Value assumed for $g_J(K^{39})$	Total number of observations	χ^2	Least-squares g_J results
Na^{23}	1500, 2411, 3300, 3550, 3750, 3950, 4200	-2.002298	256	85.8	-2.00229898(17)
Rb^{85}	1800, 2700, 3600, 4500	-2.002309	122	8.2	-2.00234556(20)
Rb^{87}	1800, 2700, 3600, 4500	-2.002309	122	3.7	-2.00234550(20)
Cs^{133}	900, 1300, 1900, 2400, 3000, 3700, 4400	-2.002309	314	21.2	-2.00255541(33)

Table XIII lists the hfs constants that were assumed for the alkalis in the calculation.

By dividing the results of the least-squares fit by the value of $g_J(K^{39})$ assumed, we obtain the quantity actually determined by this experiment, namely, the ratio of $g_J(Cs^{133})$, $g_J(Rb^{87})$, $g_J(Rb^{85})$, or $g_J(Na^{23})$ to $g_J(K^{39})$. Final values for these ratios, with errors increased to two standard deviations to allow for any undetected systematic errors, are given in Table XIV. The average value of the ratios $g_J(Rb^{85})/g_J(K^{39})$ and $g_J(Rb^{87})/g_J(K^{39})$ is listed there as $g_J(Rb^{85,\,87})/g_J(K^{39})$ since the two values agree extremely well and there is no reason to expect an isotopic change in g_J for an element this heavy. These results supersede all previously published preliminary results.[58,59]

Second-order corrections vanish for the ground-state hyper-fine structure of the alkalis for the reasons given earlier for gold. The second-order quadrupole corrections for alkalis should be only a thousandth those of gold. This together with the fact that the data fits well makes us very confident of our results.

The theoretical corrections to the value $g_J = -2$, mentioned in Sec. II. A., were calculated for the alkalis by Perl.[60] Although there are errors in his paper, as noted by Hughes,[61] none of the numbers we quote are in error. Table XV lists these calculated corrections. Balling and Pipkin's measurement of $g_J(Rb^{85})/g(e)$ by optical pumping[51] enables us to connect our measurements with Crane's measurement of the absolute g factor of the free electron.[17] Using $g_J(Rb^{85})/g(e) = 1.0000063(10)$ and $g(e) = -2.002319244(54)$ together with our results yields the experimental values for the absolute g factors of the alkalis listed in Table XV. The agreement between these values and the theoretical values given there is quite good. The increasing deviation with atomic number would seem to indicate that the configuration-mixing corrections should be recalculated. Phillips indicates that these corrections are only rough estimates.[21]

Figures 31 through 33 summarize the results of this research.

Table XIII. Constants assumed for the alkalis in the
least-squares-fit calculations

	$\Delta\nu$	$g_I \times 10^4$ [a]
Na^{23}	1771.6260470(23)[b]	8.04639[c]
K^{39}	461.719723(30)[d]	1.41922[c]
Rb^{85}	3035.732439(5)[e]	2.93700[c]
Rb^{87}	6834.682614(3)[e]	9.95323[c]
Cs^{133}	9192.631770[f]	3.98994[c]

[a] This assumes $\mu(H^1)_{uncorr} = 2.792670$ nm.

[b] See Ref. 54.

[c] See Ref. 55

[d] See Ref. 56

[e] See Ref. 57

[f] The Cs^{133} $\Delta\nu$ is the present frequency standard for other $\Delta\nu$'s.

Table XIV. Final g_J results

$$g_J(Na^{23})/g_J(K^{39}) = 1.0000007(2)$$

$$g_J(Rb^{85,\,87})/g_J(K^{39}) = 1.0000182(2)$$

$$g_J(Cs^{133})/g_J(K^{39}) = 1.0001231(3)$$

Table XV. Comparison of theoretical and experimental g_J's

|	Na	K	Rb	Cs
$(\Delta g)_{QED}$	- 0.002319	- 0.002319	- 0.002319	- 0.002319
$(\Delta g)_M$	+ 0.000022	+ 0.000020	+ 0.000020	+ 0.000018
$(\Delta g)_L$	+ 0.000004	+ 0.000004	+ 0.000004	+ 0.000004
$(\Delta g)_{CM}$	- 0.000002	- 0.000005	- 0.000050	- 0.000140
$(\Delta g)_{total}$	- 0.002295	- 0.002300	- 0.002345	- 0.002447
g_J(theor)	- 2.002295	- 2.002300	- 2.002345	- 2.002447
g_J(exper)	- 2.002297(2)	- 2.002295(2)	- 2.002332(2)	- 2.002542(2)
Deviation (ppm)	-1 (1)	+3(1)	+6(1)	-48(1)
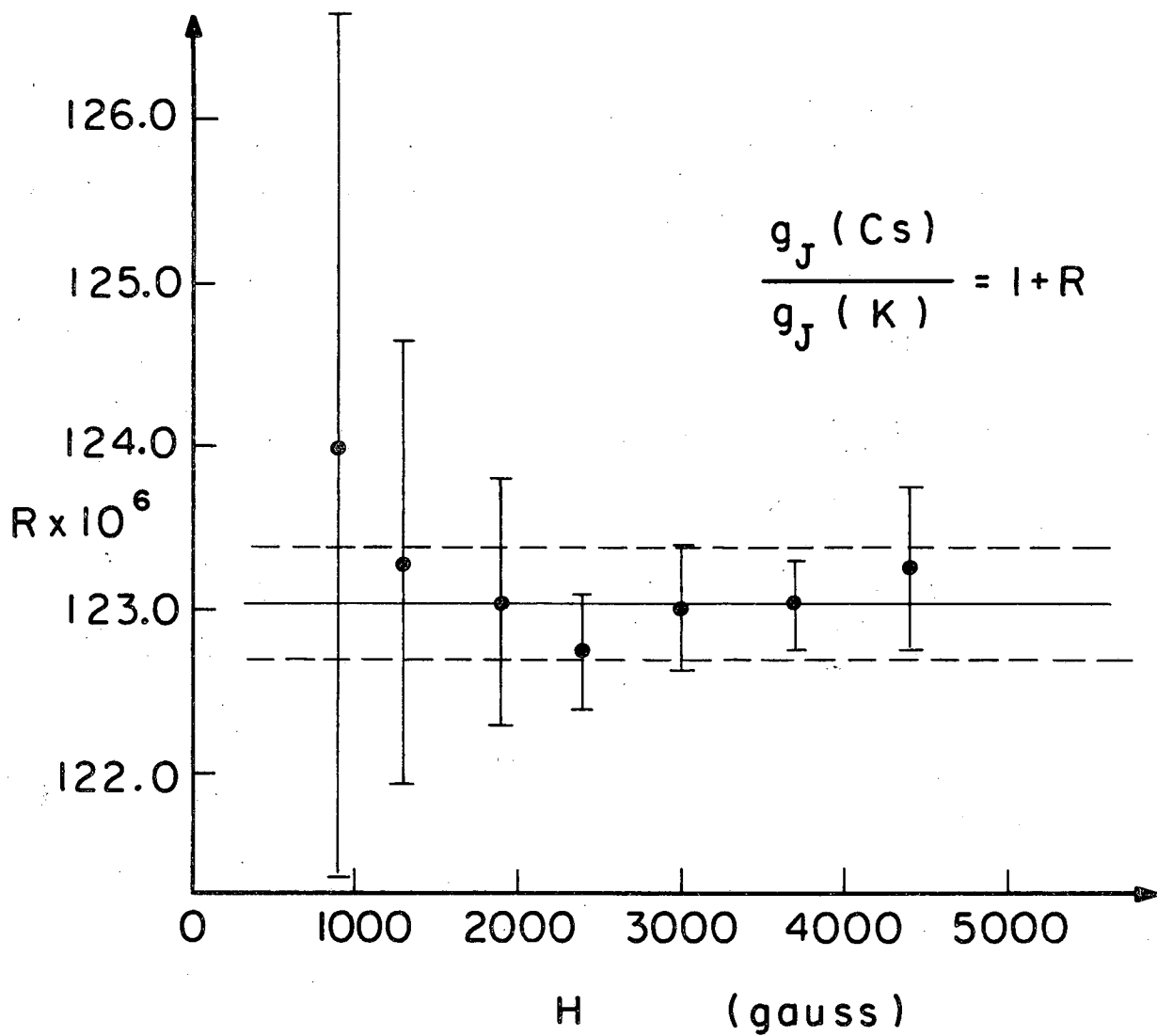
Fig. 31. Plot of the ratio $g_J(Cs^{133})/g_J(K^{39})$ versus magnetic field.

$$\frac{g_J \ (Rb)}{g_J \ (K)} = 1 + R$$
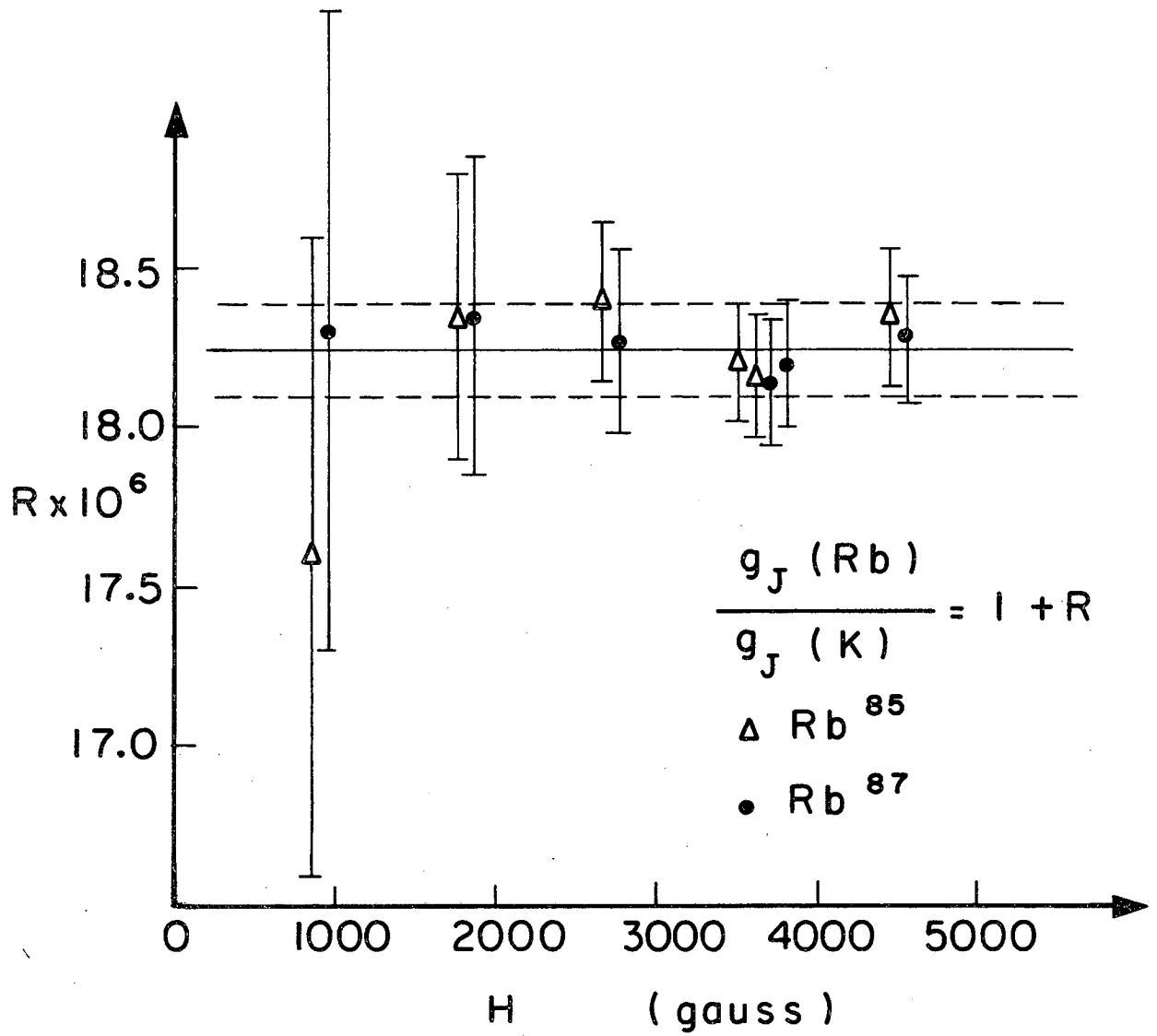
△ Rb^{85}

● Rb^{87}

MUB-4738

Fig. 32. Plot of the ratios $g_J(Rb^{85})/g_J(K^{39})$, $g_J(Rb^{87})/g_J(K^{39})$ versus magnetic field.
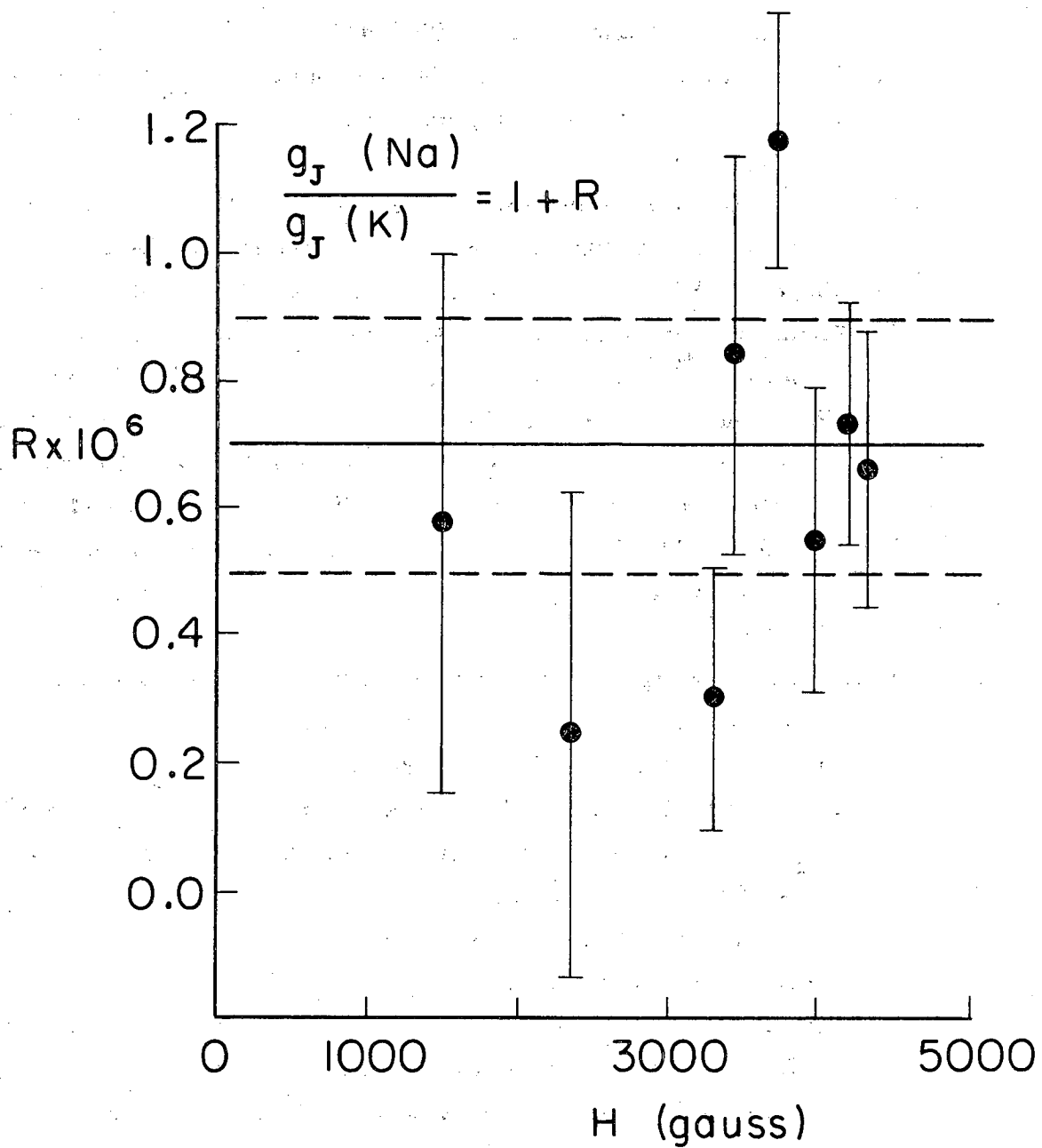
Fig. 33. Plot of the ratio $g_J(Na^{23})/g_J(K^{39})$ versus magnetic field.

REFERENCES

1. Rudolf Ritschl, Über Hyperfeinstrukturen in den Spektren von Kupfer und Gold, Naturwiss. 19, 690 (1931).

2. G. Liljegren, I. Lindgren, L. Sanner, and K. E. Adelroth, Nuclear ground-state spin and magnetic moment of Au^{190}, Arkiv Fysik 25, 107 (1963).

3. W. Bruce Ewbank, Lawrence L. Marino, William A. Nierenberg, Howard A. Shugart, and Henry B. Silsbee, Nuclear Spins of Six Neutron-Deficient Gold Isotopes, Phys. Rev. 120, 1406 (1960).

4. W. Bruce Ewbank and Howard A. Shugart, Hyperfine-Structure Separations of Au^{191} and Au^{193}, Phys. Rev. 135, A358 (1964).

5. Yau Wa Chan, W. Bruce Ewbank, William A. Nierenberg, and Howard A. Shugart, Hyperfine-Structure Separations and Magnetic Moments of Gold-194, 195, and 196, Phys. Rev. 137, B1129 (1965).

6. Yau Wa Chan, W. Bruce Ewbank, William A. Nierenberg, and Howard A. Shugart, Nuclear Spin of 9.5-Hour Au^{196m}, Phys. Rev. 127, 572 (1962).

7. Ekkehard Recknagel, Die Hyperfeinstrukturaufspaltung des Grundzustandes $^2S_{1/2}$ und das magnetische Kerndipolmoment von Au^{197}, Z. Physik, 159, 19 (1960).

8. W. J. Childs and L. S. Goodman, Hyperfine Structure of the $9161\text{-}cm^{-1}$ $^2D_{5/2}$ State of Au^{197} and the Nuclear Electric-Quadrupole Moment, Phys. Rev. 141, 176 (1966).

9. A. G. Blachman and Allen Lurio, Hyperfine Structure of the $^2D_{3/2}$ State of Au^{197}, Bull. Am. Phys. Soc. 8, 9 (1963).

10. Norman F. Ramsey, Molecular Beams (Oxford University Press, 1956).

11. W. A. Nierenberg, The Measurement of the Nuclear Spins and Static Moments of Radioactive Isotopes, in Annual Rev. Nucl. Sci., Vol. 7 (Annual Reviews, Inc., Palo Alto, 1957) p. 349.

12. Polykarp Kusch and Vernon W. Hughes, Atomic and Molecular Beam Spectroscopy, in Encyclopedia of Physics, Vol. XXXVII/1 (Springer Verlag, Germany, 1959), p. 1.

13. R. L. Christensen, D. R. Hamilton, A. Lemonick, F. M. Pipkin, J. B. Reynolds, and H. H. Stroke, Spins and Hyperfine Structure Separations of Radioactive Au^{198} and Au^{199}, Phys. Rev. 101, 1389 (1956).

14. Siegfried Penselin (Physikalisches Institut der Universität, Bonn, Germany), personal communication, 1963.

15. Charlotte E. Moore, *Atomic Energy Levels*, Vol. III, (U. S. Government Printing Office, Washington, D. C. , 1958), p. 186.

16. Charles M. Sommerfield, Magnetic Dipole Moment of the Electron, Phys. Rev. 107, 328 (1957).

17. D. T. Wilkinson and H. R. Crane, Precision Measurement of the g Factor of the Free Electron, Phys. Rev. 130, 852 (1963).

18. M. Phillips, The Effect of Nuclear Motion on Atomic Magnetic Moments, Phys. Rev. 76, 1803 (1949).

19. Henry Margenau, Relativistic Magnetic Moment of a Charged Particle, Phys. Rev. 57, 383 (1940).

20. W. E. Lamb, Jr. , Internal Diamagnetic Fields, Phys. Rev. 60, 817 (1941).

21. M. Phillips, Perturbations of Atomic g Values, Phys. Rev. 88, 202 (1952).

22. E. Fermi, Über die magnetischen Momente der Atom Kerne, Z. Physik 60, 320 (1930).

23. Giulio Racah, Sopra Le Strutture Iperfini, Nuovo Cimento, series 8, 8, 178 (1931).

24. H. M. Foley, Nuclear Moment Discrepancies in Gallium and Indium, Phys. Rev. 80, 288 (1950).

25. W. W. Clendenin, Gyromagnetic Ratio in the Hyperfine Structure of Doublet States, Phys. Rev. 94, 1590 (1954).

26. S. Pasternak and R. M. Sternheimer, An Orthogonality Property of Hydrogenlike Radial Functions, J. Math. Phys. 3, 1280 (1962).

27. Charles Schwartz, Theory of Hyperfine Structure, Phys. Rev. 97, 380 (1955).

28. Charles Schwartz, Theory of Hyperfine Structure, Phys. Rev. 105, 173 (1957).

29. M. H. Brennan and A. M. Bernstein, jj Coupling Model in Odd-Odd Nuclei, Phys. Rev. 120, 927 (1960).

30. Charles Schwartz, The Ground States of Odd-Odd Nuclei, Phys. Rev. 94, 95 (1954).

31. Warren Easley, Norman Edelstein, Melvin P. Klein, D. A. Shirley, and H. Hollis Wickman, Nuclear Spin and Moment of Ag^{110m} by Paramagnetic Resonance, Phys. Rev. __141__, 1132 (1966).

32. Akito Arima and Hisashi Horie, Configuration Mixing and Magnetic Moments of Odd Nuclei, Progr. Theoret. Phys. (Kyoto) __12__, 623 (1954).

33. H. H. Stroke, R. J. Blin-Stoyle, and V. Jaccarino, Configuration Mixing and the Effects of Distributed Nuclear Magnetization on Hyperfine Structure in Odd-A Nuclei, Phys. Rev. __123__, 1326 (1961).

34. Aage Bohr and V. F. Weisskopf, The Influence of Nuclear Structure on the Hyperfine Structure of Heavy Elements, Phys. Rev. __77__, 94 (1950).

35. Jenny E. Rosenthal and G. Breit, The Isotope Shift in Hyperfine Structure, Phys. Rev. __41__, 459 (1932).

36. I. G. Wilson, C. W. Schramm, and J. P. Kinzer, High Q Resonant Cavities for Microwave Testing, in Radar Systems and Components, by Members of the technical staff of Bell Telephone Laboratories (Van Nostrand, Inc., New York, N. Y., 1949) p. 909.

37. Yau Wa Chan, The Nuclear Spins and Magnetic Moments of Ag^{112}, Ag^{113}, Au^{194}, Au^{195}, Au^{196}, and Au^{196m}, (Ph. D. Thesis), UCRL-10334 (June 1962) p. 41.

38. Vernon J. Ehlers (Lawrence Radiation Laboratory), personal communication, 1965.

39. P. A. Vanden Bout, V. J. Ehlers, W. A. Nierenberg, and M. H. Prior, Hyperfine-Structure Separations of Au^{198} and Au^{199}, Bull. Am. Phys. Soc. __8__, 619 (1963).

40. P. A. Vanden Bout, V. J. Ehlers, and W. A. Nierenberg, Hyperfine Structure of Au^{198} and Au^{199}, Seventh Brookhaven Conference on Molecular Beams, Uppsala, Sweden (June 1964).

41. P. A. Vanden Bout, V. J. Ehlers, and W. A. Nierenberg, Hyperfine-Structure Anomaly of Au^{199}, Bull. Am. Phys. Soc. __10__, 691 (1965).

42. P. A. Vanden Bout, V. J. Ehlers, W. A. Nierenberg, and H. A. Shugart, The Hyperfine-Structure Anomalies of Au^{198} and Au^{199}, Bull. Am. Phys. Soc. (to be published).

43. Hans Kopferman, Nuclear Moments (Academic Press, Inc., New York, N. Y., 1958) p. 450.

44. J. R. Platt and R. A. Sawyer, New Classifications in the Spectra of AuI and AuII, Phys. Rev. $\underline{60}$, 866 (1941).

45. W. von Siemens (Ph. D. Thesis), University of Göttingen, Germany (1953) unpublished, as quoted in reference 7.

46. F. M. Kelly, The Nuclear Magnetic Moment of $^{197}_{79}$Au, Proc. Phys. Soc. (London) $\underline{A65}$, 250 (1952).

47. H. Schuler and J. E. Keyston, Hyperfeistrukturen und Kernmomente des Quecksilbers, Z. Physik $\underline{72}$, 423 (1931).

48. Hiroshi Noya, Akito Arima, and Hisashi Horie, Nuclear Moments and Configuration Mixing, Suppl. Prog. Theoret. Phys. (Kyoto) $\underline{8}$, 33 (1958).

49. Leonard S. Kisslinger and Raymond A. Sorensen, Spherical Nuclei with Simple Residual Forces, Rev. Mod. Phys. $\underline{35}$, 853 (1963).

50. Bernard Cagnac, Orientation Nucléaire Par Pompage Optique Des Isotopes Impairs Du Mercure, Ann. Phys. (Paris) $\underline{6}$, 467 (1961).

51. L. C. Balling and F. M. Pipkin, Gyromagnetic Ratio of Hydrogen, Tritium, Free Electrons, and Rb^{85}, Phys. Rev. $\underline{139}$, A19 (1965).

52. New Values of the Physical Constants as Recommended by the NAS-NRC, in Physics Today $\underline{17}$, 48 (1964).

53. H. J. Dahmen and S. Penselin, for address, see Ref. 56 personal communication, and given at the Seventh Brookhaven Conference, Uppsala, Sweden, 1964.

54. V. W. Cohen (Brookhaven National Laboratory), personal communication, 1965.

55. Ingvar Lindgren, Table of Nuclear Spins and Moments, in Alpha-, Beta-, and Gamma-Ray Spectroscopy, Vol. 2, Kai Siegbahn, Ed., (North-Holland Pub. Co., Amsterdam, 1965) p. 1621.

56. S. Penselin (Physikalisches Institut der Universität, Bonn, Germany) personal communication, 1963.

57. S. Penselin, V. Moran, V. W. Cohen, and G. Winkler, Hyperfine Structure of Electronic Ground States of Rb^{85} and Rb^{87}, Phys. Rev. $\underline{127}$, 524 (1962).

58. P. A. Vanden Bout, V. J. Ehlers, and Tuncay Incesu, Electronic g_J Factors of Rubidium and Cesium, Bull. Am. Phys. Soc. $\underline{9}$, 740 (1964).

59. Erol Aygün, Vernon J. Ehlers, Adnan Saplakoglu, and Howard A.
    Shugart, Electronic g_J Factor of Sodium, Bull. Am. Phys. Soc.
    <u>10</u>, 691 (1965).

60. William Perl, Relativistic Contributions to the Magnetic Moment of
    n-Electron Atoms, Phys. Rev. <u>91</u>, 852 (1953).

61. Vernon W. Hughes, <u>Electron Magnetic</u> Moment and Atomic Magnetism,
    in <u>Recent Research in Molecular Beams</u> (Academic Press, Inc.,
    New York, N.Y., 1959) p. 65.